CONTROLLING COLLOIDAL ASSEMBLY AND PHASE BEHAVIOR VIA MORPHING ENERGY LANDSCAPES

by

Jianli Zhang

A dissertation submitted to Johns Hopkins University in conformity with the requirements for the degree of Doctor of Philosophy

Baltimore, Maryland

October 2020

ABSTRACT

Controlling assembly of colloidal particles into different phases and microstructures could provide bases to understand and manufacture novel materials with non-trivial properties and numerous potential applications. A common strategy is to direct the assembly with prefabricated topographical or chemical patterns. This approach is useful in rapid assembly of massive materials but is inherently an irreversible process and is unable to achieve reconfigurable control. Field mediated self-assembly, on the other side, directs the process through interaction with external fields, including optical, magnetic, and electric, and provides a promising path for more sophisticated microstructures. One of the most imminent research goals in this area is to design novel external field patterns and control strategies with an aim for a scalable assembly. In this dissertation, MHz AC electric fields are used to generate reconfigurable and multi-dimensional fields and to accomplish three goals: 1) understanding equilibrium phase behaviors under multi-dimensional external fields, 2) controlling assembly of defect-free colloidal crystal with optimal strategy, and 3) scale up the assembly control to hierarchical colloid structures.

Equilibrium behavior of particles under external field is critical in understanding phase transition and nonuniform distribution of colloidal systems; it is also important practically in investigating novel control mechanisms. Equilibrium particle concentration profile can be derived by considering the interaction between particles and field and by balancing the interactions with osmotic pressure due to inhomogeneous particle concentration. Equation of states for effective hard disks can be used to relate osmotic pressure with particle concentration, so that we can derive a general relationship between the external energy landscape and particle concentration distribution. Based on the theory,

we successfully predicted local and global phase transitions as well as two-dimensional particle distribution under external fields. Our findings also provide foundations for the following dynamic control problems.

For the second goal, we rely on morphing electric fields and energy landscapes to control the self-assembly of particles into defect-free crystals with circular morphology. We first observed that morphology changes in response to applied electric fields enhance the diffusion of grain boundaries and formation of perfect crystals. We derived an optimal feedback control strategy based on the initial observation and a reinforcement learning study. We showed that the assembly of perfect crystal is most efficient when the applied anisotropic field is aligned with grain boundary orientation. The control strategy achieves 100% yield of perfect crystals within an order of magnitude shorter time compared to precedent works. We also demonstrated the scalability of our approach in assembly of larger colloidal systems.

Finally, we extend our knowledge in design an assembly strategy for hierarchical structures. Our specific goal is to achieve periodic colloidal crystals with perfect structure and circular morphology. We design an electrode array with independently activated poles, which can dynamically generate multiple DC and MHz AC electric fields. Through computer simulations, we showed a control process includes coarse partitioning particles into separate clusters, equalizing cluster size by particle redistribution, removing grain boundaries in all clusters, and restoring circular morphologies for the periodic structures. We demonstrated the scalability of the control to various cluster sizes. We also discussed potential applications of electrode array and field mediate assembly in other scenarios.

Committee:

Prof. Michael A. Bevan (academic advisor, ChemBE)

Prof. Paulette Clancy (ChemBE)

Prof. Yannis Kevrekidis (ChemBE)

Prof. Todd Hufnagel (Material)

Prof. Francesca Serra (Physics)

For my family

ACKNOWLEDGEMENTS

The last five years of my life has been a truly enjoyable experience and an exciting learning journey. Compared between who I was before fall of 2015 and who I become now the changes are dramatic in my personality, intellectual capability, and professional skills.

I want to thank my parents, who encouraged me to purse a PhD journey in the first place, and continuously support me in my personal and academic lives. I want to thank my wife, Yinghui, for her constant confidence in me, and being the one I can always get soothe from. I want to thank my son, Peter, for his constant distraction with his cuteness. He is probably still too young to tell what he has done to reshape my life.

I want to thank my advisor, Prof. Michael Bevan, for professional guidance of my scientific personal development. There are millions of details regarding research that I learned from him.

I want to thank Prof. Paulette Clancy, Prof. Yannis Kevrekidis, Prof. Todd Hufnagel, Prof. Francesca Serra, Prof. Chao Wang, and Prof. Robert Leheny for discussing and offering great ideas for my research, and kindly being committee members.

I want to thank my lab mates: Yuanxing Zhang and Junyan Yang, for helping with experiment and simulation works, Yuguang Yang and Brad Rupp, for training me with many aspects of research, and Nikki Neibloom, for being a great lab twin. I also want to thank other lab mates for being friendly and supportive throughout of my PhD: Jenny Jumai'an, Rachel Stein, Alex Yeh, Lechuan Zhang, and Xiao Wang, and former alumni: Matt Petroff, Isaac Torres, and Anna Coughlan. The life without these wonderful people would be totally different.

TABLE OF CONTENTS

LIST OF FIGURES

1 INTRODUCTION

1.1 Background

Ordered colloid microstructures possess many unique properties and show extensive applications in areas such as photonics, optoelectronics, energy conversion, and biological and chemical sensing. Transition of colloidal system between dilute dispersion and condensed morphology has also been studied as a model of phase behavior and other equilibrium kinetics. Controlling spatial and temporal arrangement of colloids an ongoing research topic, and typically involves a trade-off between resolution and scalability. Precise, particle-level control, such as optical tweezer, is one of the most accurate methods to control the spatial organization of colloids.[1] The limitation, on the other hand, is its limited operation area and weak scalability. Massive, entropy-driven assembly approaches, such as evaporation deposition, often introduce undesired defects and/or require extended time.[2] In order to maintain high throughput as well as sufficient resolution, directed self-assembly is considered as a desirable approach to manufacture novel nano- and micro-scale materials.[3]

Two general categories of directed assembly exist, namely template mediate assembly and field mediate assembly. Template mediate assembly relies on prefabrication of surface-modified substrates, which selectively induce colloid deposition. A wide range of microstructures have been fabricated based on this approach, although a common limitation is the prerequisite template manufacture.[4] External field mediate assembly, on the other hand, has received broad attentions for enabling precise control to local and global particle organizations, and achieving well defined and tunable colloidal structures, and

enabling. Various types of external fields have been considered for self-assembly control, including electric field,[5] magnetic field,[6] and shear field.[7] External fields introduce additional driving forces re-equilibrate particles, thereby forming specific patterns. A common challenge for such type of control is to dynamically tune the fields such that kinetically trapped states of defected structures can be prevented and/or resolved. Gravitational field, for example, has long been used to deposit particles into condensed structures. While the magnitude of field can be tuned relatively easily in centrifuges, spatial control is difficult and usually requires prefabricated substrates. Electric field, of all possible candidates, is most suitable for such goals for two reasons. First, the interactions between colloids and electric fields are universal for native colloids in aqueous medium.[8] Second, multiple types of electric fields are possible to control colloidal systems, and both the spatial and temporal features of electric fields can be dynamically tuned based on a fixed electrode design.[9]

Open questions remain in electric field mediate colloid assembly. First, a robust and general strategy to direct assembly of particles into perfect structures is highly desirable and yet still under investigation. Although various open-loop strategies have been proposed based on simple, one-dimensional electric fields, searching for more sophisticated field patterns and associated control policies not only further enhances the overall assembly performance in terms of success rate and time cost, but also provide insights and possibilities to understand complex, nonuniform colloid phase behaviors. Moreover, scalability of electric field and assembled pattern is a nontrivial topic. Very few attempts have been devoted to extending from a single crystal of a finite size to larger systems or hierarchical structures. The scalability of electric field mediate assembly is

critical in achieving massive control of macroscopic structures.

1.2 Objective

This dissertation is devoted to several scientific and engineering aspects of fundamental thermodynamics and self-assembly mechanisms of colloidal systems. The first objective is to understand the equilibrium distribution and phase behaviors of colloidal under multi-dimensional external field. Previous works focused on examining the distribution of particles under one-dimensional energy landscape, and successfully predict phase transition and other interesting thermodynamic behaviors.[10] Octupole electrode is used to generated reconfigurable isotropic and anisotropic electric fields with two-dimensional variation. Particles are equilibrated in each field conditions and form different phases and morphology structures. The second objective is to employ various isotropic and anisotropic electric fields in direct the assembly of colloidal crystals. We observed effects of morphing field shapes to the relaxation of grain boundary defects, and developed image analysis algorithms to characterize the crystal properties including global and local density, global and local crystallinity, position and orientation of structural defects (grain boundaries), and shape and orientation of cluster morphology. We also apply reinforcement learning algorithms in optimizing control strategy. The goal is to enhance the yield and time cost for colloidal crystal assembly. The last objective is to extend a single cluster self-assembly to hierarchical colloidal crystal assembly. We rely on an electrode array to generate various types of electric fields, and breakdown the control process in key operation steps. The goal is to investigate the scalability of forming periodic and ordered structures using external fields.

1.3 Dissertation Overview

This dissertation is divided into chapters. *Chapter 2* reports spatially varied equilibrium phase behavior under anisotropic electric fields. We derived the theory by considering the force on a single particle due to external field and the osmotic pressure due to nonuniform particle concentration. By incorporating the equation of states for effective hard disks, we proposed a general relationship between particle concentration distribution and the applied energy landscape. We used the theory to predict local phase transition and condensation of particles under different external field shapes and magnitudes. We also successfully predicted particle distribution under external field. We concluded that three parameters are directly related the equilibrium distribution of colloidal system: global density maximum, mean density of particles, and the shape and magnitudes of external field. The theory is presumably applicable to any types of field in arbitrary multi-dimensional system.

Chapter 3 reports control of colloid assembly of perfect crystals based on morphing electric fields. We controlled the colloid morphology by applying isotropic and anisotropic electric fields. We observed an enhancement in grain boundary diffusion and relaxation due to morphology change. We used on reinforcement learning to yield optimal control strategy, which suggests that the grain boundary can be most effective removed when the applied anisotropic field is aligned with grain boundary orientation. We also developed an image analysis algorithm to automatically track critical system parameters and achieve a closed-loop control system. The proposed control strategy achieves 100% yield of perfect crystals with circular morphology and reduced the mean assembly time by an order of magnitude compared with the most advanced precedent approach. We also demonstrate

the scalability of the strategy in assembling crystals with larger system sizes.

Chapter 4 reports a simulation work to obtain hierarchical colloidal crystals using an electrode array. Previously, we focused primarily on assembly of a single cluster, while in this work we present an approach to extend to theoretically infinite clusters. Our goal is to form hierarchical crystals with equal size, perfect structure, and circular morphology. We rely on an array of independently controlled electrodes to generate various types of DC and MHz AC electric fields. The control first partitions particles in coarse clusters. Next, particles are redistributed between adjacent clusters in order to equalize all cluster sizes. Last, all clusters are simultaneously controlled to remove grain boundaries and form circular morphology. We demonstrate the scalability of this approaching in obtaining hierarchical crystals of various sizes. We also discussed potential applications of electrode array and field mediate colloid control in other assembly tasks.

Finally, *Chapter 5* summarizes major accomplishments and findings, and discuses several potential directions and outlooks for electric field mediate colloidal control.

2 SPATIALLY VARYING COLLOIDAL PHASE BEHAVIOR ON MULTI-DIMENSIONAL ENERGY LANDSCAPES*

2.1 Abstract

A method is reported to determine equilibrium concentration profiles and local phase behavior for colloids on multi-dimensional energy landscapes. A general expression is derived based on local particle concentration and osmotic pressure differences that are balanced by forces on colloids due to energy landscape gradients. This analysis is applied to colloidal particles in high frequency AC electric fields within octupolar electrodes, where the energy landscape can be shaped in two dimensions. Predictions based on modelling colloids with an effective hard disk equation of state indicate inhomogeneous solid and fluid states coexisting on different shaped energy landscapes including multiple minima. Model predictions show excellent agreement with time-averaged Brownian Dynamic simulations at equilibrium. Findings demonstrate a general approach to understand colloidal phase behaviour on energy landscapes due to external fields, which could enable control of colloidal microstructure on morphing energy landscapes and the inverse design of fields to assemble hierarchically structured colloidal materials.

---

*Reprinted with permission from "Spatially varying colloidal phase behavior on multi-dimensional energy landscapes." *Journal of Chemical Physics* 152 (2020). By Jianli Zhang, Yuanxing Zhang, and Michael A. Bevan.

2.2 Introduction

Numerous scientifically and technologically important problems involve colloidal particles interacting with external fields. Many studies investigate steady transport of colloids in external fields balanced by hydrodynamic drag such as sedimentation,[11] electrophoresis,[12] dielectrophoresis,[13] magnetophoresis,[14] etc. The present study is concerned with the equilibrium distribution and local phase behavior of colloidal particles in external fields. The classic example of this type of problem is sedimentation equilibrium of colloids in a gravitational field. A similar analysis to the one used for sedimentation equilibrium can be used to determine equilibrium distributions and local phase behavior of colloids in other fields (*e.g.*, electric, magnetic, optical, acoustic). While gravitational fields can be tuned using a centrifuge, other field types can be tuned in amplitude but also spatially, providing the opportunity to generate more complex equilibrium concentration profiles.

A brief review of sedimentation equilibrium illustrates the basic features of calculating concentration profiles in external fields. First, we limit our review to cases where concentration profiles do not change significantly on scales comparable to particle dimensions, which enables the assumption that local thermodynamic properties are equivalent to a bulk system at the same concentration (*i.e.*, the "local density approximation"[15-16]). For sedimentation equilibrium, a differential change in elevation produces osmotic pressure changes due to concentration variations; the osmotic pressure change (times a unit area) is balanced by the gravitational force acting on each particle (within a unit volume). The gravitational force is the local gradient of the single particle position dependent energy (*i.e.*, potential energy landscape). This illustrates the basic

connection between equilibrium concentration profiles and potential energy landscapes.

Integrating the differential force balance for sedimentation equilibrium is straightforward; the gravitational energy landscape is a 1D linear function of elevation; when combined with the ideal gas equation of state for the dispersion osmotic pressure, the result is an exponential concentration profile. This profile was confirmed for dilute colloids in pioneering optical microscopy experiments by Perrin.[17-18] Performing the same analysis with the hard sphere equation of state[19-20] predicts macro-scale colloidal dispersion concentration profiles with non-uniform fluid and solid phases, which were confirmed using direct sampling[21] and x-ray measurements.[22-23] For micron sized electrostatically stabilized colloids, the sedimentation equilibrium analysis with an effective hard sphere equation of state[24] predicts micro-scale non-uniform fluid and solid phases, which have been confirmed using confocal microscopy.[25] The sedimentation equilibrium analysis is commonly used in inverse fashion to extract phase behavior and equations of state from measured concentration profiles of complex colloidal particles in gravitational fields (*e.g.*, magnetic colloids,[26] Janus particles,[27] active particles[28-29], binary mixtures[30], rods[30]).

The equilibrium distribution of colloids in any field can be obtained by an analysis that is fundamentally the same as that for sedimentation equilibrium. For example, one particularly common case is for charged colloids in non-uniform high frequency AC electric fields.[13, 31] This interaction has been used to confine colloidal dispersions in electric bottles[32-33] and to assemble colloids into non-uniform fluid, liquid crystal, and crystal phases.[34-38] The time averaged interaction corresponds to an induced dipole in a non-uniform field, which yields an energy landscape that has been previously modeled[39-40] and verified in direct measurements of particles between parallel electrodes (via a Boltzmann

inversion of measured position histograms).[41-42] The energy landscape depends on field shape and material properties; when particles are less polarizable than the medium their lowest potential energy state is at the electric field minimum, and when particles are more polarizable than the medium their lowest potential energy state is at the electric field maximum (analogous to the role of density in sedimentation equilibria).[42-43]

Concentration profiles and phase behavior of colloids in AC electric fields has previously been investigated for simple energy landscape shapes. For example, in the central region of a quadrupolar electrode (Fig. 2-1), the energy landscape has only a radial dependence, so that concentration profiles can be modeled with a 1D differential force balance in the radial coordinate. One difference to the sedimentation equilibrium problem is that the energy landscape has a quadratic dependence on the radial coordinate due to the electric field shape.[44-45] In this example, the quasi-2D osmotic pressure can be modeled with a modified hard disk equation of state[46-47] based on perturbation theory.[24] Concentration profiles show a non-uniform solid decaying from the potential energy minimum to a non-uniform fluid at its periphery, which has been validated in experiments.[45] A related analysis of concentration profiles of 3D hemispherical colloidal crystals interacting with gravity and AC quadrupolar electric fields was accurately modeled as the superposition of two separable 1D problems (*i.e.*, orthogonal gravitational and electric fields).[44]

A general approach has not been reported for relating concentration profiles and local phase behavior of colloids on energy landscapes that vary in more than one dimension. For example, physical surface patterning can produce a gravitational energy landscape, which could have an arbitrary shape based on topographies that cannot be

reduced by symmetry to 1D landscapes. We have previously performed such measurements with repulsive and attractive colloids levitated by electrostatic repulsion on top of a topographically patterned gravitational energy landscape.[48-49] The particle distribution was simulated with Monte Carlo by adjusting a potential energy landscape in an inverse analysis, but an analytical model was not developed to relate concentration profiles to the energy landscape. With the availability of increasingly sophisticated methods to shape energy landscapes for colloids based on their interactions with patterned electric, magnetic, and optical fields, it is necessary to understand how the local balance of osmotic pressure and particle forces determines concentration profiles. By understanding how shape tunable energy landscapes connect to local concentration and phase behavior, fields can be designed to spatially pattern colloids with different local microstructures corresponding to equilibrium phases.

Here, we investigate a model system consisting of an octupolar electrode that can shape 2D electric fields and energy landscapes for small ensembles of several hundred colloidal particles. This provides a realistic model based on past experiments[37-38, 50-51] to control colloidal assembly on energy landscapes that can be morphed between different shapes. A general method is presented for determining equilibrium 2D concentration profiles and local phase behavior on different shaped energy landscapes. Analytical predictions for concentration profiles and local phase behavior are validated based on Brownian Dynamic (BD) simulations of particles on a variety of 2D energy landscapes with a systematic increase in shape complexity. In addition to validating predictions, results are presented to show practically how numerical solutions are obtained depending on available information (*i.e.*, particle number, reference concentration, etc.). Although

findings are presented for the specific case of induced dipoles in high frequency AC electric fields, the general approach for obtaining concentration profiles and local phase behavior on multi-dimensional energy landscapes can be applied to any field mediated energy landscape

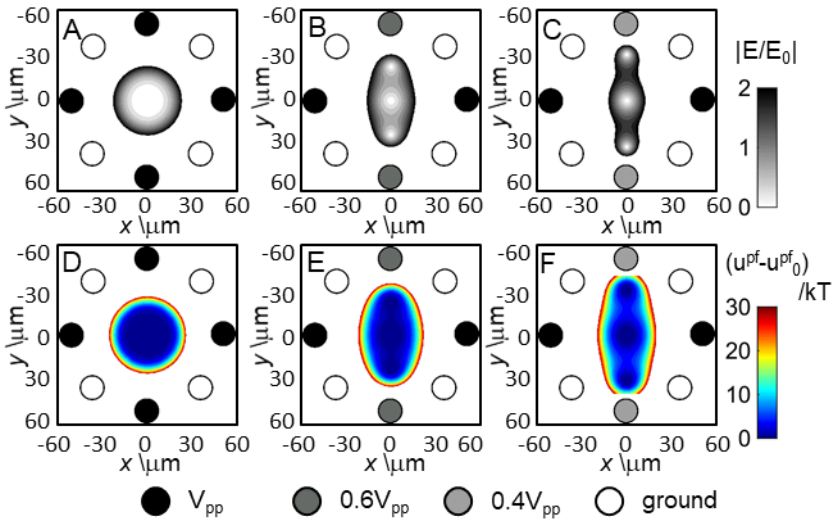

Figure 2-1 **Two dimensional electric fields and energy landscapes in octupole electrode.** (A-C) Electric field in grayscale contour plot. Electrode voltages are normalized by a reference voltage of V_{pp}=3.0V applied to west-east electrodes, and fields are normalized by $E_0=V_{pp}/d_g$, where d_g=100μm is the electrode gap width in diagonal direction. Voltage ratios applied to the west-east and north-south electrodes are set as (A) V_{pp}:V_{pp}, (B) V_{pp}:0.6V_{pp}, and (C) V_{pp}:0.4V_{pp}. (D-F) Corresponding potential energy landscapes are plotted relative to the electric field central minimum up to ~30kT.

2.3 Theory

2.3.1 Interaction Potentials

The net interaction on particle i, u_i, in a high-frequency AC electric field is given by,[38]

$$u_i = u_i^{pf} + \sum_{j \neq i} u_{ij}^{pp} \tag{2.1}$$

where the first term is the superposition of particle-field potentials, which in the present study includes only an induced dipole-field potential given by,[42]

$$u^{pf}\left(x,y\right)=-2\pi\varepsilon_m a^3 f_{cm} E^2\left(x,y\right) \tag{2.2}$$

where (x,y) is the particle center Cartesian coordinate, ε_m is the medium dielectric constant, a is particle radius, f_{cm} is the Clausius-Mossotti factor, and $E(x, y)$ is the local electric field magnitude. The second term is the superposition of particle-particle pair potentials given by,

$$u_{ij}^{pp}=u_{ij}^{e}\left(r_{ij}\right)+u_{ij}^{dd}\left(r_{ij},x_i,y_i\right) \tag{2.3}$$

where u_{ij}^{e} is electrostatic repulsion between particles with electrostatic double layers given by,[52]

$$u^{e}\left(r\right)=32\pi\varepsilon_m a\left(\frac{kT}{e}\right)^2\tanh^2\left(\frac{e\psi}{4kT}\right)\exp\left[-\kappa\left(r-2a\right)\right] \tag{2.4}$$

where r is center-to-center distance, e is elemental charge, ψ is the colloid surface potential, and κ is the inverse Debye length. The second particle-particle potential in Eq. (2.3) is for induced dipole-dipole interactions given by,[41, 43]

$$u^{dd}\left(r,x,y\right)=-\pi\varepsilon_m a^3 f_{cm}^2 P_2\left(\cos\theta\right)\left(\frac{2a}{r}\right)^3 E^2\left(x,y\right) \tag{2.5}$$

where $P_2(\cos\theta)$ is the second Legendre polynomial, and θ is the angle between induced dipoles.

2.3.2 Equation of State

The osmotic pressure, $\Pi(\rho)$, for quasi-2D colloidal dispersions can be modeled using the hard disk equation of state as,

$$\Pi(\rho) = kT\rho Z(\rho) \tag{2.6}$$

where ρ, is number density (*i.e.*, particles/area), and the hard disk compressibility factor, $Z(\eta)$, in terms of area fraction, $\eta = \pi a^2 \rho$, is given by,[46-47]

$$\begin{aligned} Z_{HD}(\eta) &= \begin{cases} Z_{HD,\mathrm{F}}(\eta), & \eta \le \eta_f \\ Z_{HD,S}(\eta), & \eta_m \le \eta \le \eta_{cp} \end{cases} \\ Z_{HD,\mathrm{F}}(\eta) &= \left[1 + \left(\eta^2/8\right)\right](1-\eta)^{-2} \\ Z_{HD,\mathrm{S}}(\eta) &= 2\left[\left(\eta_{cp}/\eta\right) - 1\right]^{-1} + 0.67\left[\left(\eta_{cp}/\eta\right) - 1\right] + 1.9 \end{aligned} \tag{2.7}$$

where $Z_{\mathrm{HD,F}}$ is the fluid compressibility factor up to freezing ($\eta_{\mathrm{f}} \approx 0.69$), and $Z_{\mathrm{HD,S}}$ is the solid compressibility factor from the melting ($\eta_{\mathrm{m}} \approx 0.71$) up to close packing ($\eta_{\mathrm{CP}} = 0.906$).[53-54] The hard disk equation of state can be used for particles with short-range interactions compared to the particle radius[55] by replacing η with an effective area fraction, η_{eff}, given by,[44]

$$\eta_{eff} = \pi a_{eff}^2 \rho \tag{2.8}$$

with an effective radius, a_{eff}, from a perturbation theory given as,[24]

$$2a_{eff} = 2a + \int_{2a}^{\infty} \left[1 - \exp\left(-u^e(r)/kT\right)\right] dr \tag{2.9}$$

based on a particle pair potential, $u^{\mathrm{e}}(r)$. Eq. (2.6) can then be re-written in terms of η_{eff} as,

$$\Pi\left(\eta_{eff}\right) = kT\frac{\eta_{eff}}{\pi a_{eff}^2}\mathrm{Z}_{HD}\left(\eta_{eff}\right) \tag{2.10}$$

2.3.3 1D Force Balance

Differential changes in local osmotic pressure can be related to forces acting on particles within differential spatial elements (the concentration and energy landscape gradients are larger compared to particle dimensions; *i.e.*, the local density approximation[15-16]). This is often derived in an intuitive manner for the case of sedimentation equilibrium,[25] but has also been shown for colloids in 1D (1D) electric fields.[44] Here, we first illustrate this differential balance for a symmetric potential energy landscape with a radial dependence in polar coordinates but no angular dependence (which allows this case to be tested in a 2D Cartesian coordinate system as a benchmark). A force balance can be written to equate the osmotic pressure difference between concentric rings at distances of r and r+Δr (left hand side below) to the local field mediated force acting all the particles between the rings (right hand side below) as,

$$2\pi r\cdot\left[\Pi\left(r\right)-\Pi\left(r+\Delta r\right)\right] = -\frac{du^{pf}\left(r\right)}{dr}\cdot\rho\left(r\right)\cdot 2\pi r\cdot\Delta r \tag{2.11}$$

where the force on each particle due to the external field can be obtain as the local gradient of a potential energy landscape. In the limit as $\Delta r \to 0$, the differential form of Eq. (2.11) becomes,

$$\frac{d\Pi\left(r\right)}{dr} = -\frac{du^{pf}\left(r\right)}{dr}\rho\left(r\right) \tag{2.12}$$

where integrating both sides with respect to r gives,

$$\int d\Pi(r) = -\int \rho(r) \cdot du^{pf}(r) \tag{2.13}$$

which indicates differential changes in local osmotic pressure can be related to differential changes in the local energy landscape and local density. Inserting an energy landscape and equation of state into Eq. (2.13) and integrating yields concentration profiles including phase behavior.

2.3.4 2D Force Balance

In this section, we extend the analysis of the 1D case in Eqs. (2.11)-(2.13) to arbitrary 2D energy landscapes. Given a 2D potential energy landscape in Cartesian coordinates, $u^{pf}(x, y)$, differential changes in local osmotic pressure are given by partial differential equations as,

$$\frac{\partial \Pi(x,y)}{\partial x} = -\frac{\partial u^{pf}(x,y)}{\partial x} \cdot \rho(x,y), \quad \frac{\partial \Pi(x,y)}{\partial y} = -\frac{\partial u^{pf}(x,y)}{\partial y} \cdot \rho(x,y) \tag{2.14}$$

which can be integrated with respect to x and y, and add together to give,

$$\int \frac{\partial \Pi(x,y)}{\partial x} \cdot dx + \int \frac{\partial \Pi(x,y)}{\partial y} \cdot dy = -\int \rho(x,y) \frac{\partial u^{pf}(x,y)}{\partial x} \cdot dx - \int \rho(x,y) \frac{\partial u^{pf}(x,y)}{\partial y} \cdot dy \tag{2.15}$$

which, by chain rule of total derivatives, can be simplified as,

$$\int d\Pi(x,y) = -\int \rho(x,y) \cdot du^{pf}(x,y) \tag{2.16}$$

which has the same expression as Eq. (2.13) except for the coordinate. This indicates that 2D differential changes in local osmotic pressure can be related to differential changes in the local energy landscape and the local density.

2.3.5 Equilibrium Concentration Profiles

Inserting any equation of state into Eq. (2.16) and re-arranging gives,

$$\int_{\rho_0}^{\rho(x,y)} \frac{1}{\rho} d\left(\rho \cdot Z\right) = -\frac{1}{kT}\left(u^{pf}\left(x,y\right) - u_0^{pf}\right) \tag{2.17}$$

where the left-hand side is integrated from a reference density, ρ_0, to the density at position, $\rho\,(x, y)$, and the right-hand side is integrated from the reference energy, $u^{\mathrm{pf}}{}_0$, to the same energy landscape position, $u^{\mathrm{pf}}(x, y)$. The same result is obtained for a 1D coordinate by inserting Eq. (2.10) into Eq. (2.13). The concentration profile, $\rho\,(x, y)$, depends only on reference particle density ρ_0 and the potential energy difference between the reference state and position of interest. By inserting the hard disk equation of state (Eq. (2.10)) into Eq. (2.17), and expressing density in terms of effective area fraction η_{eff} (Eq. (2.8)), an expression for effective hard disks is given by,

$$\int_{\eta_0}^{\eta_{eff}(x,y)} \frac{1}{\eta} d\left(\eta \cdot Z_{HD}\right) = -\frac{1}{kT}\left(u^{pf}\left(x,y\right) - u_0^{pf}\right) \tag{2.18}$$

which gives the spatially varying concentration profile in terms of the energy landscape and equation of state. The total number of particles, N, in a system is given by,

$$N = \int_{-\infty}^{+\infty}\int_{-\infty}^{+\infty} \rho\left(x,y\right) dxdy \tag{2.19}$$

2.3.6 Order Parameters

The local six-fold bond orientational order parameter of particle i is given as,[56]

$$\psi_{6,i} = \frac{1}{N_C^i} \sum_{j=1}^{N_C^i} e^{i6\theta_{ij}} \tag{2.20}$$

where N_C^i is the number of coordinated neighbors within the first coordination shell of particle i, and θ_{ij} is the angle between two particle centers for an arbitrary reference angle. The crystalline connectivity, χ_6^{ij}, of particle i with coordinated neighbor j is defined as,

$$\chi_6^{ij} = \frac{\left|\mathrm{Re}\left[\psi_{6,i}\psi_{6,j}^*\right]\right|}{\left|\psi_{6,i}\psi_{6,j}^*\right|} \tag{2.21}$$

where $\psi_{6,j}^*$ is the complex conjugate of $\psi_{6,j}$. The local six-fold connectivity order parameter, $C_{6,i}$, is defined as the number of crystalline neighbors for particle i with 6-fold order given by,[57]

$$C_{6,i} = \frac{1}{6} \sum_{j=1}^{N_C^i} \left[\begin{vmatrix} 1 & \chi_6^{ij} \geq 0.32 \\ 0 & \chi_6^{ij} < 0.32 \end{vmatrix} \right] \tag{2.22}$$

2.4 Methods

2.4.1 Electric Field Simulations

The octupole electrode was modeled using the electrostatic interface in COMSOL Multiphysics software. The octupole was centered in the bottom of a 400 μm by 400 μm rectangular chamber with a height of 20 μm, and was filled with 0.1mM NaOH aqueous solution. Each electrode pole was 20 μm in diameter, 40nm in thickness, and positioned on the vertices of an octagon with a 100 μm diagonal distance. The top view of the octupole is illustrated in Fig. 2-1. The electrodes are represented by grayscale circles. The electric field in the octupole center was solved at a height of 1.5 μm from the bottom surface, which

is equivalent to the equatorial elevation of a 3 μm particle touching the substrate. The resulting electric field is tabulated in a look-up table with a 0.25μm grid resolution and a magnitude normalized by $E_0=V_{pp}/d_g$, where V_{pp} is voltage applied to the east-west poles, and d_g is the electrode gap distance; a specific magnitude electric field is obtained by multiplying the normalized table with V_{pp}. For Brownian Dynamics simulations, intermediate values were obtained from the look-up table by Barycentric interpolation,[58] and used to compute energy landscapes given by Eq. (2.2).

2.4.2 Brownian Dynamics Simulations

Table 2-1 **Model and simulation parameters based on prior experiments**. (a) Particle radii, (b) medium dielectric constant, (c) Debye length, (d) Clausius-Mossotti factor, (e) zeta potential, (f) electrode gap.

Parameter	equation	value	parameter	equation	value
a (nm)[a]	(2.2), (2.4),	1000	f_{cm}[d]	(2.2)	-0.47
ε_m[b]	(2.2), (2.4),	78	ψ (mV)[e]	(2.4)	-75
κ^{-1} (nm)[c]	(2.4)	10	d_g (μm)[f]	Fig. 1	100

Brownian Dynamics simulations were used to obtain the dynamic equilibrium distribution of particles on each energy landscape. The simulation details are the same as in previously reported studies.[59-60] The dynamics is discretized into time steps of 0.1ms, during which the total force on particle, which is defined in Eqs. (2.1)-(2.5), is considered to be constant. The electric field in Eqs. (2.2) and (2.5) was obtained from the lookup table as described above. The remainder of the parameters used in the simulations are reported in Table 2-1. The particles were randomly placed in the electric field at the beginning of every simulation, and the equilibrium state is identified by the plateau of total potential energy felt by all particles. After equilibrium, the particle coordinates were recorded every simulation second for a total of 1000s. A total of 10^4 individual simulations are conducted

for each case. The particle distribution is counted as the normalized visit frequency to every square of 0.1μm wide in the simulation area.

2.4.3 Given η_0 and $u^{pf}(x,y)$, solve $\eta_{eff}(x,y)$ and N

Eq. (2.18) gives the relationship between the potential energy landscape, reference concentration, and concentration profile. In addition, Eq. (2.19) relates the concentration profile and total number of particles. With four variables and two equations, two variables need to be defined to solve for the remaining two variables. In cases where the concentration profile, $\eta_{eff}(x,y)$, is given, the other variables can be obtained in a straightforward manner. When the reference particle concentration, η_0, and the energy landscape, $u^{pf}(x, y)$, are given, the other two parameters can be found as follow. By inserting η_0 into Eq. (2.18) to relate u^{pf} and η_{eff}, the concentration profile is obtained, and then the total particle number is obtained from Eq. (2.19).

2.4.4 Given N and $u^{pf}(x,y)$, solve η_0 and $\eta_{eff}(x,y)$

Given the total particle number and energy landscape, a bisection numerical method is used to solve for the concentration profile. This is done by iterating the reference area fraction, $\eta_{0,i}$, until $N(\eta_{0,i})=N$ (as in the previous section calculation). In each iteration, the mid-point value, $\eta_{0,i}=0.5(\eta_{0,lo}+\eta_{0,up})$, is used to solve for the distribution and total particle number, $N(\eta_{0,i})$, where $\eta_{0,lo}$ and $\eta_{0,up}$ are lower and upper bounds used in the bisection method that satisfy $N(\eta_{0,lo})<N$ and $N(\eta_{0,up})>N$. The bounds are initialized with guesses and are updated according to the bisection method that halves the interval $[\eta_{0,lo}, \eta_{0,up}]$ with each iteration. Convergence is guaranteed because N is an integer.

2.4.5 Given N and η_0 solve energy landscape magnitude (V_{pp}) and $\eta_{eff}(x,y)$

Given the total particle number, reference area fraction, a bisection numerical method is used to solve for the concentration profile and energy landscape magnitude. The energy landscape in this work is given by Eq. (2.2), where electric field amplitude determines the energy landscape magnitude (although physical properties in the prefactor could also be changed in a similar fashion). In this case, the applied voltage, V_{pp}, is a prefactor in the electric field look-up table, so adjusting it changes the energy landscape magnitude. Similar to the previous cases, the value of V_{pp} is iterated using the bisection method until $N(V_{pp})=N$.

2.5 Results & Discussion

2.5.1 Anisotropic Non-Uniform Energy Landscapes

Figs. 2-1A-C show results for three electric fields based on applying different voltages to electrode pairs within a coplanar octupole electrode (see *Methods*). Figs. 2-1D-F show potential energy landscapes for an induced dipole in the non-uniform AC electric fields given in Figs. 2-1A-C. The potential energy landscapes are given by Eq. (2.2), which we previously measured directly for single colloidal particles between coplanar parallel electrodes[41-43] and within the central region of coplanar quadrupolar electrodes.[44-45, 59]

The magnitudes of the potential energy landscapes in Fig. 2-1 are determined by $|\mathbf{E}^2|$ in Eq. (2.2), which are scaled by peak-to-peak voltage, V_{pp}, applied to the eat-west poles. Different shaped fields and landscapes are generated by applying different relative voltages to electrode pairs within the octupole. In each case, the east-west electrodes have V_{pp}=3V, and the north-south electrode pairs are set as ratios of this voltage (see Fig. 2-1

caption, schematics). The remaining electrodes are ground. The first landscape in Fig. 2-1D for a symmetric quadrupolar state produces an isotropic energy landscape in the vicinity of the central electric field minimum, which has a radial dependence with no angular variations. The other two cases (Figs. 2-1E, F) have different voltage ratios applied in orthogonal directions to produce anisotropic energy landscapes. The resulting energy landscapes in these latter cases both global minima at the field minimum at the electrode center, as well as, local energy minima along the axis of the low voltage poles.

2.5.2 Concentration Profiles & Phase Behavior on Energy Landscapes

Fig. 2-2 illustrates the procedure for obtaining spatially varying concentrations profiles and phase behavior on a 2D energy landscape. An example case is shown where the total number of particles is specified (N=100) and the energy landscape is specified (Fig. 2-1F). The goal is to determine the concentration profile, $\rho\,(x, y)$, given the energy landscape, $u^{\mathrm{pf}}(x, y)$ using the approach outlined in *Methods*. This requires an iterative scheme since Eq. (2.18) cannot be solved algebraically to a closed-form expression for $\rho\,(x, y)$ and $\eta_{\mathrm{eff}}(x, y)$ as a function of $u^{\mathrm{pf}}(x, y)$.

Figs. 2-2A, B show the electric field and energy landscape for this particular case. Fig. 2-2C shows three representative relationships between $\eta_{\mathrm{eff}}(x, y)$ and $u^{\mathrm{pf}}(x, y)$, which are calculated using Eq. (2.18) with different reference area fractions, η_0. Using the bisection method, the initial iteration starts with a guess of η_0=0.85, which gives a specific relationship between η_{eff} and u^{pf} (Fig.2-2C, 1st iteration). The relationship can be used to plot $\eta_{\mathrm{eff}}(x, y)$ in Fig. 2-2D, which corresponds to a total number of N=165 particles. In the subsequent iterations, additional $\eta_{\mathrm{eff}}(x, y)$ from Eq. (2.18), and N from Eq. (2.19) are

obtained. Figs. 2-2C-F show concentrations profiles for the first, third, and fifth iterations in this scheme, where N_1 = 165 ($\eta_{0,1}$=0.85), N_3=26 ($\eta_{0,3}$=0.64), and N_5=100 ($\eta_{0,5}$ =0.80). The fifth iteration results in the correct number of particles, and the concentration profile shown in Fig. 2-2F is the correct one for the energy landscape.

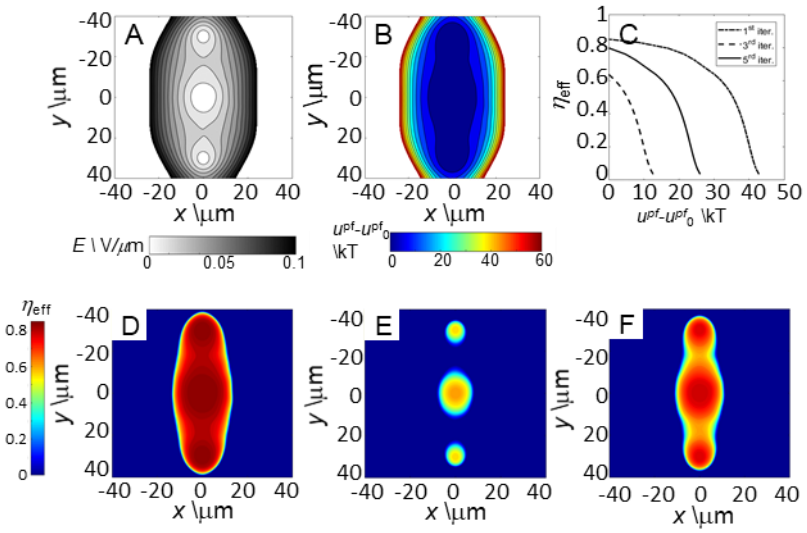

Figure 2-2 **Solving for particle concentration profile given number of particles and energy landscape.** (A) The electric field, $E(x, y)$, generated using a reference voltage of V_{pp}=3V and V_{pp}:0.4V_{pp} (see Fig. 2-1) (B) Corresponding energy landscape, $u^{pf}(x, y)$. (C) Relationship between $\eta_{eff}(x, y)$ and $u^{pf}(x, y)$ solved over the 1st, 3rd, and 5th iteration using bisection method according to Eq.(2.18). (D-F) Concentration profiles plotted in the same color bar for the same three iterations in panel C with N=165, 26, and 100.

2.5.3 Radially Symmetric Energy Landscape: Comparison of 1D & 2D Analyses

After showing how to calculate concentration profiles for given energy landscapes in Fig. 2-2, results from Brownian Dynamic (BD) simulations are compared to theoretical predictions to demonstrate the validity of the approach. Fig. 2-3 first shows results for the radially symmetric energy landscape in Fig. 2-1A, D, which provides a benchmark case since it can be predicted from either a 1D or 2D analysis. Comparison with BD simulations also provides the opportunity to demonstrate the validity of the "local density

approximation"; agreement between particle-scale simulations and predicted concentration profiles shows whether it is valid to assume concentration profiles do not change significantly on scales comparable to the particle dimensions (and local thermodynamic properties are equivalent to a bulk system at the same concentration[15-16]).

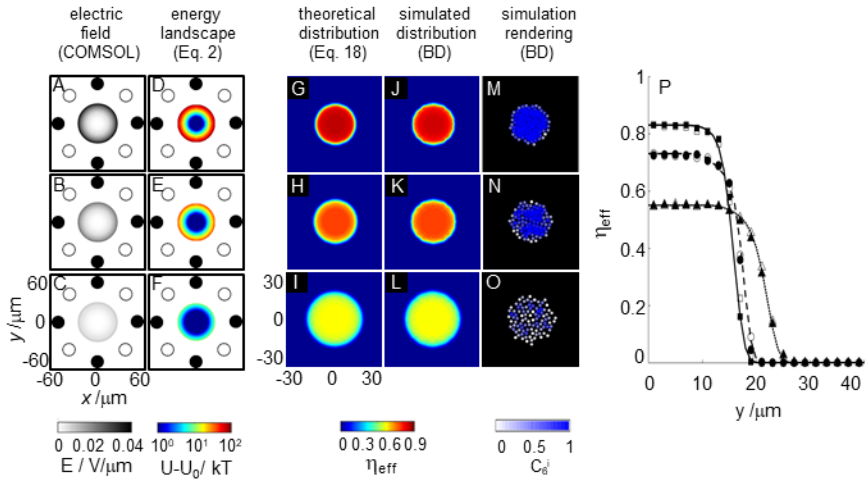

Figure 2-3 **Equilibrium concentration profiles of *N*=100 particles on energy landscapes resulting from V_{pp}:V_{pp} fields.** (A-C) Electric field, $E(x, y)$, generated using a reference voltage of V_{pp}=0.9V (A), 2.2V (B), and 3.8V (C). (D-F) Corresponding energy landscapes, $U^{pf}(x, y)$. (G-I) Theoretical concentration profiles from Eq. (2.18) with maximum center area fractions of η_0=0.83 (G), 0.73 (H), and 0.55 (I) corresponding to solid, solid near melting conditions, and fluid phases. (J-L) Concentration profiles from time averaged Brownian Dynamic simulation at equilibrium. (M-O) representative simulation renderings with particles colored using a white-blue scale based on the local C_6^i (white for $C_{6,i}$ = 0, blue for $C_{6,i}$ = 1). (P) One-dimensional concentration profiles along positive y-axis. For the cases of η_0=0.83, 0.73, and 0.55, the theoretical estimations are shown using solid line, dash line, and dot line, and the simulation results are shown using square, circle, and triangle symbols. BD simulations with and without field-induced dipolar interactions shown by open and closed symbols

The first two columns of Fig. 2-3 show the electric field and corresponding energy landscapes that are used to equilibrate the particles. Fig. 2-3G-I shows theoretical concentration profiles (Eq. (2.18)) for N=100 particles on symmetric landscapes with the same voltage applied in both directions (Fig. 2-1A,C) for V_{pp}=0.9V, 2.2V, and 3.8V. BD results are shown in Fig. 2-3J-L as equilibrated time-averaged concentration profiles and Fig. 2-3M-O as renderings of single configurations. Particles in the rendered configurations

are colored by their six-fold connectivity order parameter, C_6, in Eq. (2.22), which helps to visualize whether they are part of fluid or solid phases. Fig. 2-3P compares theoretical and simulated profiles along the positive y-axis of the energy landscape. Open points indicate BD simulations with dipolar pair interactions (Eq. (2.5)), and closed points are obtained by neglecting this interaction.

The results for BD simulations and the predictions in Eq. (2.18) display excellent agreement for each of the three energy landscape amplitudes. In each case, the predicted and simulated 2D concentration profiles appear essentially identical, and the 1D profiles clearly show close correspondence between predictions without dipole-dipole interactions and simulations with and without dipolar interactions. While the predictions are based on the hard disk equation of state with perturbation theory to account for electrostatic repulsion, the BD simulations with dipolar interactions could result in a significantly different equation of state and resulting spatial variation in phase behavior. However, the dipolar interactions have a negligible effect for the conditions investigated in Fig. 2-3. This result is consistent with prior work for colloidal particles in radially non-uniform energy landscapes with no angular variations (also due to high frequency AC electric field mediated interactions).[44-45] This behavior is understood as arising from a net cancellation of dipolar interactions in solid phases,[61] which also appears to be a reasonable approximation in dense fluids states.[41-43] The agreement between the model prediction and BD simulation results also demonstrates the validity of the local density approximation.

The results in Fig. 2-3 also show the 1D analysis (Eq. (2.13)) and 2D analysis (Eq. (2.16)) both agree with the BD simulations, which provides a benchmark for the 2D analysis prior to its implementation in other cases that cannot be solved with the 1D

analysis. The 2D analysis can be shown to analytically reduce to the 1D analysis for the case in Fig. 2-3 where a change in coordinate system together with symmetry makes the two analyses identical. A similar 1D analysis to the case in Fig. 2-3 was reported in prior work.[44-45]

The results in Fig. 2-3 also show how different amplitudes of energy landscapes with the same shape changes spatial variations in particle concentration including local phases. The maximum area fractions at the energy landscape potential energy minimum for the three cases in Fig. 2-3 are η_0 =0.55 (V_{pp}=0.9V), η_0 =0.73(V_{pp}=2.2V), and η_0=0.83(V_{pp}=3.8V). The latter two cases have maximum effective area fractions indicating the presence of a hard disk solid phase. Both of these cases have concentration profiles that decays radially as an inhomogeneous solid, and at greater radial distances, a number of different microstructures are observed. In the steepest potential energy well, the density vanishes form the hard disk solid state within less than a particle diameter indicating all particles are in the solid phase. In the next steepest potential energy landscape, the hard disk solid density decays into a coexisting fluid periphery, which rapidly vanishes over several particle radii. The lowest amplitude energy landscape contains an inhomogeneous dense fluid state that radially decays and vanishes. In each case, local structure based on C_6 values indicate crystalline microstructures consistent with the expected solid phases. In short, the results in Fig. 2-3 show that Eq. (2.18) is accurate for the simple 1D energy landscape and all effective hard disk concentrations including single fluid, solid, and coexisting phases.

2.5.4 Concentration Profiles & Phase Behavior on 2D Energy Landscapes

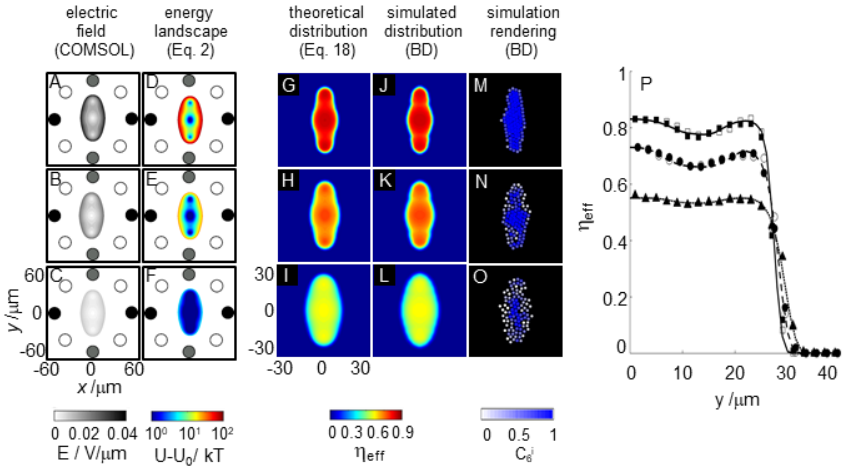

Figure 2-4 **Equilibrium concentration profiles of *N*=100 particles on energy landscapes resulting from V_{pp}:0.6V_{pp} fields.** Panel organization and legends same Fig. 3. Reference voltages are V_{pp}=0.9V (A), 1.9V (B), and 3.3V (C). Maximum center area fractions are η_0=0.83 (G), 0.73 (H), and 0.55 (I).

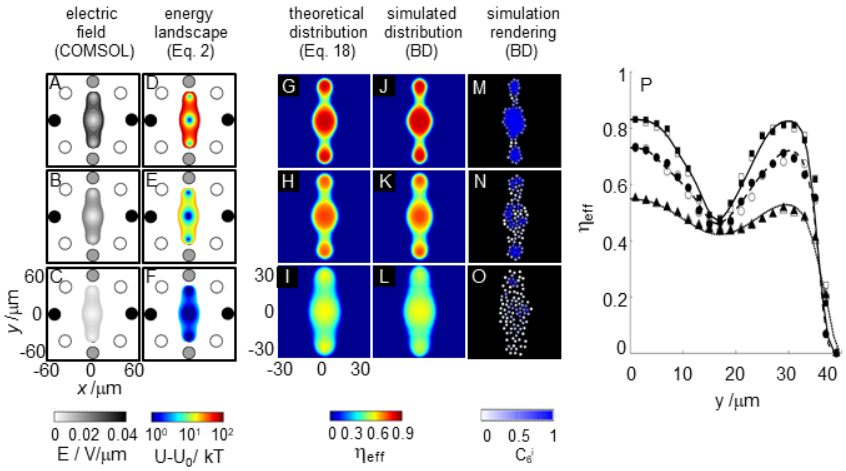

Figure 2-5 **Equilibrium concentration profiles of *N*=100 particles on energy landscapes resulting from V_{pp}:0.4V_{pp} fields.** Panel organization and legends same Fig. 3. Reference voltages are V_{pp}=0.8V (A), 1.6V (B), and 2.5V (C). Maximum center area fractions are η_0=0.83 (G), 0.73 (H), and 0.55 (I).

Figs. 2-4 and 2-5 show concentration profiles for particles on 2D energy landscapes, which capture both local phase behavior and ensemble morphology. Results

are presented in the same organization as Fig. 2-3. The landscapes are 2D in this case since they cannot be reduced to a single coordinate through symmetry (and thus require the 2D analysis in Eq. (2.16) rather than the 1D analysis in Eq. (2.13)). The electric field and energy landscape shapes investigated are shown as the first two columns. The field amplitudes were set so that the maximum particle concentration at the energy landscape minimum in Figs. 4 and 5 is the same as the cases presented in Fig. 2-3.

The results in Figs. 2-4 and 2-5 for different 2D landscape morphologies show excellent agreement between predictions of the 2D model (Eqs. (2.16) and (2.18)) and BD simulation results. Variations in phase behavior are captured in each case including inhomogeneous fluids, solids, and their transition. Figs. 4-4P and 4-5P shows cases with nearly all particles in solid phases, all particles in the fluid phases, and cases where solid phases exist in three separate potential energy wells with intervening and peripheral fluid regions. The V_{pp}:0.4V_{pp} field generates three isolated crystalline domains connected by fluid phases, which is due to local energy maxima between minima. Dipolar interaction between particles have negligible effects in BD results for the concentration profiles in Figs. 2-4 and 2-5 (consistent with Fig. 2-3). The results in Figs. 2-3-2-5 together show how energy landscape shape and amplitude can be used to control morphology, concentration profiles, and local phase behavior of colloidal particles.

2.5.5 Concentration Cross Sections from Arbitrary Initial Coordinates

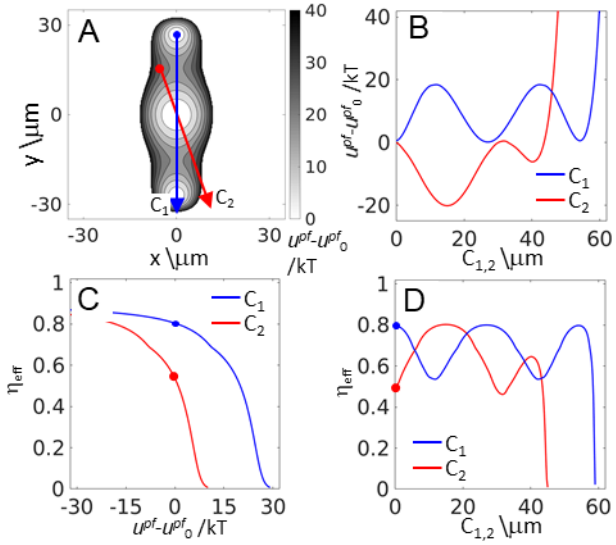

Figure 2-6 **Calculating concentration profile cross sections.** (A) Energy landscape generated by V_{pp}:0.4V_{pp} with V_{pp}=2V. Two directions, denoted as C_1 and C_2, shown in red and blue lines. (B) 1D energy landscapes along the lines shown in (A) with matching colors with reference states at origins. The x-axis is the distance along C_1 or C_2 directions. (C) Relationship between potential energy magnitude and particle area fraction, solved using ρ_0 = 0.8 (blue) and 0.51 (red) in Eq. (2.18). Reference area fractions are found from simulation and marked by points in the figure. (D) 1D particle concentration distributions along C_1 and C_2 directions.

Fig. 2-6 shows how low-dimensional cross sections can be obtained from arbitrary starting coordinates other than the global energy minimum or density maximum. This practically demonstrates a different aspect of using Eq. (2.18). For an anisotropic energy landscape, Fig. 2-6A shows two 1D cross sections originating from different starting coordinates including different directions on the landscape. The 1D energy landscapes are shown in Fig. 4-6B with the same color scheme vs. the coordinates C_1 and C_2 given by equations of lines in Cartesian coordinates. The 1D energy landscapes are reported for energies relative to value at their respective origins. Fig. 2-6C shows the dependence of η_{eff} on u^{pf} given by Eq. (2.18) where points indicate the effective area fractions at the

energy landscape origin (η_0=0.8 (blue) and 0.51 (red)) These reference effective area fractions can be obtained from either theory or BD simulation as discussed in Fig. 2-5. With η_{eff} vs. u^{pf} in Fig. 2-6C, and u^{pf} vs. C_1 and C_2 in Fig. 4-6B, it is straightforward to plot η_{eff} vs. C_1 and C_2 in Fig. 2-6D using the same color scheme as the other panels.

The results in Fig. 2-6 are fundamentally same as the 2D plots in Fig. 2-5 in that both cases solve the distribution of particles on a 2D energy landscape. However, Fig. 2-6 also demonstrates several useful aspects of calculating such 1D concentration profiles. For example, the starting states are not located at global energy landscape minima, but can be chosen at arbitrary initial coordinates. This enables initial states to be chosen with more flexibility and convenience. In addition, multiple reference positions can be chosen if local concentration profiles and phase behavior are required at different arbitrary coordinates on an energy landscape. The initial area fractions are not required to be the maximum value along a spatial coordinate, which was the approach demonstrated in the example in Fig. 2-2 and employed in Figs. 2-3-2-5. As shown in Fig. 2-6D, starting from different energy landscape coordinates and initial concentrations can still be used to compute the density at other coordinates along a profile. The results in Fig. 2-6D confirm the consistency of the distributions along C_1 and C_2 directions, because both distributions yield the same maximum density at the global energy minimum at the 2D landscape center.

The example in Fig. 2-6 shows that the same relationship between potential energy and area fraction can be used to specify the concentration profile and phase behavior along any energy landscape cross section. The relationship in Fig. 2-6C is also the same as those reported in Fig. 2-2C, which demonstrates that once the equation of state is known, the expression in Eq. (2.18) can be used to connect concentration profiles directly to any

energy landscape and any coordinates on the landscape. The examples in this paper demonstrate different numerical approaches to use this expression depending what information is known in a given problem statement. Ultimately, the approach in this work demonstrate a general approach to determining concentration profiles and phase behavior on multi-dimensional energy landscapes.

2.6 Conclusions

A method was developed to determine concentration profiles and local phase behavior on energy landscapes that vary in more than one spatial coordinate. A general expression was derived based on local osmotic pressure differences balancing forces on colloids due to energy landscape gradients (when concentration and energy gradients are large compared to the particle size). This analysis is used to study colloidal particles in high frequency AC electric fields, where an octupolar electrode is used to tune the amplitude and shape of electric fields and resulting energy landscapes. By modeling the colloidal particles with an effective hard disk equation of state based on perturbation theory, it is shown that concentration profiles of locally non-uniform solid and fluid phases can be predicted for a variety of different 2D energy landscape shapes including multiple energy minima. Results are compared to Brownian Dynamic simulations to confirm the predictions of the theoretical model against time averaged equilibrium particle configurations. Findings include practical details of determining concentration profiles and cross sections based on different known and unknown variables. Findings from this work demonstrate a general approach for obtaining concentration profiles and local phase behavior on multi-dimensional energy landscapes for colloids interacting with a variety of external fields. The reported approach is amenable to controlling colloidal microstructure

on morphing energy landscapes and to the inverse design of external fields and energy landscapes based on desired colloidal concentration profiles (*e.g.*, hierarchically patterned crystals).

3 CONTROLLING COLLOIDAL CRYSTALS VIA MORPHING ENERGY LANDSCAPES & REINFORCEMENT LEARNING

3.1 Abstract

We report a feedback control method to remove grain boundaries and produce circular shapes in colloidal crystals using morphing energy landscapes and reinforcement learning based control policies. We demonstrate this approach for optical microscopy and computer simulation experiments for colloidal particles in AC electric fields. First, we discover how tunable energy landscape shapes and orientations enhance stochastic grain boundary motion and crystal morphology relaxation. Using these findings, reinforcement learning is used to develop an optimized control policy to actuate morphing energy landscapes to produce defect-free colloidal crystals orders of magnitude faster than natural relaxation times. Morphing energy landscapes mechanistically enable rapid crystal repair via anisotropic stresses to control defect and shape relaxation without melting. This method is scalable for up to at least N=10^3 particles with mean process times scaling as $N^{0.5}$. Further scalability could be enabled by controlling many parallel local morphing energy landscapes (*e.g.*, periodic landscapes) to generate large-scale global defect-free hierarchical structure.

---

*Reprinted with permission from "Controlling Colloidal Crystals via Morphing Energy Landscapes & Reinforcement Learning." *Science Advances* (2020). By Jianli Zhang and Michael A. Bevan.

3.2 Introduction

Controlling assembly of colloidal particles into different microstructures and morphologies could provide a basis to fabricate hierarchically structured materials with non-trivial emergent properties (e.g., optical, mechanical, thermal, acoustic) important to numerous technologies.[62] Many naturally occurring biological materials provide inspiration for creating periodic microstructures with unique multifunctional properties, where such microstructures often have repeat units that could be realized by assembling colloidal components.[63-64] However, despite a common recognition that colloidal assembly could provide a route to synthetic materials that mimic biological material structures and properties, many approaches are limited by defects, as well as, scalability and structural diversity. In addition, changing interactions between initially stable colloids frequently results in amorphous aggregates with minimal functionality. In short, the state of the art in colloidal assembly often falls short of the grand challenge of directing matter into highly ordered nano- and micro- structured materials.

Using biological materials as inspiration for target structures naturally leads to questions about how processes in biological systems produce complex structures. Biological systems are clearly complex in terms of the number of components, interactions, and parallel dynamic processes. A central feature of biological processes is exquisite control over many processes orchestrated in space and time. Although the obvious complexity of biological systems is somewhat overwhelming, it may be a necessary requirement to replicate some minimal aspects of such control in synthetic material systems to achieve comparable structures. Practically, it may be necessary to control colloidal assembly in space and time with a minimal level of sophistication to achieve many

desirable microstructures and morphologies. Such intervention perhaps seems at odds with a popular conception of self-assembly as simply mixing components and waiting for an autonomous process to yield complex defect-free structures. However, formally controlling assembly processes, in a manner similar to biological systems, may be the critical piece missing from many current approaches to assembling defect-free nano- and micro- structured materials.

Based on current limits of colloidal assembly, and with inspiration from biological systems, it seems necessary to control colloidal assembly in space and time, including both microstructures and morphologies. External fields provide mechanisms to control position and orientation of colloidal assemblies and microstructure relaxation. For example, gravitational fields cause colloidal assembly to occur at different spatial coordinates, with crystalline microstructures assembling at potential energy minima.[22, 65-66] Although effective gravitational fields can be controlled macroscopically in centrifuges, and microscopically on topographically patterned landscapes,[49] they are not easily controlled locally and dynamically to manipulate colloidal assembly kinetics and defects. Macroscopic magnetic fields have been used to anneal colloidal microstructures,[67] and local magnetic fields have also been used to assemble small colloidal ensembles,[68-70] but require specific material properties. Shear fields can induce crystallization,[71] but are difficult to control on length scales comparable to particle microstructures and produce significant defects.[72] Optical fields[73-74] can produce induced dipolar interactions in highly localized fields to manipulate many single colloidal particles (*e.g.*, holographic optical tweezers). However, optical fields have not been used to control colloidal assembly and local microstructures beyond proof-of-principle demonstrations.[75-76] Such examples of

colloidal assembly in external fields illustrate both desirable features and challenges with controlling assembly in space and time.

Electric fields can be designed to manipulate colloidal assembly in space and time in a manner that overcomes many limitations of other external fields. Electric fields can be shaped across length scales with different electrode designs[77] including arrays[78-79] and patterns.[80-81] Such spatial control of electric field shape and amplitude along with fast transient responses provides capabilities for rapid control over colloidal assembly and reconfiguration. In general, interactions and transport of colloids in electric fields at different frequencies[8222,23] and in media with varying properties (*e.g.*, polar, non-polar, salt)[12, 83] are sufficiently well understood to manipulate colloidal assembly for diverse materials. More recently, direct measurements have quantitatively connected dipole-field and dipole-dipole interaction potentials to local phase behavior[45] and morphology including different field shapes.[84] The ability to tune electric field shape, amplitude, and frequency in space and time has a number of promising features for achieving high fidelity control over colloidal assembly processes.

Although much is known about colloidal interactions, dynamics, and microstructures in electric fields,[85-86] significant limitations remain in understanding and developing elements to implement formal control of assembly processes. These elements, in the terminology of colloid science (and control science), include capabilities to: (1) quantify microstructures (sense states), (2) tune interactions (actuate state changes), (3) model non-equilibrium microstructure evolution (dynamic models), and (4) determine how to choose colloidal interactions (control policy) based on current and desired states (objective). Some aspects have been previously developed, such as quantifying

microstructures and their dynamic evolution between states for tunable depletion,[87] magnetic field,[88] and electric field[59] mediated assembly processes. In addition, field mediated colloidal assembly dynamic models have been used to implement feedback control in experiments[38] and simulations[89-90] to assemble defect-free colloidal crystals. Such approaches have yielded the unprecedented capability to assemble small defect-free colloidal crystals on relatively short time-scales with complete efficacy.[38] In these prior studies, the control policy, which closes the loop between sensing microstructures and deciding how to actuate fields, was based on a Markov decision process framework using coarse-grained Markov state models. This prior work provides a foundation to pursue control of more complex processes and objectives, but also indicates limitations and directions for development.

In this work, we report morphing electric field shapes to control crystal defect removal rates and morphology. Results are obtained for varying system sizes in microscopy and computer experiments. We first investigate how field shape influences coupled grain boundary (GB) motion and crystal morphology relaxation. This approach is enabled by the capability to morph electric field mediated energy landscapes within octupolar electrodes to control quasi-2D spatially varying colloidal phase behavior (Fig. 3-1).[84] We then develop novel coarse-grained variables, or reaction coordinates, for microstructural and morphological features (*i.e.*, sensors) to quantify dynamic responses to field shape changes (*i.e.*, actuators). To close the loop between sensing and actuation, we employ reinforcement learning (RL) to discover control policies to determine what field shapes and orientations should be actuated to: (1) rapidly remove GBs to obtain single domain crystals, and (2) restore circular crystal morphologies from anisotropic states. Finally, using this control

scheme, the time to obtain target defect-free circular crystals is characterized for different system sizes. Findings from this work inform the design, control, and optimization of colloidal assembly in space and time to realize complex hierarchically structured materials.

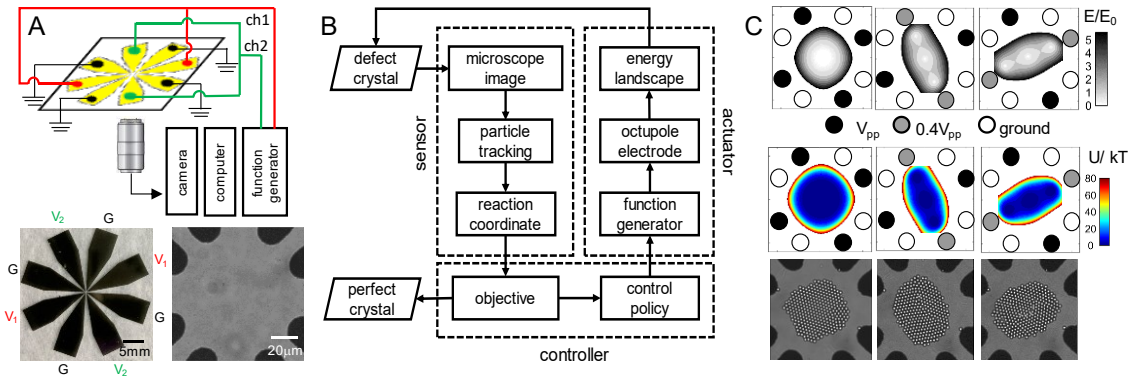

Figure 3-1 **Feedback controlled morphing energy landscape for colloidal assembly.** (**A**) (top) Feedback control configuration consisting of octupole electrode, microscope, CCD camera, computer, and function generator. (bottom) Octupole electrode with two applied voltages, V_1 and V_2, and ground poles, G, with zoom view of electrode center region. (**B**) Feedback control scheme based on morphing energy landscape actuator, reaction coordinate sensors, and RL control policy. (**C**) (top row) Applied voltages determine electric field amplitude and anisotropy as shown for three illustrative cases, including: (left) isotropic fields (V_1:V_2=1:1), (middle) anisotropic field with 112° orientation (V_1:V_2=10:4), and (right) anisotropic field with 22° orientation (V_1:V_2=4:10). (middle row) Corresponding single particle potential energy landscapes. (bottom row) Representative experimental configurations for 2.34 um silica colloids (N=300) for each field.

3.3 Results & Discussion

3.3.1 Anisotropic Field Shape Actuation

To control electric field shape, and field-mediated energy landscapes for quasi-2D colloidal dispersions sedimented onto surfaces, a gold film octupole electrode on a glass microscope slide and connected to a function generator (Figs. 3-1A). A microscope and CCD camera connected to a computer monitor particles positions in real-time to sense the system state, and by connecting the same computer to the function generator, it is possible to close the loop and perform feedback control on the system state. Key elements of the feedback loop involving sensing, actuation, and the control policy (Fig. 3-1B) are described

in the following.

To actuate field-mediated dipolar colloidal interactions within the electrode, different voltages are applied to electrode pairs within the octupole (Figs. 3-1C). This relatively simple electrode configuration provides control of field anisotropy and orientation. By controlling AC voltage and frequency, it is also possible to control the magnitude of dipolar interactions and sign of dipole-field interactions. The *kT*-scale energy landscapes due to dipole-field interactions can be adjusted in shape and magnitude. For high AC frequencies, particles are compressed towards the field minimum at the octupole center, where the assembled morphology depends on the energy landscape shape. We recently reported the equilibrium phase behavior and concentration profiles of colloids on such field mediated energy landscapes.[84] In brief, dipole field energy landscapes are given as,

$$u(x,y) = -2\pi\varepsilon_m a^3 f_{cm} E^2(x,y) \tag{3.1}$$

where ε_m is the medium dielectric constant, a is particle radius, f_{cm} is the Clausius-Mossotti factor that depends on particle and medium dielectric properties, and $E(x,y)$ is the local electric field magnitude. The particle phase behavior and morphology is determined by the concentration profile, $\eta(x,y)$, on the energy landscape as,

$$\int_{\eta_0}^{\eta(x,y)} \frac{1}{\eta} d(\eta Z) = -\frac{1}{kT}\left[u(x,y) - u_0\right] \tag{3.2}$$

where η_0 and u_0 are a reference concentration and energy, and Z is the compressibility factor (effective hard disks in this work, see *SI*). Eq. (3.2) is obtained from integrating a differential force balance of local osmotic pressure and particle forces due to energy landscape gradients. These results allow us to specify electrode voltages for each field

shape to ensure all particles are in the crystal phase (Fig. 3-7) with morphologies determined by the energy landscape shape.

Knowledge of equilibrium phase behavior in different shaped fields provides a basis to begin considering non-equilibrium structures and their dynamic evolution on changing landscapes. Static crystalline configurations within different field shapes show predicted phase behavior and morphology based on model predictions (Fig. 3-1C),[84] but with significant defects in the form of GBs between misoriented crystalline domains. With the present study's objectives of creating defect-free crystalline microstructures with circular morphology, the first task is to understand how changing field shape influences GB removal and morphological dynamic responses.

3.3.2 Microstructure & Morphology Evolution

To quantify microstructure and morphology relaxation on different energy landscapes, here we characterize the temporal evolution of 2D crystals following step-changes in isotropic and anisotropic fields. We introduce reaction coordinates that track dynamic processes (Fig. 3-2A). Raw information includes the applied field shape and orientation from voltage settings and particle coordinates obtained either directly from simulations or from image analysis of microscopy experiments. To monitor GBs, we characterize global crystallinity via bond orientational order (ψ_6), local crystallinity via six-fold connectivity for each particle ($C_{6,\mathrm{i}}$) and its ensemble average ($\langle C_6 \rangle$), which are used together to identify GB orientation in lab coordinates (γ) and relative to the field (α). To monitor crystal morphology, we characterize circularity (c) as well as the shape major-axis orientation in lab coordinates (ϕ) and relative to the field (θ).

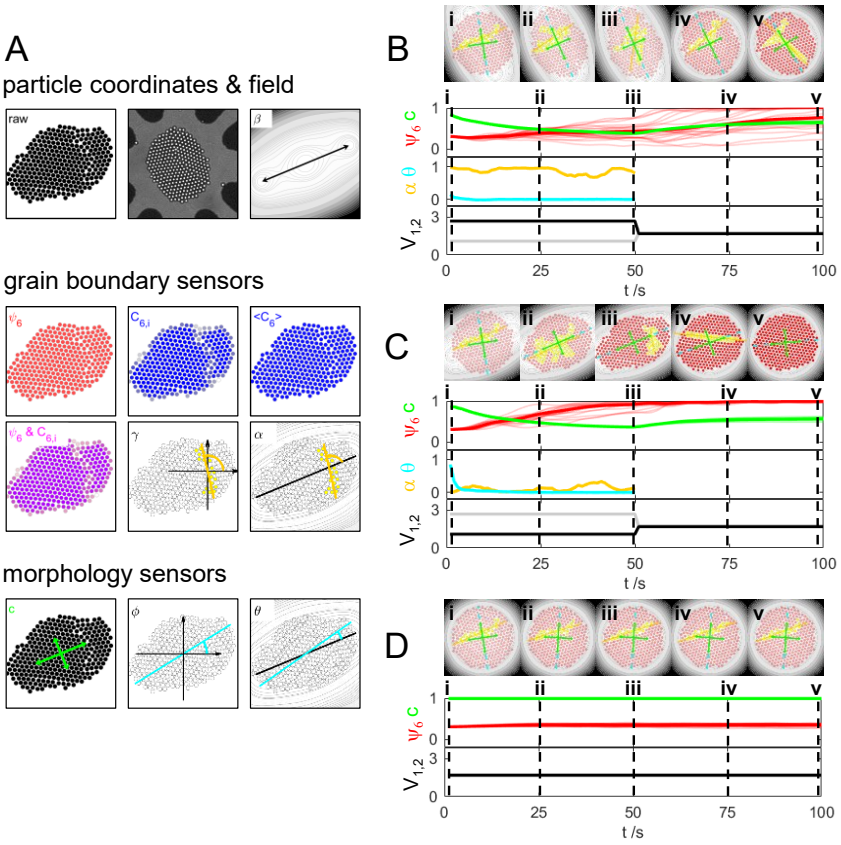

Figure 3-2 **Gain boundary and shape relaxation vs. energy landscape shape and orientation.** (**A**) Particle coordinate analysis in experiments and simulations to obtain reaction coordinates (corner label) for static configurations (see quantitative definitions in *SI*), which can be obtained in real-time trajectories. (Right) Rendered configurations and trajectories for sensors (reaction coordinates) and actuator settings (voltages) for different field shapes and orientations, including: (**B**) anisotropic field nearly perpendicular to the GB (α=87.5°) for 50s, followed by isotropic field for 50s, (**C**) anisotropic field nearly parallel to the GB (α=2.5°) for 50s, followed by isotropic field for 50s, and (**D**) constant isotropic field for 100s. Trajectories show: global crystallinity (ψ_6, red), circularity (*c*, green), GB orientation relative to field (α, yellow), morphology orientation relative to field (θ, cyan), and voltages (V_1, black; V_2, gray). The ψ_6 and *c* trajectories of 19 additional experiments are shown by lighter colored lines.

Brownian Dynamic (BD) simulations are used to investigate how GB motion and crystal shape relaxation are affected by field shape and orientation. We first test whether field shape and orientation can favorably influence GB motion and shape relaxation and demonstrate use of the reaction coordinates for tracking relevant dynamic processes (as part of posing a problem for more extensive testing using RL). A circular crystal of N=300 particles with a single GB is quenched for 50s by anisotropic fields orientated

perpendicular (Fig. 3-2B) and parallel (Fig. 3-2C) to the GB, which is then followed by 50s quenches using isotropic fields. For comparison, a 100s quench with an isotropic field is also shown (Fig. 3-2D). Results suggest how energy landscape shape determines directional stresses and collective dynamic processes to promote both GB migration and shape relaxation. As evident from the first 50s of ψ_6 trajectories, isotropic fields do not affect GB diffusion, whereas both anisotropic field orientations promote GB migration. Alignment of the anisotropic field long-axis parallel to GBs (Fig. 3-2C) yields on average faster GB migration than the perpendicular orientation (Fig. 3-2B). It appears that compression of the crystal domains towards the GB coupled with elongation produces local anisotropic stresses; these appear to favor particle motion within the GB and a net drift of the GB to the crystal periphery.

While anisotropic fields enhance GB removal rates in bicrystals, they also sculpt cluster morphologies to match underlying landscapes.[84] To make a fair comparison with feedback controlled assembly of perfect crystals using isotropic fields,[38] and to achieve the objective of creating circular defect-free crystals, it is necessary to understand relaxation of crystal morphologies towards circular states. The simulated trajectories reveal coupled microstructural and morphological dynamics during the 50s isotropic quench (Figs. 3-2B, C, D). An important aspect of this finding is that we observe defect-free crystals do not relax easily to circular morphologies with only application of an isotropic field. As will be discussed in the following section on feedback control, fields can be shaped with moments orthogonal to the crystal shape anisotropy to provide stronger driving forces for shape relaxation. We defer further discussion of how field shape influences GB removal and shape evolution until after presenting these results.

3.3.3 Feedback Controlled Microstructure & Morphology

The initial experiments addressed scientific questions about how different shaped electric field mediated energy landscapes influence GB motion and morphology relaxation (Fig. 3-2). These findings provide essential information to address the engineering challenge of designing a feedback approach to control crystal defects and shape. By employing microscopy and particle tracking as sensors for crystallinity and shape, and reconfigurable electric field mediated energy landscape shape as an actuator, the only remaining element (Fig. 3-1C) is a control policy to close the loop to achieve the objectives of assembling defect-free circular crystals in minimal time. The feedback control is designed with two objectives, to obtain: (1) defect-free crystal microstructures, and (2) circular crystal morphologies. We describe the development of two control policies that address each objective by specifying how to actuate tunable energy landscapes.

To develop control policies, we employ a combination of empirical testing and machine learning using BD simulations previously matched to experiments via rigorous thermodynamic and dynamic criteria.[38, 59, 84, 91] For comparison, our previous work used a Markov Decision Process framework to develop control policies for assembly of perfect crystals in isotropic fields.[38] This approach required knowledge of the transition probability between all states for each field based on a model; optimization in this approach was achieved by maximizing the probability of reaching a target state by choosing the correct actuator based on instantaneous observations of any system state. The present work avoids construction of a dynamic model for transition probability by employing a combination of initial empirical parametric testing (*i.e.*, human learning) with subsequent reinforcement learning (RL) to obtain final policies.

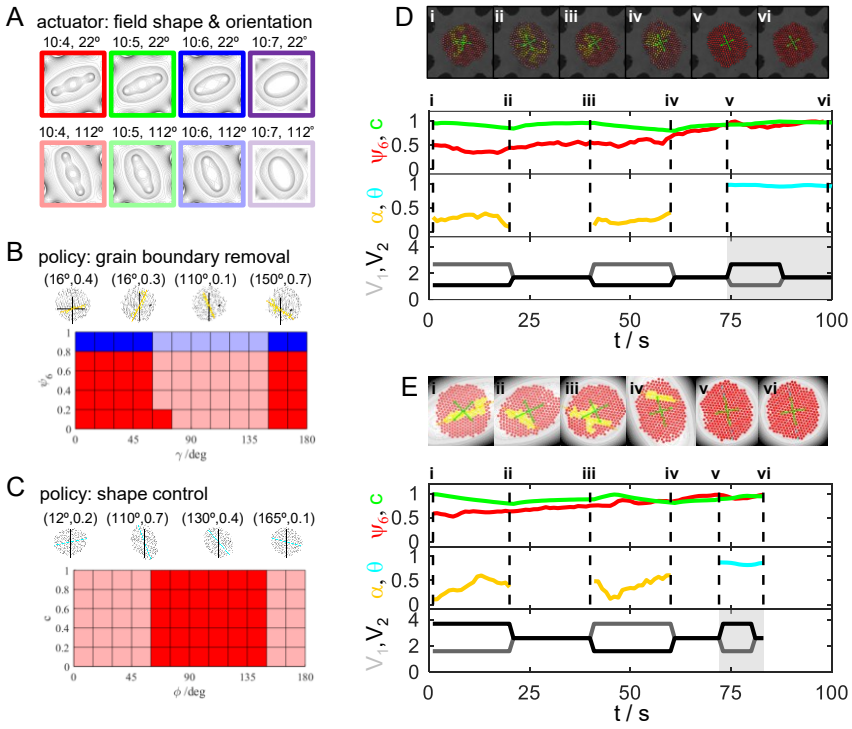

Figure 3-3 **Feedback controlled GB removal and circularity using morphing energy landscapes with RL control policy.** (**A**) Electric field shapes and orientations (actuator choices) for consideration in RL based optimal control policies. RL control policies as look up tables and representative states for: (**B**) GB removal based on sensors for GB orientation (γ) and global crystallinity (ψ_6), and (**C**) circular shape restoration based on sensors for sensors for crystal shape orientation (ϕ) and circularity (c). (**D**) Microscopy experiment including analyzed images and trajectories for: (objectives) global crystallinity and circularity, (sensors) field orientation and shape major axis orientation relative to the GB, and (actuators) applied voltages. Gray region (74s < t < 100s) highlighted in the actuator panel repents the period for morphology control, while the other white region represents the period for GB removal (t < 74s). (**E**) BD experiments including rendered configurations on underlying gray scale energy landscapes and reaction coordinate trajectories with the same information in (B). In images, renderings, and plots, particles and trajectories are colored the same as in Fig. 3-2.

To provide initial estimates of feedback control parameters, we first employed empirical tests to determine characteristic relaxation timescales. Relaxation time was interrogated by testing anisotropic fields with fixed shape (V_{max}:V_{min}=10:4) and random orientations (β=23° or 113°), which were alternated with isotropic fields (Fig. 3-12). For simplicity, the same time period was used for anisotropic and isotropic fields. Findings show alternating anisotropic and isotropic fields every 20s produced the fastest removal of GBs and morphology restoration. These characteristic relaxation times are consistent with

prior measures of GB motion[59] and scaling arguments based on long-time diffusion of particles within GBs.[38]

Next, using 20s period of randomly oriented anisotropic fields alternated with 20s isotropic fields, different field shapes were tested (*i.e.*, voltage ratios, V_{max}:V_{min} = 10:3-10:10, Fig. 3-12). Finding show a 10:4 field aspect ratio produced the fastest GB removal. The most anisotropic field shape (V_{max}:V_{min} = 10:3) occasionally released particles from the octupole center, so it was not further considered. In short, a monotonic increase in GB removal rate was observed with increasing anisotropy in the underlying energy landscape. However, this result was observed with a fixed field shape for all control cycles. The optimal landscape shape is less obvious if both field shape and orientation can be dynamically selected.

Using the control update time and possible field shapes identified in initial testing, we next employed RL to determine the optimal control policies for determining field orientation and shape in feedback control of GBs and crystal morphology. RL obtains optimal policies via algorithm-guided learning through iteratively simulated experiments;[92] this avoids time-consuming dynamic model development.[93] BD simulations are used to enable significantly more statistics than directly using experimental trajectories (and also overcome spatiotemporal sampling limitations). The two control objectives were considered separately during RL (see *Methods*). For both GB removal and crystal shape control, eight anisotropic field shapes and orientations were considered as candidate actuator settings (Fig. 3-3A). In both cases, RL is initialized with all actuator settings being equally likely, so that optimal choices are identified in the course of evaluating statistical outcomes as learning proceeds.

For GB removal, the control policy was discretized into a look-up table based on sensors for GB orientation (γ) and global crystallinity (ψ_6), with representative states rendered for illustration (Fig. 3-3B). The resulting control policy from RL primarily chooses the most anisotropic field (10:4) oriented parallel to GBs, except for highly ordered configurations (ψ_6>0.8) where a less anisotropic field (10:6) is chosen. The choice of field orientations parallel to GBs in consistent with the initial results in Fig. 3-2, but is now verified for many more starting configurations, control trajectories, and for all eight combinations of field shape and orientation. The choice of a lower aspect ratio field for high values of global crystallinity is not obvious but indicates less distortion of crystal morphology is necessary for GB removal. A single asymmetric feature is observed in the GB removal policy at ($60^{\circ}<\gamma<75^{\circ}$, ψ_6<0.2); this condition is for highly defective crystals with GBs oriented about half-way between both possible field orientations, where it appears either field orientation is about equally effective. In short, RL identifies a clear trend for field orientation with a subtle shape change for highly crystalline states.

For crystal morphology control, the control policy was discretized into a look-up table based on sensors for crystal shape orientation (ϕ) and circularity (c), with representative states shown for illustration (Fig. 3-3C). The resulting policy always uses the most anisotropic field (10:4) oriented perpendicular to the crystal shape orientation. This finding is also consistent with preliminary results in Fig. 3-2 showing defect free anisotropic crystals ($\psi_6\approx0.2$, c<1) did not relax to circular shapes in isotropic fields. Whereas GB motion is visibly part of morphology relaxation in polycrystals, microscopy and simulation videos show for defect free crystals a shearing motion along crystal planes are the primary morphology relaxation mechanism. In addition, GBs were not observed to

form as part of morphology relaxation. The same movies also show morphology relaxation does not involve particle migration around the crystal periphery (for either defect free or polycrystals), although such a mechanism is in principle possible. Based on these findings, when the mismatch between crystal and underlying energy landscape shape is small, the driving force for relaxation appears insufficient to overcome relevant elastic moduli of the perfect crystal interior. Practically, the RL policy reduces to a simple heuristic where the most anisotropic field, with the least alignment to the crystal shape major axis, produces the fastest relaxation to circular crystals.

The resulting overall control policy (Table 3-2) then consists of the two sub-policies to achieve the two objectives of removing GBs (Table 3-3) and obtaining circular crystals (Table 3-4). The GB removal policy is called until a perfect crystal is obtained (*i.e.*, ψ_6>0.99), followed by the policy to restore morphology until a circular crystal is formed (*i.e.*, c>0.99). Endpoint detection within both sub-policies enables early termination as soon as objectives are met. To allow for the possibility of introducing defects during the process for restoring circular morphology, the GB removal algorithm can be called at any control update time when defects are detected. In practice, we never observed GBs being reintroduced into crystals during morphology relaxation for the several hundred realizations conducted in the course of our study.

The resulting optimized control policies were implemented in experiments to test their effectiveness for generating defect-free crystals with circular morphologies (Fig. 3-3). Individual realizations for feedback control of 300 particle ensembles are shown for microscopy (Fig. 3-3D) and simulated (Fig. 3-3E) experiments. Reaction coordinate trajectories now formally serve as sensors for microstructure and morphology. Global

crystallinity (ψ_6) and circularity (c) indicate progress toward control objectives of creating single domain crystals and perfect circular morphology and are used for end-point detection. The field orientation relative to the GB (α) and to the crystal shape major axis (θ) are used in control policies with feedback control to decide field orientation to promote GB removal and restoration of circular morphologies. Applied voltage to each electrode (V_1, V_2) show how the electric field is actuated using the policy.

Simulated and experimental trajectories show how feedback control using the control policies work in practice. In both simulated and experimental trajectories, the GB removal policy is called during two control update periods and terminated early during the second period via end-point detection. After GB removal, both defect-free crystal lattices have shapes corresponding to circularities of c=0.7-0.9, which requires the circular shape restoration policy. In both cases, application of an anisotropic field orthogonal to the crystal long-axis yields a circular morphology in ~5-10s. Changing crystal morphology does not introduce any new internal defects; this appears to result from crystals shape relaxation occurring via shearing motion along crystal planes. Based on successful demonstrations in experiments and simulations, in the following, we obtain statistics for many more controlled trajectories, which we compare for different policies and system sizes.

3.3.4 Control Performance & Scaling

The feedback control performance can be quantified based on more statistics, comparison to other approaches, and as a function of system size. Control performance (Fig. 3-4) is reported for statistical comparisons of many individual stochastic trajectories including 10^2 microscopy experiments and 10^3 simulated experiments. Instantaneous and cumulative

yields of perfect crystals vs. time are reported for three cases: (1) the feedback controlled alternating anisotropic/isotropic field developed in this work (Fig. 3-4A), (2) a feedback controlled isotropic field from our prior work (Fig. 3-4B) (details in *SI* and Ref. [38]), and (3) uncontrolled quenches to a constant isotropic field (Fig. 3-4C). For comparison, individual experimental and simulated realizations for the last two approaches are shown in Fig. 3-13,14. All control experiments begin with quenched bicrystal configurations characterized by a single GB, high local order, and low global order (C_6>0.9, ψ_6<0.6). Each policy also has an identical objective of producing a defect-free single domain crystal (ψ_6>0.99). The second objective of circular morphology is automatic for isotropic fields. Mean times (and standard deviations) to yield different percentages of defect-free circular crystals are compared for each case (Fig. 3-4D). The logarithmic fits capture cumulative yield vs time data up to 100% yields for controlled cases at finite times (and uncontrolled data at short-times; long-time asymptotic behavior may differ).

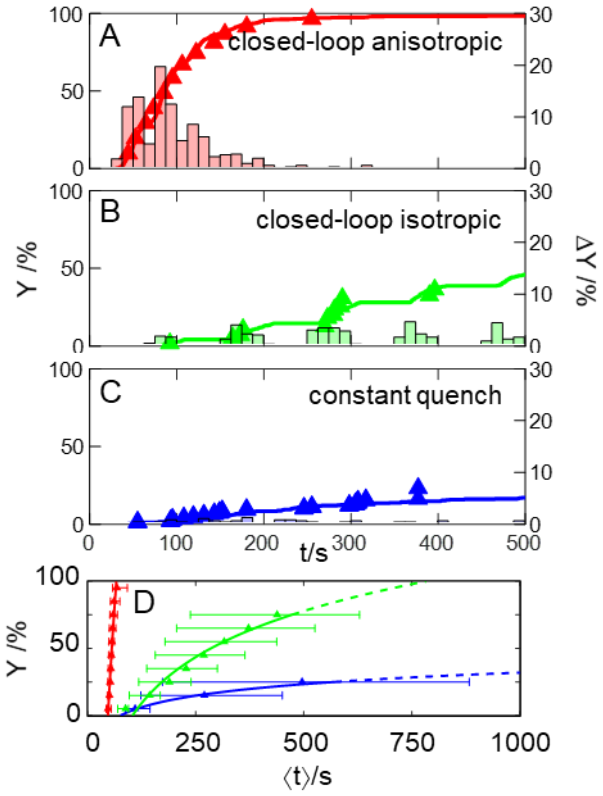

Figure 3-4 **Defect-free circular crystal yield vs. time for different control strategies.** Cumulative yield (Y, left-axis) of defect-free circular crystals for 10^2 microscopy experiments (points) and 10^3 simulated experiments (lines) as well as instantaneous yield (ΔY, right axis) values from simulated experiments (bars). Results for three different control strategies include: (**A**) the new feedback approach based on morphing energy landscapes with an RL based policy, (**B**) a former feedback approach based on changing isotropic energy landscape amplitudes with a MDP based policy[38] (Fig. 3-14), and (**C**) a constant uncontrolled quench using an isotropic field[45, 84] (Fig. 3-13). (**D**) Cumulative defect-free circular crystal yield vs. average time, $\langle t \rangle$, for each control policy in A-C (same coloring) using simulation results (points). $\langle t \rangle$ obtained for all t up to yield Y within the time limit. Left value error bar is standard deviation for all t less than $\langle t \rangle$ given value of Y; right value error bar standard deviation for all t greater than $\langle t \rangle$ given value of Y. Empirical logarithmic fits to each case are given by: (anisotropic) Y=288ln(0.025$\langle t \rangle$), (isotropic) Y=49ln(0.009$\langle t \rangle$), and (quench) Y=12ln(0.013$\langle t \rangle$).

Feedback control using anisotropic fields displays an obvious superior capability for rapidly generating perfect circular crystals compared to benchmarks. To understand the advantages of the new approach, we first discuss results from benchmarks. For the case of a constant isotropic field quench, less than ~15% of trajectories relax into perfect crystals in 500s (Fig. 3-4C). This shows structures do not easily relax via GB diffusion without intervention, which is consistent to weak driving forces and slow dynamics on shallow free

energy landscape gradients.[59] This uncontrolled case does not produce 100% perfect crystals on experimental timescales (microscopy or computer experiments). Because the majority of trajectories never relax into perfect crystals, assembling perfect crystals on short times requires some type of control.

A previously reported method for optimal feedback control based on isotropic fields provides an important benchmark in terms of performance and concept. This approach employs isotropic fields with varying inward radial compression (Fig. 3-4B), to control melting and re-crystallization,[38] has a ~50% success rate in 500s. The optimal scheme using only isotropic fields represents a critical improvement in that it guarantees perfect crystals in 100% of trials compared to the small yield in the uncontrolled quench. The average crystallization time for the uncontrolled case is unbounded since many trajectories never crystallize, so in this respect controlling isotropic compression represent an essentially infinite improvement compared to the uncontrolled case. This case provides the most relevant direct benchmark for comparing with the new feedback control method and policy. We are aware of other approaches to feedback controlled assembly,[89-90] but not for field based actuators and an objective of assembling perfect crystals.

The new approach developed in this work (Fig. 3-4A), using anisotropic fields to assist GB motion with the RL optimized policy, has a 100% success rate at producing perfect circular crystals within ~100s, which is ~10x faster than the best prior feedback control method using isotropic fields. Because our prior approach using isotropic fields produced circular crystals, we made this part of the current control objective. However, if we had only specified perfect crystal microstructures, then the performance would be even faster without the morphology correction step. In any case, the previous feedback control

was optimal for isotropic fields, and produced perfect crystals 100% of the time, but the new approach using anisotropic fields provides a non-trivial order of magnitude improvement.

A statistical analysis of many feedback controlled trajectories (from Fig. 3-4A) also reveal trends about the number of cycles necessary to remove GBs and restore circular morphologies. In 10^3 simulated control experiments, the number of times the GB removal policy was called to remove defects was 1 (15%), 2 (50%), 3 (28%), 4 (4%), 5 (1%), and 6 (<1%). No controlled trajectories were observed where the GB removal policy was called >6 times. In microscopy experiments, results were similar except 2% of trajectories required 6 cycles to remove GBs, but this could be due to less statistics. For morphology control, >98% of simulated experiments yielded circular crystals after calling the morphology restoration policy one time. The other 2% of trajectories did not require morphology control because the final state after GB removal was already circular. Practically, for perfect crystals after grain boundary removal, morphology control was essentially deterministic, which appears to be the reason for one cycle being sufficient for restoring circular morphologies.

Given the success our new approach for creating perfect crystals of 300 particles, it is important to address scaling to larger system sizes (*i.e.*, particle number, N). To investigate size effects, we first scaled the field to maintain the same thermodynamic conditions using Eqs. (3.1) and (3.2). The differential force balance underlying this thermodynamic model is based on dipole-dipole interactions averaging to zero for isotropically distributed particles, which has been shown in theory for macroscopic electrorheological fluids[61] and has been validated in experiments for three dimensional

millimeter scale electrode dimensions.[94] However, the model could be updated to include dipole-dipole interactions if they were found to be important for different conditions. The model has also been validated in our own prior work on different system sizes[45] and dimensions.[44, 84] As such, the thermodynamic model appears to be appropriate for scaling to larger system dimensions. Practically, the electrode dimensions and voltages are sized for different N using Eqs. (3.1) and (3.2) to specify solid phases with the same osmotic pressure, morphology, and peripheral density profile for any field shape (*i.e.*, arbitrary energy landscapes[84], see *SI* for details). Simplification of this model for specific cases in this work yields analytical expressions where the electrode gap scales as $\sim N^{1/2}$ and voltage scales as $\sim N^{3/4}$. The control update time and RL control policy are same for all system sizes.

Given the excellent agreement between microscopy and simulated experiments in Fig. 2-4, we investigate system size effects using BD simulations for 300, 600, and 900 particles (Fig. 3-5, Fig. 3-15**)**. For each size, 10^3 controlled trajectories are summarized by instantaneous and cumulative yields of perfect circular crystals vs. time (Fig. 3-5A-C). Representative configurations in isotropic and anisotropic fields is also reported (Fig. 3-5D), as well as, perfect crystal yield vs. mean time for each system size (Fig. 3-5E) and system size dependence vs. mean time for fixed perfect crystal yields (Fig. 3-5F). Average crystallization times, obtained by averaging cumulative crystallization trajectories up to 100%, are 72s (N=300), 110s (N=600), and 129s (N=900). In short, the current control method produces 100% perfect circular crystals on the order of ~100s, which demonstrates its general effectiveness for different system sizes.

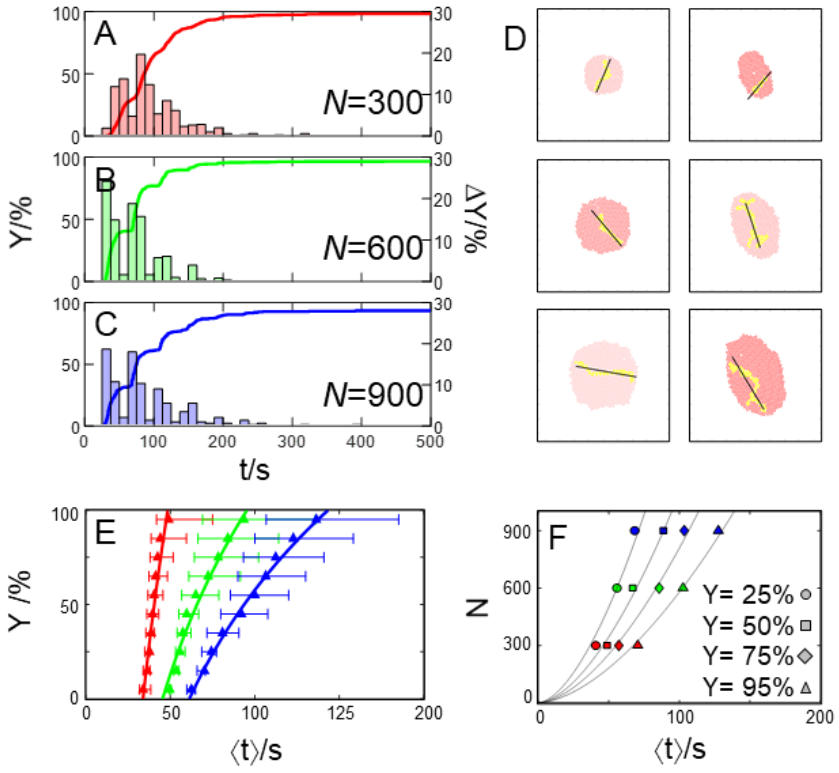

Figure 3-5 **Feedback controlled morphing energy landscape control vs. system size.** Instantaneous (Y, bars) and cumulative (ΔY, line) yields of defect-free circular crystals vs. time for computer simulations of system sizes including: (**A**) *N*=300, (**B**) 600, and (**C**) 900 particles. Example controlled trajectories for 600 and 900 particles are shown in **Fig. S10; Movies S8, S9**. (**D**) Representative renderings of GBs and crystal morphology for different system sizes on (left) isotropic energy landscapes and (right) anisotropic energy landscapes for electrode gap dimensions of 100μm, 140μm, and 170μm. (**E**) Cumulative defect-free circular crystal yield vs. average time (same as Fig. 4D) for each system size in A-C (same coloring). Logarithmic fits to each case are given by: (N= 300) Y=288ln(0.025⟨t⟩), (N=600) Y=134ln(0.022⟨t⟩), and (N=900) Y=117ln(0.016⟨t⟩). (**F**) Average time to achieve cumulative defect-free circular crystal yields given by power law fits as: (25%, circle) N=0.74⟨t⟩$^{1.67}$, (50%, square) N=0.51⟨t⟩$^{1.67}$, (75%, diamond) N=0.38⟨t⟩$^{1.67}$, and (95%, triangle) N=0.27⟨t⟩$^{1.67}$.

The time to obtain perfect crystals via GB removal with the new feedback control approach increases with increasing system size. The system size dependence on GB removal time scales ($\langle t \rangle \propto N^{3/5}$; inverting $N \propto \langle t \rangle^{5/3}$) is slightly greater than the $N^{1/2}$ system size dependence of the electrode dimensions. However, GB dynamics should not obviously follow similar scaling to thermodynamic quantities.[59] GB removal requires migration from crystal interiors to edges, where this distance is proportional to the crystal radius, which scales as $N^{1/2}$ for circular morphologies. This scaling might account for similar GB removal

time scales. The observed bias to a greater power likely results from additional effects including multiple GBs/domains and more complex non-circular shapes.[45] The current control approach is partially based on orienting fields relative to GBs, which is less well defined for multiple domains. As we noted when investigating field orientations, all anisotropic field orientations promoted faster GB relaxation compared to isotropic fields. Despite additional complexity of multiple domains/GBs, GB removal times fit a consistent scaling up to the largest size investigated.

Our new feedback approach rapidly generates perfect circular crystals of up to ~10^3 particles, and nothing suggests the trend will not extrapolate to larger systems. Given GB removal time increases for larger system sizes, eventually these times may become impractically large. Further scaling-up beyond some threshold crystal size might be achieved through adaptation of the approach here to subdomains within larger crystals. For example, the approach here could be parallelized on an electrode array[78-81] to work on local regions of larger crystals. Another approach could involve spatially translating fields through crystals in a manner analogous to zone refining. In general, the approach in this work can be scaled effectively in local microscopic systems of increasing size, but eventually creating very large crystals would require adapting the current approach to include some spatial addressability to operate on different regions within larger crystals. In any case, given the unprecedented nature of the feedback control method developed here, it seems there are opportunities for further development including scale-up to larger systems.

In conclusion, we developed a new feedback controlled approach using morphing energy landscapes to remove GBs and produce circular shapes in colloidal crystals. We

demonstrated this approach in microscopy and simulation experiments for colloidal particles in AC electric fields, although the reported approach is generalizable to any morphing energy landscape. We discovered how easily accessible energy landscape shapes and orientations together could enhance coupled GB and crystal morphology relaxation processes. Based on this finding, RL was used to develop an optimized control policy to close the loop between sensing states and actuating morphing energy landscapes to rapidly and reliably produce defect-free circular crystals.

The resulting optimized control enabled by morphing energy landscapes is superior to benchmarks and is scalable to different system sizes. Statistical comparisons of controlled stochastic trajectories quantify the speed and accuracy of producing defect-free circular crystals, where: (1) feedback controlled morphing energy landscapes produces perfect crystals an order of magnitude faster than feedback controlled isotropic landscapes, and (2) both feedback controlled methods are dramatically faster than the nearly unbounded times required for uncontrolled relaxation of defective crystals into perfect structures. The key element provided by morphing energy landscapes that enables rapid creation of perfect crystals is the ability to exert anisotropic stresses to control crystal defects/shapes without melting, which is inherently faster than repeated melting/freezing (disassembly/assembly) processes. Finally, this new control approach is scalable to different system sizes, with average times for creating defect-free circular crystals increasing as $N^{0.5}$. In short, morphing energy landscapes in conjunction with optimized feedback control can assemble defect-free colloidal crystals with non-trivial improvements to speed and scaling compared to state-of-the-art methods.

Future work could extend the scalability of our approach, most likely without the

need for higher fidelity control. Addressing multiple crystals on electrode arrays, or any periodic landscape, via parallel and serial combinations of our control approach, could be used to merge adjacent crystals into larger crystals or to create hierarchical patterned crystal structures. Given the success of elliptically shaped landscapes in this work, it is not obvious that more complex shaped landscapes would improve speed or reliability. For example, even in the limit of individually controlling every particle on highly complex landscapes, limitations due to cooperative re-arrangement processes would not obviously allow for faster net processes than coarse control of directional stresses within crystals via local field anisotropy. Another extension of this work could include controlling assembly of anisotropic colloidal particles, which have additional complexities due to additional orientational degrees of freedom important to equilibrium and non-equilibrium structures as well as defects. Finally, other potential future directions include adapting our method to three dimensional target structures as well as using crystal optical responses (*e.g.*, diffraction) as sensors for desired states. Ultimately, controlling locally repeating shapes on periodic landscapes could produce many defect-free local structures that collectively lead to a global defect-free hierarchical structure.

3.4 Methods

Control cell. Coplanar octupole Au thin film electrodes were patterned on glass microscope coverslips after cleaned with acetone (30 min), isopropanol (30 min), Nochromix (1h), and 0.1 M KOH (30 min). The coverslips were rinsed with DI water and dried with N_2 before use. The electrodes were fabricated by spin coating photoresist (S1813, Shipley) onto microscope cover slips, UV exposure through a photomask, and physical vapor deposition of a 15 nm chromium adhesive layer and a 35 nm gold layer.

The photoresist liftoff was accomplished with agitation in 1165 Remover (Shipley). To construct batch cells, PDMS O-rings (Corning, d=10mm) were coated with vacuum grease and sealed between the coverslip with the electrode and a glass coverslip. 100 μL of nominal 2.34 μm diameter silica colloids (Bangs Laboratories) were added to the batch cell before sealing it. 22 gauge copper wires were attached to the electrode using conductive carbon tape. The electrode was then connected in series with a dual-channel function generator (Agilent 33220) (Fig. 3-1A).

Microscopy. Microscopy was performed on an inverted optical microscope with a 63× Zeiss air objective lens (0.6 numerical aperture) at 1.25 magnification. A 12-bit CCD camera captured 336 pixel × 256 pixel (104 μm × 79 μm) digital images at rate of 10 frames/s. Image capture and analysis were performed using MATLAB Image Processing and Image Acquisition Toolboxes. Image analysis algorithms coded in MATLAB were used to simultaneously locate and track particle centers, as well as, compute reaction coordinates in real time.

Simulations. BD simulations, which previously matched to experiments,[59] were used to compare with experiments and test additional conditions. Particle elevations above the substrate are fixed to their most probable value based on a balance of gravitational and electrostatic particle-wall interactions. This simulation time step is 0.1ms, and the remainder of the parameters used in the simulations are reported in Table 1. To obtain initial configurations of self-assembly, the particles were randomly placed in the electric field, quenched under isotropic field using crystallization voltage, and held for 50s. The process is restarted if the configuration failed the starting configuration criterion (ψ_6<0.6).

Table 3-1 **Model parameters based on prior experiments**. (a) Particle radii, (b) medium dielectric constant, (c) Debye length, (d) Clausius-Mossotti factor, (e) zeta potential, (f) electrode gap.

Parameter	equation	value	parameter	equation	value
a (nm)[a]	S2, S4, S5	1000	f_{cm}[d]	S2, S5	-0.47
ε_m[b]	S2, S4	78	ψ (mV)[e]	S4	-75
κ^{-1} (nm)[c]	S4	10	T (K)[f]	S4	300

Control Policies. RL, specifically Q-learning, was used to obtain the optimal anisotropic policy. The controlled system is characterized by a state space (S), and the control actions forms the action space (A). A score table, $Q(s, a)$, is defined to reflect the preference of applying an action $a \in A$ at a state $s \in S$. Optimal control policies for two objectives are learned separately with RL. For GB removal, the state space is defined by global crystallinity (ψ_6) and grain orientation (γ), while for morphology relaxation, the state space is defined by circularity (c) and morphology orientation (ϕ). Crystallinity and circularity are discretized by 0.2, and GB and morphology orientations are discretized by 15º. In both policies, the action space consists of all combinations of anisotropic field shapes and orientations (Fig. 3-3A). Initially, actions are unbiased, *i.e.* $Q(s, a) = 0$. During learning, control actions are chosen at the beginning of each period (T) either randomly with 50% probability or by the highest Q score. A reward (R) is given at the end of every period to evaluate the outcome of the chosen control action. By observing a control period, the Q-score is updated as,[95]

$$\Delta Q(s_T, a_T) = \left[N(s_T, a_T)\right]^{-0.51}\left[R(s_{T+1}) + 0.5 \cdot \max_i Q(s_{T+1}, a_i) - Q(s_T, a_T)\right] \qquad (3.3)$$

where s_T is the state at the beginning of control period, and a_T is the chosen control action, $R(s_{T+1})$ is the reward calculated based on the period ending state, s_{T+1}, and $N(s_T, a_T)$ is the number of times state s_T and action a_T has been visited. Learning terminates when $\Delta Q(s,$

a) < 0.01 for all (*s*, *a*), indicating further updates are negligible. For GB removal, reward is defined as,

$$R\left(s_{T+1}\right)=1-\psi_{6,T+1}^{2} \tag{3.4}$$

where $\psi_{6,T+1}$ is crystallinity at the period end. For morphology control, reward is defined as,

$$R\left(s_{T+1}\right)=1-c_{T+1}^{2} \tag{3.5}$$

where c_{T+1} is morphology circularity at the period end. Rewards indicate effectiveness of the chosen control action towards achieving the control objective, and therefore crystallinity and circularity are chosen as metrics. Nonlinear expressions are used to better distinguish crystals with intermediate to high crystallinity and circularity values, where the most challenging control situations arise. For GB removal, configurations with low crystallinity (*e.g.* $\psi_6 < 0.4$) are rarely observed and rapidly resolved. Intermediate and high crystallinity values often possess complex defect structures and. The same is true for morphology control, where extremely anisotropic clusters (*e.g.* $c < 0.5$) are less common than nearly circular morphologies. The final optimized policies are plotted in Fig. 3-3A and listed in Table 2.

Table 3-2 Policy to obtain perfect, isotropic crystals

given N particles in isotropic field	$V_1 = V_2 = V(N)$ from **Eq. S29**
loop until both control objectives are met,	exit if ψ_6>0.99 and c>0.99
if grain boundary exists, use **Table 3** policy	if ψ_6<0.99, go to **Table 3** policy
if morphology not circular, use **Table 4** policy	if ψ_6>0.99 and c<0.99, go to **Table 4** policy

Table 3-3 Policy to obtain perfect crystal microstructure; remove grain boundaries (ψ_6<0.99)

loop with update time, Δt_C	
endpoint detection every 1s,	exit to **Table 2** policy if ψ_6>0.99
for first half period, use anisotropic field,	$V_1 \neq V_2$ if $t < 0.5\Delta t_C$
orientation parallel to GB	$\alpha = \lvert\gamma - \beta\rvert < 45^o$
field shape according to ψ_6	v=0.4 (ψ_6<0.8) or v=0.6 ($\psi_6 \geq 0.8$)
voltage found by theory	$V_{1,2}(N,v)$ from **Eq. S29**
for second half period, use isotropic field	$V_1 = V_2$ if $t > 0.5\Delta t_C$
voltage found by theory	$V_{1,2}(N)$ from **Eq. S29**

Table 3-4 Policy to obtain circular crystal morphology; remove shape anisotropy (c<0.99)

loop with update time, Δt_C	
endpoint detection every 1s,	exit to **Table 2** policy if c>0.99
for first half period, use anisotropic field,	if $t < 0.5\Delta t_{C,CM}$
orientation normal to morphology	$\theta = \lvert\varphi - \beta\rvert > 45^o$
field shape with fixed aspect ratio	v=0.4
voltage found by theory	$V_{1,2}(N,v)$ from **Eq. S29**
for second half period, use isotropic field	$V_1 = V_2$ if $t > 0.5\Delta t_C$
voltage found by theory	$V_{1,2}(N)$ from **Eq. S29**

3.5 Nomenclature

a	particle radius	v	voltage ratio between V_{min} and V_{max}
a_{eff}	effective radius of particle	$V_{1,2}$	voltages applied to electrodes
a_c	morphology acylindricity	V_{max}	max of the applied voltages
a_T	control action of period T	V_{min}	min of the applied voltages
c	morphology circularity	u^d_{ij}	induced dipolar interaction
c_E	field circularity	u^e_{ij}	electrostatic repulsion
C^i_6	local six-fold connectivity	u^{pf}_i	particle-field interaction
$\langle C_6 \rangle$	average six-fold connectivity	u^{pp}_{ij}	particle-particle interaction
d_g	electrode gap width	Y	yield of crystals
$d_{g,ref}$	reference gap width	Z	compressibility factor
e	elemental charge	$Z_{HD,F}$	compressibility factor of fluid phase
E	electric field magnitude	$Z_{HD,S}$	compressibility of solid phase
E_0	reference field magnitude	α	grain orientation relative to field
$\tilde{E}$	normalized electric field magnitude	β	anisotropic field orientation

f_{cm}	Clausius-Mossotti factor	γ	grain orientation in lab coordinate
F_i	net conservative force	ε_m	dielectric constant of medium
I	electric field second moment tensor	η	local particle area fraction
$I_{x,y}$	diagonal terms in moment of field	η_{CP}	area fraction of close-packed crystal
kT	thermal energy	η_{eff}	effective area fraction of particle
N	number of particles	η_m	area fraction of melting transition
N_c^i	coordination number	θ	morphology-field orientation
N_{ref}	reference number of particles	θ_{ij}	particle angle in lab coordinate
r_{ij}	distance between particle i and j	κ	inverse Debye length
R	ensemble length	Π	osmotic pressure
$\tilde{R}$	normalized ensemble length	ρ	number density of particle
R_g	particle radius of gyration	φ	morphology lab orientation
R_T	reward of control period T	ψ_6	global crystallinity parameter
S	particle gyration tensor	ψ_6^i	local crystallinity parameter
S_T	system state of control period T	Ψ	colloid surface potential
$S_{x,y}$	particle gyration tensor terms	χ_6^{ij}	crystalline connectivity

3.6 Theory

3.6.1 Colloidal Interactions

The net conservative force, F_i, acting on particle i is given by,[38]

$$F_i = \nabla\left[u_i^{pf} + \sum_{j\neq i} u_{ij}^{pp}\right] \tag{3.6}$$

where the first term is the interaction between external field and particle and given as,

$$u^{pf}(x,y) = -2\pi\varepsilon_m a^3 f_{cm} E^2(x,y) \tag{3.7}$$

where (x, y) is the particle coordinate, ε_m is the medium dielectric constant, a is the particle radius, f_{cm} is the Clausius-Mossotti factor, and $E(x, y)$ is the electric field magnitude. The second term is the particle-particle pair-interaction, which in this study can be expressed as,

$$u_{ij}^{pp} = u_{ij}^{e} + u_{ij}^{d} \tag{3.8}$$

where the first term is the electrostatic repulsion between particle *i* and *j* and is given as,[59]

$$u_{ij}^{e} = 32\pi\varepsilon_m a\left(\frac{kT}{e}\right)^2 \tanh^2\left(\frac{e\Psi}{4kT}\right)\exp\left[-\kappa\left(r_{ij}-2a\right)\right] \tag{3.9}$$

where r_{ij} is the center-to-center distance between the particles, e is the elemental charge, Ψ is the colloid surface potential, and κ is the inverse Debye screening length. The second term is the field-induced dipolar interaction and is given by,[59]

$$u_{ij}^{d} = -\pi\varepsilon_m a^3 f_{cm}^2 P_2\left(\cos\theta_{ij}\right)\left(\frac{2a}{r_{ij}}\right)^3 E\left(x,y\right)^2 \tag{3.10}$$

where $P_2(\cos\theta_{ij})$ is the second Legendre polynomial, and θ_{ij} is the angle between the line that connects the two particle centers and the electric field.

3.6.2 Colloidal Phase Behavior on Energy Landscapes

In our previous work we have shown the general relationship between particle density distribution and the applying external field.[84] The two-dimensional osmotic pressure, $\Pi(\rho)$, for hard disk colloids is given by the equation of state as,[44]

$$\Pi\left(\rho\right) = kT\rho Z\left(\rho\right) \tag{3.11}$$

where ρ is the particle number density and Z is the compressibility factor. For hard disk model, the compressibility factor is given as,

$$\begin{aligned} Z_{HD,\mathrm{F}}\left(\eta_{eff}\right) &= \left(1+\frac{\eta_{eff}^2}{8}\right)\left(1-\eta_{eff}\right)^{-2} && \eta_{eff} < \eta_f \\ Z_{HD,\mathrm{S}}\left(\eta_{eff}\right) &= 2\left(\frac{\eta_{CP}}{\eta_{eff}}-1\right)^{-1} + 0.67\left(\frac{\eta_{CP}}{\eta_{eff}}-1\right)+1.9 && \eta_{CP} > \eta_{eff} > \eta_m \end{aligned} \tag{3.12}$$

where $Z_{HD,F}$ is the fluid compressibility factor valid from infinite dilution up to the freezing transition, η_f=0.69, and $Z_{HD,S}$ is the solid compressibility factor valid from melting transition, η_m=0.71, up to close packing at η_{CP}=0.906. η_{eff} is effective area fraction given as,

$$\eta_{eff} = \pi a_{eff}^2 \rho \tag{3.13}$$

where a_{eff} is the effective radius of particles which accommodates the pair-wise electrostatic repulsion interaction and is given as,[10]

$$2a_{eff} = 2a + \int_{2a}^{\infty} \left[1 - \exp\left(-u^e\left(r\right) / kT \right) \right] dr \tag{3.14}$$

Eq. (2.6) can be rewritten by combining Eq. (3.12)-(3.14) as,

$$\Pi\left(\eta_{eff}\right) = kT \frac{\eta_{eff}}{\pi a_{eff}^2} Z_{HD}\left(\eta_{eff}\right) \tag{3.15}$$

which relates the colloidal osmotic pressure to the effective area fraction. Under a 2D external energy landscape, differential changes in local osmotic pressure are given by partial differential force balances as,

$$\frac{\partial \Pi\left(x,y\right)}{\partial x} = -\frac{\partial u^{pf}\left(x,y\right)}{\partial x} \cdot \rho\left(x,y\right), \;\; \frac{\partial \Pi\left(x,y\right)}{\partial y} = -\frac{\partial u^{pf}\left(x,y\right)}{\partial y} \cdot \rho\left(x,y\right) \tag{3.16}$$

which can be integrated with respect to x and y, and add together to give,

$$\int \frac{\partial \Pi\left(x,y\right)}{\partial x} \cdot dx + \int \frac{\partial \Pi\left(x,y\right)}{\partial y} \cdot dy = -\int \rho\left(x,y\right) \frac{\partial u^{pf}\left(x,y\right)}{\partial x} \cdot dx - \int \rho\left(x,y\right) \frac{\partial u^{pf}\left(x,y\right)}{\partial y} \cdot dy \tag{3.17}$$

which, by chain rule of total derivatives, can be simplified as,

$$\int d\Pi(x,y) = -\int \rho(x,y) \cdot du^{pf}(x,y) \tag{3.18}$$

which indicates that 2D differential changes in local osmotic pressure can be related to differential changes in the local energy landscape and the local density. Inserting the equation of state given by Eq. (2.10) into Eq. (2.16) and re-arranging gives,[84]

$$\int_{\eta_0}^{\eta_{eff}(x,y)} \frac{1}{\eta} d\left(\eta \cdot Z_{HD}\right) = -\frac{1}{kT}\left(u^{pf}(x,y) - u_0^{pf}\right) \tag{3.19}$$

where the left-hand side is integrated from a reference density, η_0, to the density at position (x, y), η (x, y), and the right-hand side is integrated from the reference energy, $u^{pf}{}_0$, to the same energy landscape position, $u^{pf}(x, y)$. Eq. (3.2) indicates particle density depends only on energy landscape magnitude, and therefore the field can be related to the particle phase behavior.

3.7 Electric Field

3.7.1 Crystallization Voltage

The crystallization voltage of N particles under a specific field shape can be solved from Eq. (3.2) based on a 90-10 rule,[96] where the density decays from 90% of the maximum density to 10% in less than one particle diameter at the periphery. Using this criterion, Eq. (3.2) is re-written as,

$$\int_{0.1\eta_{cp}}^{0.9\eta_{cp}} \frac{1}{\eta} d\left(\eta \cdot Z_{HD}\right) = -\frac{1}{kT}\left[u^{pf}(R-a) - u^{pf}(R)\right] \tag{3.20}$$

where R is the furthest distance between cluster edge and center. u^{pf} is replaced by Eq. (3.7) to yield,

$$E^2\left(R-a\right)-E^2\left(R\right)=\frac{kTZ_{HD}\ln 9}{2\pi a^3\varepsilon f_{cm}} \tag{3.21}$$

The energy different on the left-hand side can be approximated as,

$$\nabla E^2\left(R\right)=\frac{kTZ_{HD}\ln 9}{4\pi a^4\varepsilon f_{cm}} \tag{3.22}$$

which suggests that the gradient of electric field squared on cluster edge is a constant to obtain a crystal phase. The electric field can be normalized as,

$$E\left(R\right)=\tilde{E}\left(\tilde{R}\right)E_0,\quad \tilde{R}=R/d_g \tag{3.23}$$

where $\tilde{R}$ is the dimensionless length of cluster, and E_0 is the magnitude of field defined as,

$$E_0=\left(V_{\min}+V_{\max}\right)/d_g \tag{3.24}$$

where $V_{\min}$ and $V_{\max}$ are the two peak-to-peak voltages applied to the octupole. The left-hand side of Eq. (3.22) can be substituted with Eq. (3.23) to give,

$$\nabla E^2\left(R\right)=d_g^{-1}\nabla_{\tilde{R}}\tilde{E}^2\left(\tilde{R}\right)E_0^2 \tag{3.25}$$

where $\nabla_{\tilde{R}}$ is the gradient operator with respect to $\tilde{R}$. Eq. (3.22) can then be rewritten as,

$$E_0=\left(\frac{kTZ_{HD}\ln 9}{4\pi a^4\varepsilon f_{cm}\nabla_{\tilde{R}}\tilde{E}^2\left(\tilde{R}\right)}\right)^{1/2}d_g^{1/2} \tag{3.26}$$

which, by substitute E_0 with Eq.(3.24), yields,

$$V_{\min} = \frac{1}{1+v}\left(\frac{kTZ_{HD}\ln 9}{4\pi a^4 \varepsilon f_{cm} \nabla_{\tilde{R}} \tilde{E}^2\left(\tilde{R}\right)}\right)^{1/2} d_g^{3/2}$$
$$V_{\max} = \frac{v}{1+v}\left(\frac{kTZ_{HD}\ln 9}{4\pi a^4 \varepsilon f_{cm} \nabla_{\tilde{R}} \tilde{E}^2\left(\tilde{R}\right)}\right)^{1/2} d_g^{3/2} \quad (3.27)$$

where v is the voltage ratio between $V_{\min}$ and $V_{\max}$,

$$v = V_{\min}/V_{\max} \quad (3.28)$$

$\nabla_{\tilde{R}}\tilde{E}$ can be solved empirically for octupole-based fields as,

$$\nabla_{\tilde{R}} \tilde{E}^2\left(\tilde{R}\right) = \exp\left[\left(17v-23\right)\tilde{R}^3 + \left(114v+126\right)\tilde{R}^2 + 28v\tilde{R} + 7v - 9\right] \quad (3.29)$$

which can be substituted into Eq. (3.27) to get the crystallization voltage for a given field shape.

3.7.2 Field Shape & Orientation

The shape and orientation of the anisotropic electric fields are defined based on the second moment of electric energy landscape, which is given as,

$$I = \frac{1}{\iint u^{pf}\left(x,y\right)dxdy}\begin{bmatrix} \iint x^2 u^{pf}\left(x,y\right)dxdy & \iint xy\cdot u^{pf}\left(x,y\right)dxdy \\ \iint xy\cdot u^{pf}\left(x,y\right)dxdy & \iint u^2 u^{pf}\left(x,y\right)dxdy \end{bmatrix} \quad (3.30)$$

where the energy landscape, $u^{pf}(x, y)$ is defined in the lab coordinate. To define the orientation of the field, the coordinate system is rotated by,

$$\begin{bmatrix} x' \\ y' \end{bmatrix} = \begin{bmatrix} \cos\beta & -\sin\beta \\ \sin\beta & \cos\beta \end{bmatrix}\begin{bmatrix} x \\ y \end{bmatrix} \quad (3.31)$$

where the angle of rotation, β, is defined as the field orientation, if the rotated second

moment matrix is diagonal,

$$I' = \frac{1}{\iint u^{pf}(x',y')\cdot dxdy}\begin{bmatrix} \iint (x')^2 u^{pf}(x',y')\cdot dxdy & 0 \\ 0 & \iint (y')^2 u^{pf}(x',y')\cdot dxdy \end{bmatrix} = \begin{bmatrix} I_x & 0 \\ 0 & I_y \end{bmatrix}$$

(3.32)

and $I_x > I_y$. β is the direction of the field major axis. The field shape is defined as,

$$c_E = \frac{\sqrt{I_x} - \sqrt{I_y}}{\sqrt{I_x + I_y}} \tag{3.33}$$

which is a dimensionless value that goes to one for an isotropic field.

3.7.3 System Size Dependent Fields

To control the self-assembly of different numbers of particles, both the width of electrodes and the magnitude of applied voltages need to be adjusted accordingly. The dependency of voltage on particle number and voltage ratio is shown in Fig. 3-6A. where the marked cases are rendered in Fig. 3-6B-G. To solve for the voltages, the electrode width is first scaled according to,

$$d_{g,N} = \left(\frac{N}{N_{ref}}\right)^{1/2} d_{g,ref} \tag{3.34}$$

where N_{ref}=300 and $d_{g,ref}$=100μm is considered as the reference system. With such choice of electrode scale-up, a constant field circularity is maintained for each voltage ratio (Fig. 3-6H), which yield comparable and consistent driving force for the self-assembly control of different particle numbers. Given the electrode width, crystallization voltages can be found by substituting Eq. (3.34) into Eq. (3.27) as,

$$V_{\min,N} = \frac{1}{1+v}\left(\frac{N}{N_{ref}}\right)^{3/4}\left(\frac{kTZ_{HD}\ln 9}{4\pi a^4 \varepsilon f_{cm}\nabla_{\tilde{R}}\tilde{E}^2\left(\tilde{R}\right)}\right)^{1/2} d_{g,ref}^{3/2}$$
$$V_{\max,N} = \frac{v}{1+v}\left(\frac{N}{N_{ref}}\right)^{3/4}\left(\frac{kTZ_{HD}\ln 9}{4\pi a^4 \varepsilon f_{cm}\nabla_{\tilde{R}}\tilde{E}^2\left(\tilde{R}\right)}\right)^{1/2} d_{g,ref}^{3/2} \quad (3.35)$$

Another merit of using Eq. (3.34) as the scale-up criterion is that the fitted parameter of $\nabla_{\tilde{R}}\tilde{E}$ (Eq. (3.29)) is independent of system size. This is because both the electrode width and characteristic cluster length both scale as $N^{1/2}$, so their ratio, the dimensionless cluster length, is constant.

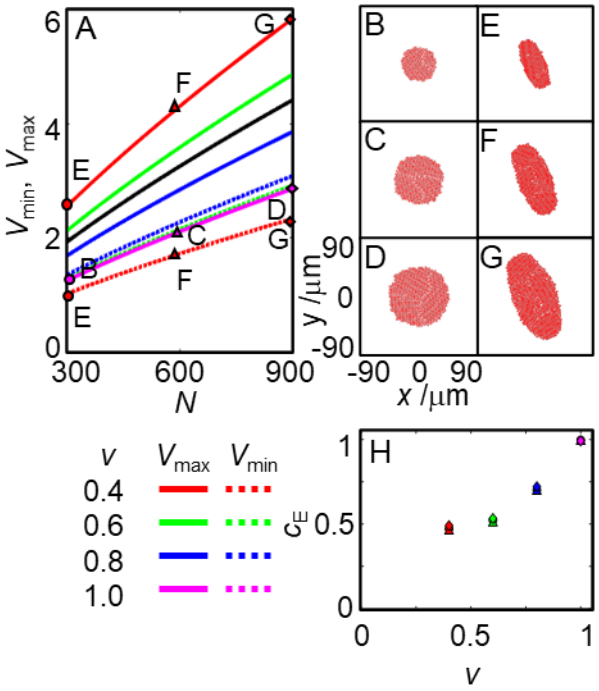

Figure 3-6 **Octupole voltages for scaled-up system sizes.** (A) Crystallization voltages at different field shapes and system sizes as calculated by Eq. (3.35). The electrode width scaled with $N^{1/2}$ (Eq. (3.34)). Markers represent the crystallization voltages of isotropic (pink) and v=0.4 anisotropic (red) field for N=300 (circle), 600 (triangle), and 900 (diamond) particles. (B-D) Renderings of N=300, 600, and 900 particles from simulation under corresponding isotropic fields. (E-G) Renderings of N=300, 600, and 900 particles under anisotropic (v=0.4) fields. (H) field circularity as a function of field shape and system size. The circularity is given by Eq. (3.33). Field shapes, in terms of voltage ratio v, are v=0.4 (red), 0.6 (green), 0.8 (blue), and 1 (pink). System sizes are N=300 (circle), N=600 (triangle), and N=900 (diamond).

3.7.4 Reaction Coordinates

3.7.4.1 Crystallinity Parameters

The global six-fold bond orientational order, ψ_6, is defined as,[97]

$$\psi_6 = \left| \frac{1}{N} \sum_{i=1}^{N} \psi_6^i \right| \tag{3.36}$$

where N is the total number of particles, and ψ_6^{i} is the local six-fold bond orientational order for each particle i, given by,

$$\psi_6^i = \frac{1}{N_c^i} \sum_{j=1}^{N_C^i} e^{i6\theta_{ij}} \tag{3.37}$$

where $N_{\mathrm{c}}^{\mathrm{i}}$ is the number of coordinated neighbors within the first coordination radium of particle i, and θ_{ij}, which as the same definition as in Eq. (2.5), is the angled between particle i and j and the lab coordinate given as,

$$\theta_{ij} = \tan^{-1}\left(\frac{y_i - y_j}{x_i - x_j} \right) \tag{3.38}$$

The crystalline connectivity, χ_6^{ij}, between particle i and j is defined as,

$$\chi_6^{ij} = \frac{\left| \mathrm{Re}\left[\psi_6^i \psi_6^{j^*} \right] \right|}{\left| \psi_6^i \psi_6^{j^*} \right|} \tag{3.39}$$

where $\psi_6^{\mathrm{j}^*}$ is the complex conjugate of ψ_6^{j}. The local six-fold connectivity $C_{6,\mathrm{i}}$ can be calculated by,[98]

$$C_{6,i} = \frac{1}{6} \sum_{j=1}^{N_c^i} \left[\begin{vmatrix} 1 & \chi_6^{ij} \geq 0.32 \\ 0 & \chi_6^{ij} < 0.32 \end{vmatrix} \right] \tag{3.40}$$

and the global six-fold connectivity, C_6, of the ensemble is given by,

$$C_6 = \frac{1}{N}\sum_{i=1}^{N} C_{6,i} \tag{3.41}$$

3.7.4.2 Morphology Parameters

The shape and orientation of the particle ensemble are defined similar to those of the electric field based on the particle gyration tensor, which is given as,[88]

$$S = \frac{1}{N}\begin{bmatrix} \sum_i x_i^2 & \sum_i x_i y_i \\ \sum_i x_i y_i & \sum_i y_i^2 \end{bmatrix} \tag{3.42}$$

where the coordinates are defined in the lab coordinate, and, similar to Eq. (3.31), can be rotated by,

$$\begin{bmatrix} x_i' \\ y_i' \end{bmatrix} = \begin{bmatrix} \cos\varphi & -\sin\varphi \\ \sin\varphi & \cos\varphi \end{bmatrix}\begin{bmatrix} x_i \\ y_i \end{bmatrix} \tag{3.43}$$

where the rotation angle, φ, is the orientation of morphology, if the rotated gyration tensor is diagonal,

$$S' = \frac{1}{N}\begin{bmatrix} \sum_i (x_i')^2 & \sum_i x_i' y_i' \\ \sum_i x_i' y_i' & \sum_i (y_i')^2 \end{bmatrix} = \begin{bmatrix} S_x & 0 \\ 0 & S_y \end{bmatrix} \tag{3.44}$$

and $S_x > S_y$. φ is effectively the major axis direction of the morphology, and S_x and S_y are the standard deviation of particles along the major and minor axes. The relative angle between the morphology and an applied anisotropic field is given as,

$$\theta = \varphi - \beta \tag{3.45}$$

which ranges between ±90°. The shape of morphology, on the other hand, is defined by the circularity, c, as,

$$c = 1 - \left(a_c / R_g \right) \tag{3.46}$$

where R_g is the particle radius of gyration,

$$R_g = \sqrt{S_x + S_y} \tag{3.47}$$

and a_c is the morphology acylindricity,

$$a_c = \sqrt{S_x} - \sqrt{S_y} \tag{3.48}$$

The morphology circularity is a dimensionless value that goes to one for a perfect spherical cluster.

3.7.4.3 GB Coordinate

The grain particles are defined as interior particles that are not hexagonally packed, and can be identified using the crystallinity parameters as $\psi_{6,i}<0.9$ and $C_{6,i}>0.6$. The orientation of GB is defined as,

$$\gamma = \arctan\left[\frac{\sum_i \left(x_{i,g} - \langle x_g \rangle \right)\left(y_{i,g} - \langle y_g \rangle \right)}{\sum_i \left(x_{i,g} - \langle x_g \rangle \right)^2} \right] \tag{3.49}$$

where the subscripts represent the grain particle, and, and the angle brackets represent average values. γ is effectively the angle of the linear fit of grain particles. The relative angle between GB and field is given as,

$$\alpha = \gamma - \beta \tag{3.50}$$

which ranges between ±90°.

3.8 Computational Methods

3.8.1 Electric Field Modeling

The octupole electrode was modeled using the electrostatic interface in COMSOL Multiphysics software. The octupole was placed at the center on the bottom of a 400 μm by 400 μm by 20 μm rectangular chamber, which was filled with 0.1mM NaOH aqueous solution. Each electrode was modeled as a cylinder with 20 μm in diameter and 40nm in thickness, and was positioned on the vertices of an octagon with a 100 μm diagonal distance. The top view of the octupole is shown in Fig. 3-1, where the applied voltages to the electrodes are represented by grayscale fillings. A lookup table is generated with 0.25μm resolution at 1.5 μm from the chamber bottom, which is equivalent to the equatorial elevation of a 3 μm particle touching the substrate. The field is normalized by E_0 (Eq.(3.24)), so that only the spatial variation of the field, denoted as $\tilde{E}(x, y)$ in Eq. (3.23) , is recorded by the lookup table. In the Brownian Dynamics simulations, intermediate values were obtained from the look-up table by Barycentric interpolation, and used to compute energy landscapes given by Eq. (3.6).

3.8.2 Reaction Coordinates

Fig. 3-7-3-10 show color renderings of reaction coordinates explained in *Theory*. Fig. 3-7A, B shows a trajectory where the particles are held by anisotropic field (v=0.4) parallel to GB (α=2.5°) for 50s, followed by isotropic field for 50s. The particles are colored by ψ_6 (red) and $C_{6,i}$ (blue). Fig. 3-7C, D show trajectories of ψ_6 and $\langle C_6 \rangle$ given in

Eq. (3.36) and (3.41). Fig. 3-8A, B use the same trajectory to show the morphology parameters. The green arrow shows the standard deviation of particles along long and short axes of morphology orientation, which are denoted by the diagonal terms in the particle gyration tensor (Eq. (3.44)). The orientation of major axis is defined as the morphology orientation φ (Eq. (3.43)). The radii of cyan and purple circles correspond to the radius of gyration R_g (Eq. (3.47)) and morphology acylindricity a_c (Eq. (3.48)). Fig. 3-8C, D plot the trajectories of R_g, a_c, and circularity, c (Eq. (3.46)) from the same trajectory.

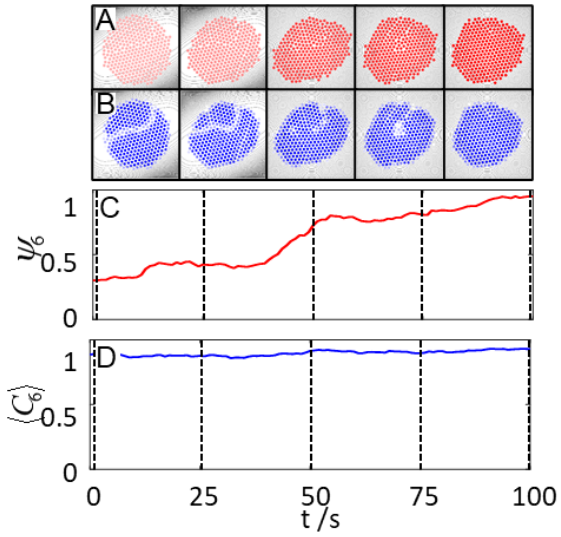

Figure 3-7 **Crystallinity reaction coordinates.** (A) Trajectory shown same as Fig. 2C, where 300 particles are quenched using anisotropic field parallel to the GB for 50s, followed by isotropic field for 50s. The particles are colored in white-red scale based on the global crystallinity ψ_6 given in Eq. (3.36) (white for $\psi_6 = 0$, red for $\psi_6 = 1$). The applied electric fields are plotted as underneath contour (B) The same trajectory colored using a white-blue scale based on the local $C_{6,i}$ given in Eq.(2.22) (white for $C_6^i = 0$, blue for $C_6^i = 1$). (C, D) trajectories of ψ_6 and C_6.

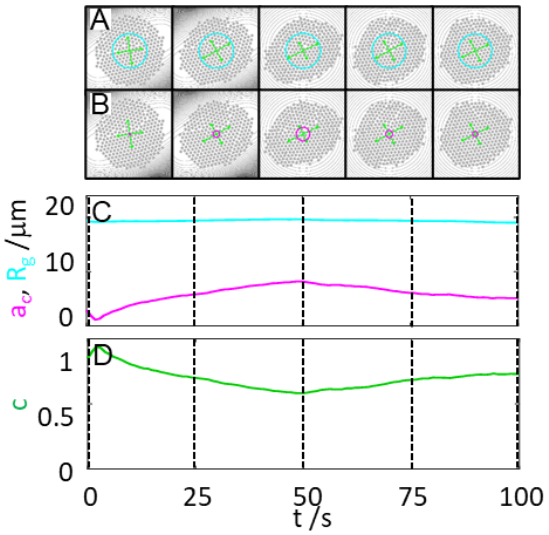

Figure 3-8 **Morphology circularity.** (A, B) Configurations obtained from the same trajectory as Fig. S2, where 300 particles are quenched using anisotropic field parallel to the GB for 50s, followed by isotropic field for 50s. The radius of gyration R_g (Eq. (3.47)) is shown by the radii of cyan circles, and acylindricity a_c (Eq. (3.48)) is shown by the radii of purple circles. The long-axis of green arrows point towards morphology orientation φ (Eq. (3.43)). The lengths of arrows correspond to the standard deviations of particles along long and short axes of morphology and are denoted by S_x and S_y in Eq. (3.44). Radius of gyration, acylindricity, and morphology circularity are all calculated based on S_x and S_y. (C, D) Trajectories of R_g and a_c and (D) Trajectory of morphology circularity c (Eq.(3.46)) are matched to configurations shown in (A,B).

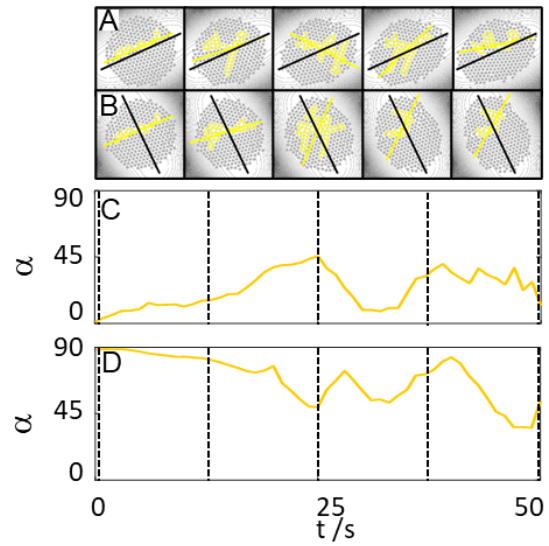

Figure 3-9 **GB orientation.** (A, B) Configurations captured from trajectories in which particles are squeezed by parallel and perpendicular anisotropic fields for 50s from an initial isotropic configuration. GB particles are colored in yellow. Field orientations β (Eq. (3.31)) are shown by the slopes of black lines, and the GB orientations φ (Eq.(3.43)) are shown by the slopes of yellow lines. (C, D) Trajectories of GB orientations relative to field orientation α (Eq. (3.50)) are plotted based on the trajectories shown in (A, B)

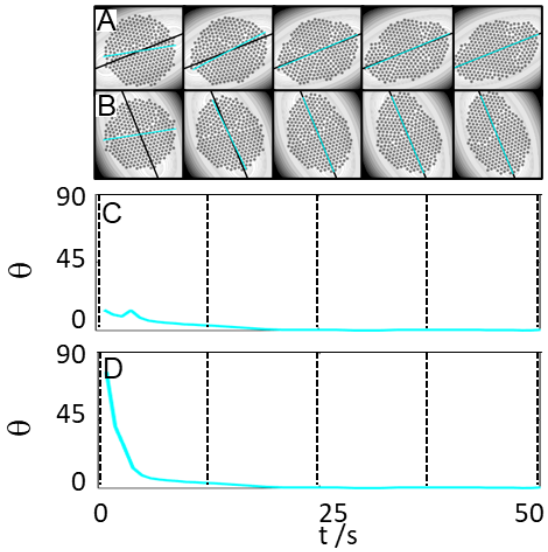

Figure 3-10 **Morphology orientation.** (A, B) Configurations captured from trajectories in which particles are squeezed by parallel and perpendicular anisotropic fields for 50s from an initial isotropic configuration. Morphology orientation φ (Eq.(3.43)) are shown by the slopes of cyan lines, and field orientations β are shown by the slopes of black lines. (C,D) Trajectories of morphology orientations relative to field orientation θ defined in Eq. (3.45).

Fig. 3-9 shows two trajectories where the particles are held by different anisotropic fields (α=2.5° and 87.5°) for 50s. The orientations of field and GB are shown by black and yellow lines, and the grain particles are colored in yellow. Fig. 3-9C, D plot the trajectories of GB angle, α, as given in Eq. (3.50), which measures the relative angle between GB and applied anisotropic field. Therefore, although the two trajectories start from the same configuration, the initial readings of α are perpendicular to each other. Fig. 3-10 use the same trajectories as Fig. 3-9 to show the orientations of morphology and anisotropic field in cyan and black lines. Fig. 3-10C, D plot the trajectories of morphology orientation, θ, as given in Eq.(3.45), which measures the relative angle between morphology and applied anisotropic field.

3.9 Control Policy Optimization

3.9.1 Control Update Time Empirical Optimization

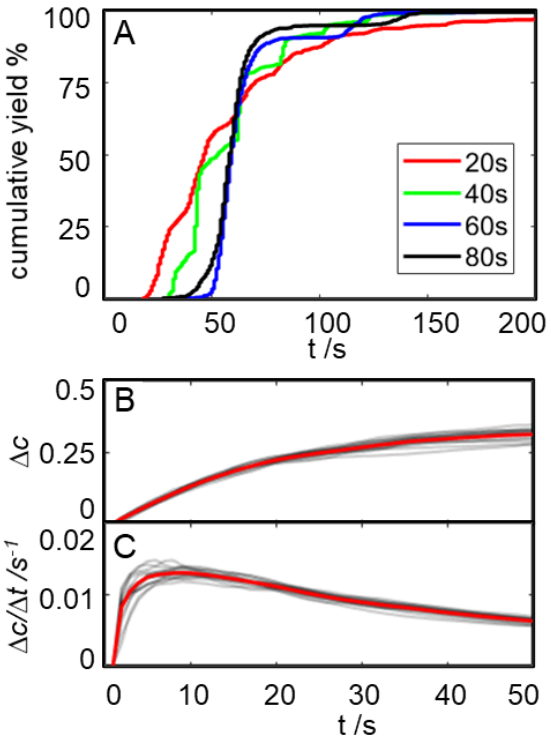

Figure 3-11 **Empirical optimization of control update time.** (A) Yield of perfect crystals as a function of time for different update time and fixed anisotropic field shape (v=0.4). (B) Change of morphology circularity as a function of time starting from circular configuration under anisotropic fields. 20 individual trajectories and their average are shown by black and red lines. (C) Rate of morphology change as a function of time after the same condition. Individual trajectories and their average are plotted in black and red curves.

Control update time was optimized by randomly alternating isotropic and anisotropic field (v=0.4) with equal time. The yield of perfect circular crystals vs. time was averaged over 1000 simulated experiments for each update time (Fig. 3-11A). The legend denotes the respective times anisotropic and isotropic half-periods. Fig. 3-11B shows the net change of circularity starting from isotropic morphologies by applying anisotropic field (v=0.4), where 20 individual trajectories (black lines) and their average (red line) are presented. Fig. 3-11C shows the rate of circularity change under the same conditions.

Perfect circular crystals have been formed with 100% yield at all update times, while the fastest assembly was achieved with an update time of 20s.

Dynamic trajectories support the observed optimal update time. Maximum morphology change was asymptotically reached at longer control times (>30s), which is desired to remove larger GBs from ensemble interior. On the other hand, the maximum rate of morphology change was observed early in the period (~10s), which allows for more frequent field changes and accelerated removal of small GBs or local defects. The optimal control update time is a combination of both factors, which is confirmed by the crystal yield trajectories (Fig. 3-11A). The earliest success was observed for an update time of 10s, which can be attributed to the rapid relaxation of small GBs. However, assembly of the last 5% required extended times, because these cycles usually consisted of configurations with larger GBs in the cluster center. An inadequate morphology change is less effective in relaxing defects. With larger period times (>30s), virtually all cycles finished within the same control period, as the yield curve rise to 100% vertically. While large GBs are removed effectively with longer periods, relaxation of minor defects was delayed.

3.9.2 Anisotropic Shape Empirical Optimization

The anisotropic field shape was optimized by using the optimal control update time and alternating between isotropic and anisotropic field in random directions. The field shape, denoted in terms of applied voltage ratios, was optimized within v=0.4-0.7. The yield of perfect circular crystals using each anisotropic field shape was averaged over 1000 cycles of simulated experiment (Fig. 3-12A). Fig. 3-12B shows the circularity of field (Eq. (3.33)) as a function of applied voltage. Fig. 3-12C shows the energy landscape of each

field shape defined by Eq. (2.2), and Fig 3-12D shows the corresponding equilibrium particle distributions as predicted from thermodynamics by Eq. (3.2).

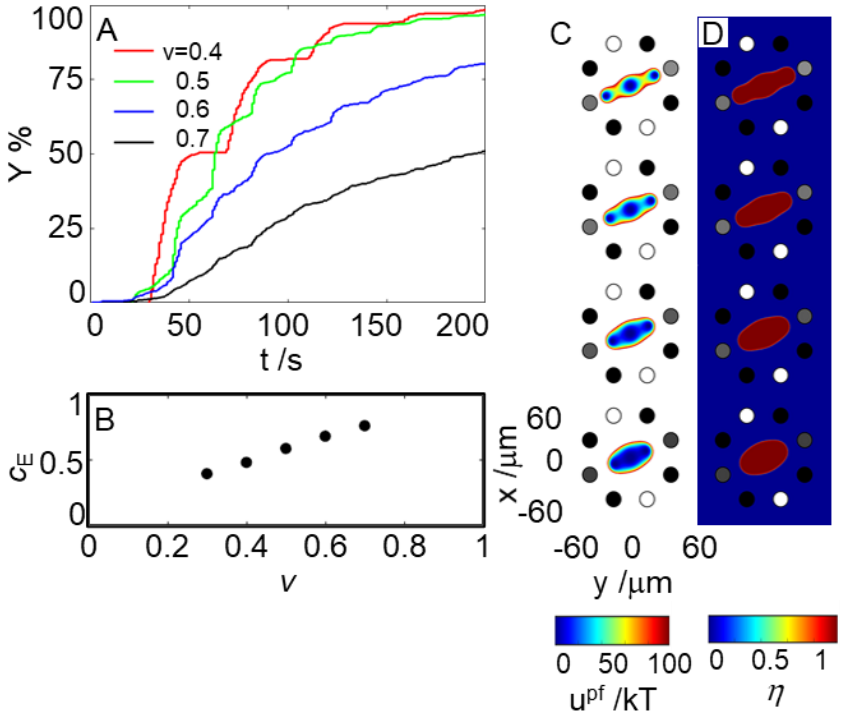

Figure 3-12 **Empirical optimization of anisotropic field shape.** (A) Yield of perfect crystals as a function of time for different anisotropic field shapes with random orientations and fixed update time (Δt=20s). (B) Field circularity (Eq. (3.33)) as a function of voltage ratio. (C) Single particle energy landscapes (Eq. (2.2)) generated with voltage ratios of v = 0.4 - 0.7. (D) Equilibrium distributions of particles predicted by Eq. (3.2) under corresponding energy landscapes.

The yield monotonically increased with decreasing field circularity and applied voltage ratio, which again confirmed that the fundamental driving force for GB removal is the alternation between isotropic and anisotropic fields. With the current electrode and number of particles, a minimum voltage ratio v=0.4 is feasible. For lower ratios, the field does form an energy well enclosing all the particles within the electrode center of, such that particles would irreversibly diffuse away. As a result, the optimal anisotropic field shape was found to correspond v=0.4.

3.10 Example Control Experiments

3.10.1 Constant Quench

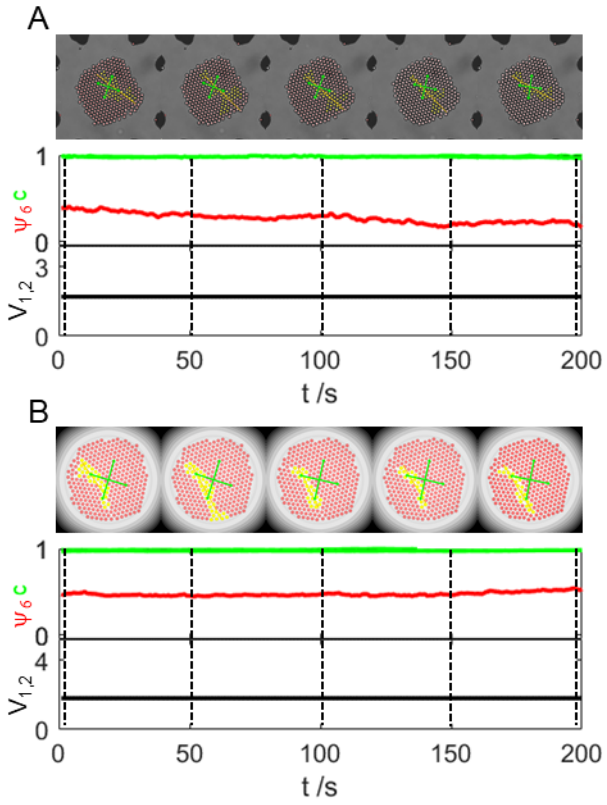

Figure 3-13 **Open loop control using constant isotropic field.** (A) Microscopy experiment including analyzed images and trajectories for global crystallinity ψ_6(red), morphology circularity c (green), and two applied voltages (black, gray). (B) Computer simulated experiment including rendered configurations on underlying gray scale energy landscapes and same information in (A). In images, particles are colored using an 8-bit white-red scale to indicate degree of global crystallinity, GB particle are colored yellow, and green arrows indicate directions and relative magnitudes of shape long- and short- axes (see *Method* and *SI* for detailed calculations related to coloring particles).

Constant quench policy represented an open loop, uncontrolled process of colloid self-assembly, in which particles are held under a constant isotropic field until a perfect crystal is formed or time exceeds. To make fair comparisons with other policies, the initial structure was set as ψ_6<0.6, and a perfect crystal is defined as ψ_6>0.99 and c>0.99. Individual renderings from microscopy (Fig. 3-13A) and simulated (Fig. 3-13B)

experiments failed to form perfect crystals within the time limit, which is not uncommon given constant field shape.

3.10.2 Optimal Closed-Loop Isotropic Control

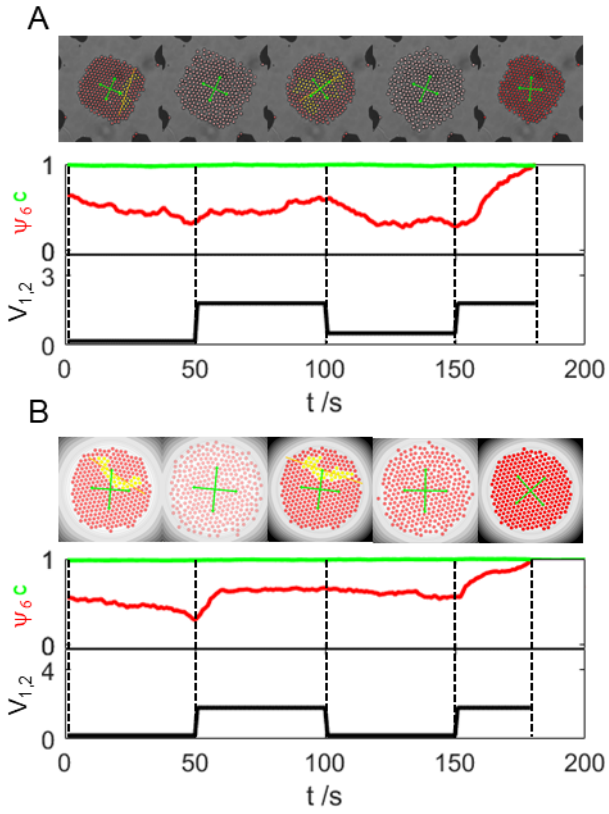

Figure 3-14 **Feedback control using optimal isotropic policy.** (A) Microscopy experiment including analyzed images and trajectories for global crystallinity ψ_6(red), morphology circularity c (green), and two applied voltages (black, gray). (B) Computer simulated experiment including rendered configurations on underlying gray scale energy landscapes and same information in (A). In images, particles are colored using an 8-bit white-red scale to indicate degree of global crystallinity, GB particle are colored yellow, and green arrows indicate directions and relative magnitudes of shape long- and short- axes (see *Method* and *SI* for detailed calculations related to coloring particles).

Optimal isotropic control policy introduced in previous works was replicated using the octupole electrode to be compared with anisotropic policy.[38] To make fair comparisons with other policies, the initial structure was set as ψ_6<0.6, and a perfect crystal is defined as ψ_6>0.99 and c>0.99. Individual renderings from microscopy (Fig. 3-14A) and simulated

(Fig. 3-14B) experiments are presented. Briefly, the policy applies isotropic fields with various magnitudes based on the system global crystallinity ψ_6 and bond connectivity $\langle C_6 \rangle$. The policy relies on periodic relaxation of condense structure to remove GBs with Brownian motion.

3.10.3 Optimal Closed-Loop Anisotropic Control for Larger System Sizes

Computer simulated experiments are conducted to investigate the scale-up problem of self-assembly using anisotropic control policy. Individual realizations for $N = 600$ (Fig. S15A) and $N = 900$ (Fig. S15B) particles are used. The control policy (Policy. 1) was same as the benchmark system of $N = 300$. The electrode width and applied voltage magnitudes were scaled according to Eq. (3.34) and (3.35), which ensured a consistent level of field anisotropy for the dynamics of grain removal, and a consistent cluster density for the thermodynamics of the ensemble. Otherwise, the choice of update time, field orientation, and field shape were the same.

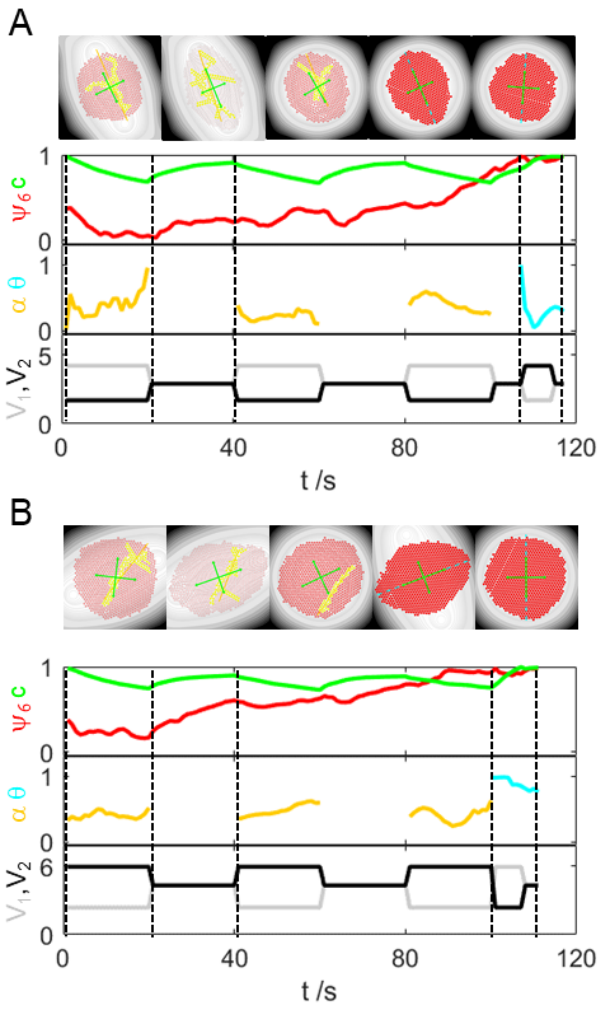

Figure 3-15 **Feedback control using optimal anisotropic policy for different system sizes.** (A) Computer simulated experiment of *N* = 600 particles using the same anisotropic control policy, which includes analyzed images and trajectories for global crystallinity ψ_6(red), morphology circularity c (green), GB orientation α (yellow), morphology orientation θ (cyan), and two applied voltages (black, gray). (B) Computer simulated experiment of *N* = 900 particles. The organization of panel is same as (A).

4 CONTROLLED HIERARCHICAL COLLOIDAL ASSEMBLY ON PERIODIC LANDSCAPES

4.1 Abstract

We report a comprehensive control process that yields hierarchical colloidal crystals with perfect crystallinity and circular morphology. We demonstrate this approach in computer simulation based on an electrode array that can be dynamically activated to generate diverse fields and energy landscapes. We proposed control steps include coarse partition of liquid phase particles into condensed clusters, redistribution of particles in to equal size clusters, removal of grain boundaries, and relaxation of circular morphology for all clusters. This approach can assemble large array of hierarchical structures of various cluster sizes. The proposed electrode array also provides a robust and reconfigurable tool to solve other assembly tasks.

4.2 Introduction

Assembly of colloidal particles into structured materials possess potential applications and properties in photonics, magnetics, and mechanics.[99-101] Spatial organization is a major challenge to many promising colloidal materials.[102-103] Homogenous close-packed colloid crystals are the most investigated structures.[104] More complex spatial organizations are investigated for non-spherical colloids, assembly on curved substrates, or colloid nanodot.[105-108] Hierarchical structure with distinct long- and short-range orders and properties is an active research territory.[109]

Many hierarchical colloid structures are inspired by biological systems.[110-112] Individual and collective behavior of colloids resemble those of active cells or biological

molecules.[113-114] Hierarchy is a critical prerequisite for biological multifunctional materials.[115-117] Bio-inspired structures have seen potential applications in drug screening, optical/electronic devices, and templated substrates.[80, 118-120] Understanding and replication of complex biological structures contributes to more knowledge regarding colloidal interactions.[121-122]

Colloid assembly approach with high resolution and great scalability is a desirable. Precise control to individual particles or small clusters, such as optical tweezers, have limited operation areas. Entropy-driven assembly, such as evaporation deposition or interfacial assembly, are most suitable for massive fabrications but often lack precision and introduce irreversible defects.[123-124] Directed assembly is often a good combination of precision and scalability.[125-126]

Pattern mediate assembly provides a robust and consistent approach to form hierarchical colloidal structures.[127-129] Colloid crystals nucleate and grow around specific sites on substrates.[130-131] Assembly are formed on topographical features, chemically modified spots, or captured interfaces on prefabricated substrates.[132-134] The pattern can be manufactured in different geometries to achieve colloidal microstructures of stripes, circles, or other shapes.[102, 135-137] Natural limitations of template-based assembly are the poor tunability of assembled structure and lack of mechanisms to resolve defects. External fields are desirable in these regards. Reversible assembly controlled using external fields achieves reconfigurable microstructures and can prevent kinetically trapped states. Electric fields are most successful with assembly of single colloid crystal or micropattern. [38, 51, 138] In a way, electric fields act like reconfigurable templates, in which particles aggregate according to spatial variation of fields. So far, most successful works of electric field

mediate assembly focus on a single cluster.[60, 139] Scalable and macroscopic colloid structures formed by electric fields is still an ongoing research topic.

In this work we present a computational study to direct assembly of hierarchical crystals based on electrode array. We generated various types of DC and MHz AC electric fields using electrode array. These electric fields enable controls to colloid phase behavior, dynamic transport process, and grain and morphology dynamics. We divided the overall approach into steps of coarse partitioning, cluster redistribution, and defect and cluster morphology control. Our approach can scale to larger system sizes and potentially infinite array of clusters. Finally, we conceptually present several possible applications based on electrode array.

4.3 Results & Discussion

4.3.1 Colloid Control over Electrode Array with DC or AC electric fields

Fig 4-1A shows simulation system setup, where orthogonal array is formed by electrodes of 5μm in width, 40nm in height, and separated by 5μm. Fig. 4-1B shows a random liquid state of N_0 = 3600 particles with 1μm radius, and Fig. 4-1C shows coarse partitioning of particles into 9 condensed clusters. Particles are colored by local C_6 values in white-to-blue scale representing liquid (C_6 = 0, white) to solid (C_6 = 1, blue) phases. Fig. 4-1D and 4-1E shows particle trajectories during cluster redistribution, where blue-to-red color scale is used to represent dynamics over one second starting from equilibrium positions. Fig. 4-1F shows a case of cluster dimension of L/S = 1/3, which consists of 9 clusters with equal sizes ($\langle N \rangle$ = 400). Grain boundary defects exist because of uncontrolled quenching. Fig. 4-1G and H shows control operations which remove grain boundaries and

relax circular morphology. Grain particles are represented in yellow color and other particles are represented in white-to-red scale according to ψ_6 values of each cluster. Cyan arrows point in the direction of morphology orientations, and the lengths is defined as (1 - c) · R, where R is the cluster radius given as $R = (\langle N \rangle \cdot a^2/\eta_{cp})^{1/2}$, a is the particle radius and η_{cp} is the close packed area fraction. The length of cyan arrow corresponds to difference from circular morphology.

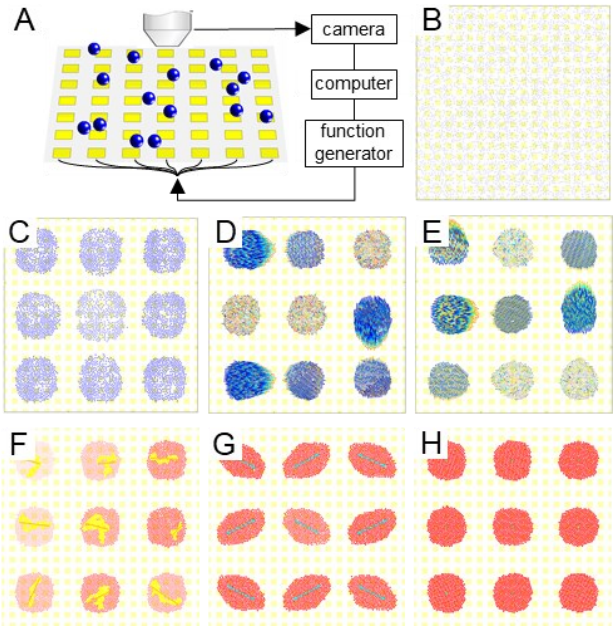

Figure 4-1 **Assembly of hierarchical colloidal crystals on electrode array.** (**A**) Schematic of colloid control on electrode array. (**B**) Initially particles are randomly dispersed with area fraction density of $\eta \approx 0.28$. (**C**) Coarse partitioning of colloids into clusters. clusters have dimension of $L/S = 1/3$. Particles are colored by local C_6 in white-blue scale. (**D, E**) Cluster redistribution and cluster size equalization. Particles redistributed between adjacent clusters in multiple steps. Trajectories are colored from blue to red as a function of time. (**F**) Control of grain boundary removal. Initially all clusters contain grain boundaries, which are represented by yellow particles. The other particles are colored in white-red scale by global ψ_6 of each cluster. Orientations of grain boundaries are marked by orange lines (**G**) Control of morphology relaxation. Initially all clusters have perfect structure and anisotropic shapes. Cyan arrows represent the direction of morphology, and the lengths represent (1 - c) · R, where c is the morphology circularity, and R is the cluster size given as $R = (Na^2/\eta_{cp})^{1/2}$. (**H**) hierarchical perfect crystals with circular morphologies.

Assembly of hierarchical perfect crystals is controlled in consecutive steps using electrode array. Each electrode can be independently activated with AC voltage and DC offset. Initially particles are randomly dispersed in the system, with a liquid phase of area

fraction $\eta \approx 0.28$. In the first step (Fig. 4-1C), particles are coarse partitioned into clusters with framing MHz AC electric field. The cluster dimension is defined in terms of L/S, where L is the dimension of cluster and S is the dimension of simulation window. Distribution of cluster sizes can be predicted by density fluctuation theory with isotherm compressibility factor. In the next step (Fig. 4-1D, E), clusters are redistributed to obtain equal sizes using directional DC electric fields. An optimal strategy to redistribute clusters is determined based on greedy optimization algorithm, which minimizes the total number of redistributed particles and the number of transfer operations. MHz AC electric fields are always applied to constrain particles in each cluster, except for the redistributed clusters. In the third step (Fig. 4-1F), the grain boundaries in all clusters are removed with alternating isotropic and anisotropic AC electric fields. Each field shape is applied for a fixed period, so that cluster morphology can be squeezed under changing fields. In previous works, we have shown that such changing fields and morphologies contribute to the diffusion of grain defects and the formation of perfect crystals. In the last step (Fig. 4-1G), the same set of isotropic and anisotropic fields are used to relax the circular morphology of each cluster. The anisotropic field perpendicular to existing morphology orientation is applied until the cluster shape is relaxed, and then isotropic field is applied to hold clusters in perfect structures. Finally, hierarchical crystals with circular shapes are obtained (Fig. 4-1H).

4.3.2 Coarse Partitioning of Particles into hierarchical clusters

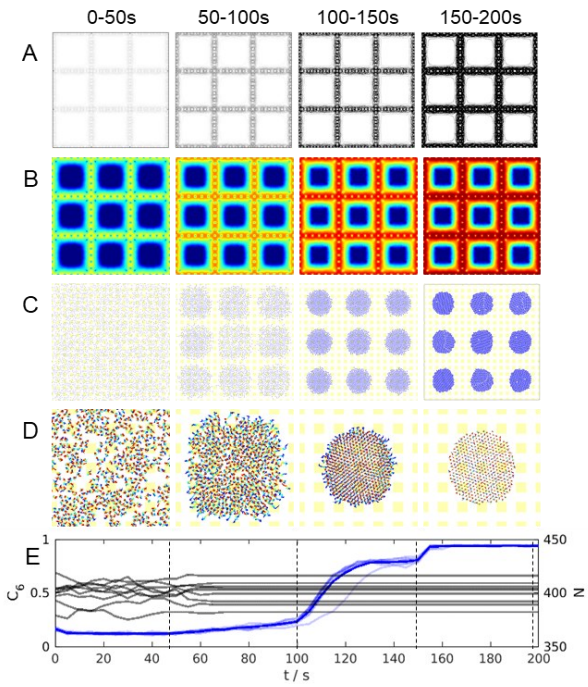

Figure 4-2 **Coarse partition particles into clusters.** (**A**) MHz AC electric fields for coarse partitioning with increasing strengths. The plots scale between 0 and 0.05 V/μm. The applied AC voltages are 0.06V, 0.2V, 1.6V and 2V (left to right). (**B**) Energy landscapes of single-particle interaction with AC electric fields (Eq. (4.8)). The plots scale between 0 and 100kT. (**C**) Equilibrium particle rendering under each field magnitude field. Particles are colored by average $\langle C_6 \rangle$ in white ($\langle C_6 \rangle$ = 0) to blue ($\langle C_6 \rangle$ = 1) scale. (**D**) Dynamic particle trajectories over 5s before reaching equilibrium states. The color bar ranges from blue to red following rainbow spectrum. (**E**) Parameters tracked during the coarse partitioning, including $\langle C_6 \rangle$ (blue) and cluster sizes (black). Dash lines correspond to capture times of (C).

Fig. 4-2 shows coarse partitioning of $N_0 = 3600$ particles (a = 1μm) into clusters with dimension of $L/S = 1/3$, which correspond to an array of 3×3 clusters. Fig. 4-2A shows four magnitudes of MHz AC electric fields sequentially applied during partitioning, and Fig. 4-2B shows corresponding energy landscapes due to interaction between particles and MHz AC electric field (Eq. (4.8)). Fig. 4-2C shows equilibrium distributions of particles under each field magnitude. Particles are colored by local C_6 values in white-to-blue scale, which represent the degree of local condensation. Fig. 4-2D shows dynamic trajectories of particles in the center cluster captured before reaching the equilibrium configurations over

five seconds. Trajectories are plotted in blue-to-red scale. Finally, Fig. 4-2E shows size (black) and averaged $\langle C_6 \rangle$ (blue) of individual clusters.

The applied MHz AC electric fields are designed to generate energy barriers of 0.1kT, 1kT, 10kT, and 100kT in four columns of Fig. 4-2. Coarse partitioning can be achieved by first separating particles into isolated clusters with these energy barriers, and then condensed into solid phase under field gradient. With small energy barriers less than kT, particles can diffuse freely across energy barriers and migrate between different clusters. As a result, the particles trajectories are stochastic, and cluster sizes are fluctuating. With intermediate energy barriers (<100kT), particles are constrained in each cluster, because kT-level thermo motion cannot overcome energy barriers. Meanwhile, particles aggregate within each cluster under field gradient towards cluster center. The equilibrium concentration and distribution of particles can be predicted by balancing the particle-field interaction with an osmotic pressure incurred by particle aggregation (see *supporting information*). At the high energy barrier (= 100kT), particles are completely condensed into solid phase, with averaged $\langle C_6 \rangle \approx 1$. The large energy barrier needed for full condensation is because of the nonlinear decay of field from cluster edge. Over the area of particles, the energy drops only by approximately 20kT, which can be proved by theory to be able to completely crystallize the given number of particles. Overall, Coarse partitioning achieved unequal sizes clusters with grain boundaries. To equalize cluster sizes, the cluster redistribution control is conducted and discussed next.

4.3.3 Redistribution of Particles to Form Equal Size Clusters

We use an example to demonstrate cluster redistribution in three steps (Fig. 4-3). The applied electric fields (Fig. 4-3A) and energy landscapes (Fig. 4-3B) used in each step are shown as linear summations of MHz AC fields and DC fields. Rendering of particles during each step of redistribution is colored to distinguish different clusters (Fig. 4-3C), and the direction of particle transfers are shown using dynamic trajectories captured over one second (Fig. 4-3D). Changes of cluster sizes are shown as a function of time with matching cluster colors (Fig. 4-3E).

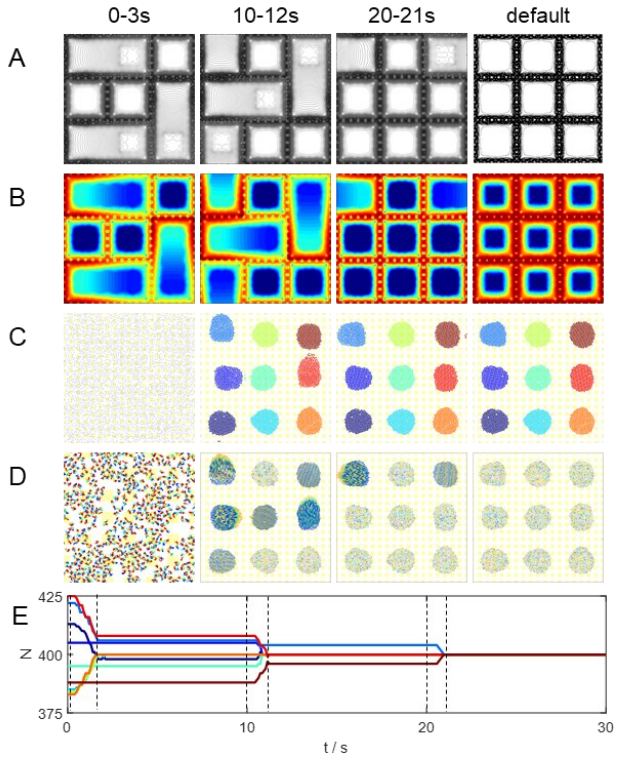

Figure 4-3 **Cluster redistribution.** (**A**) Applied electric fields during each step of redistribution control. The electric fields are superpositions of DC and AC electric fields and are plotted between 0 and 0.05V/μm. (**B**) Energy landscapes, which are linear summations of particle interactions with DC (Eq. (4.9)) and AC (Eq. (4.8)) electric fields. The plots scale between 0 and 100 kT. (**C**) Renderings of particle configurations in the middle of each redistribution step. Different colors are associated to each cluster. (**D**) Dynamic particle trajectories captured over 1s before rendered configurations. The color bar ranges from blue to red following rainbow spectrum. (**E**) Cluster sizes as a function of time with same colors. Dash lines correspond to capture times of (C).

Fig. 4-3 shows an example where all transfer operations are grouped into three steps, where each step consists of a single or multiple transfer operations. Equal size clusters are eventually held by AC electric field as in coarse partitioning. Because of the periodic boundary condition, transfers across simulation boundary are allowed. By the end of coarse partitioning, particles are randomly distributed in clusters, where the mean and standard deviation of cluster size can be predicted by density fluctuation theory based on isotherm compressibility factor.[140] It is practically impossible to directly achieve equal cluster size, and therefore cluster redistribution is necessary. A directional DC electric field can be used to move particles along field gradient,[141] and is used in this paper to transfer particles between adjacent clusters. An example of a single transfer operation is shown in Fig. 4-11. A MHz AC electric field is linearly superimposed onto the DC field, which constrains particles within the cluster pair and provides an energy barrier that shields the effect of DC field to nearby clusters. The two electric fields can be considered as results of an alternating voltage signal and a constant offset, respectively. The fields and energy landscapes can be linearly superimposed because their interaction with particles, given by Eq. (4.8) and (4.9), are independent with each other.

An optimal redistribution strategy (Fig. 4-12) is used with the goals to minimize total number of transferred particles and total number of transfer operations (Fig. 4-3). Details about the redistribution strategy is discussed later. Briefly, the strategy is found using a greedy algorithm based on the Manhattan distance between clusters. The strategy prefers transfers between closers clusters (*e.g.* adjacent) over clusters further apart (*e.g.* diagonal or alternating). The strategy also prefers a transfer path that can be combined with other transfers. To further accelerate cluster redistribution, multiple transfer operations can

be launched simultaneously by compartmenting the electrode array into individual cluster pairs, where each pair can be independently controlled (Fig. 4-3). For example, in the first plot of Fig. 4-3A and 4-3B, three redistribution cluster pairs are assigned (top-left, bottom-left, and bottom-right). In each cluster pair, the DC field establishes the field gradient that migrates particles from larger cluster to smaller cluster. In addition, the MHz AC field is applied to constrain the particles on the periphery. Numerically, the electric field and energy landscapes of each compartment are modeled separately, and the full profiles are concatenated by each compartment. This approach assumes a negligible effect of the field to one cluster pair to nearby clusters. This is valid due to the applied AC electric field, which generates a significant energy barrier that shields effect of DC fields outside of the controlled clusters. We presented a comparison between the approximated approach and the exact full modeling of all DC fields in Fig. 4-10. The results suggest that a negligible effect is caused due to crosstalk between different DC fields.

4.3.4 Remove Grain Boundaries in All Clusters

Fig. 4-4 shows the process of grain boundary removal control. The electric fields (Fig. 4-4A) and energy landscapes (Fig. 4-4B) are generated by periodic octupole electrodes. The resulting isotropic and anisotropic fields in perpendicular directions are alternatively applied with fixed period to compress clusters into different morphologies. Renderings of particles shows equilibrium morphology under each field shape (Fig. 4-4C), where grain boundary particles are colored in yellow, and other particles are colored in white-to-red scale by ψ_6 of each cluster. The dynamic particle trajectories (Fig. 4-4D) are captured over 5 seconds before reaching corresponding equilibrium configurations.

Trajectories are plotted in blue to red scale. The crystallinity and grain boundary orientation related to anisotropic field orientation are plotted for each individual cluster (Fig. 4-4E).

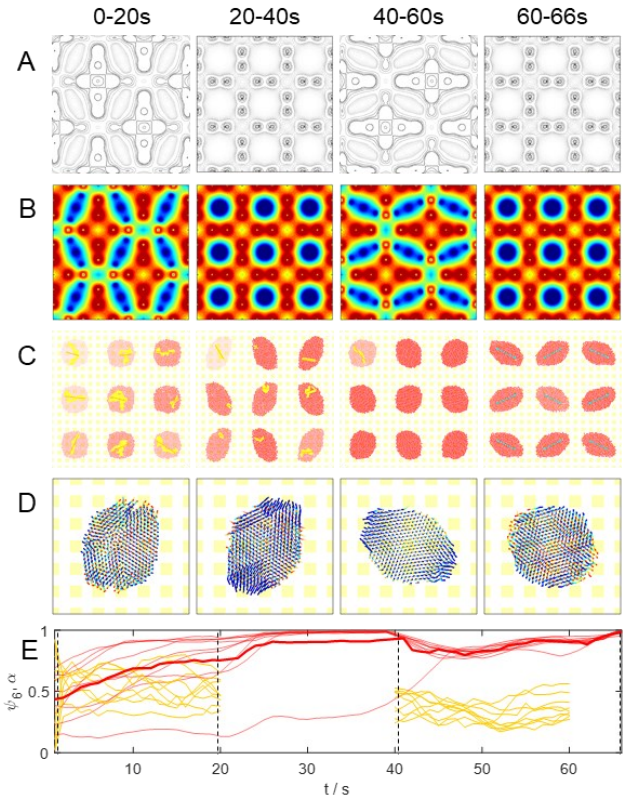

Figure 4-4 **Grain boundary removal using isotropic and anisotropic fields.** (**A**) MHz AC electric fields applied during each period of control. The plots scale between 0 and 0.05 V/μm. (**B**) Energy landscapes for single particle interaction with AC fields (Eq. (4.8)). The plots scale between 0 and 40kT. (**C**) Equilibrium particle configurations under each field shape. Grain boundary particles are colored in yellow and others are colored according to ψ_6 of each cluster in white (ψ_6 = 0) to red (ψ_6 = 1) scale. (**D**) Dynamic particles trajectories captured over 5s before rendered configurations. The color bar ranges from blue to red following rainbow spectrum. (**E**) Control parameters, including crystallinity ψ_6 (red) and grain orientation α (yellow) related to anisotropic field orientation for each cluster. Dash lines correspond to capture times of (C).

Removing grain boundaries within a single colloidal cluster using alternating isotropic and anisotropic electric fields has been reported in our previous paper. The goal in this work is to simultaneously achieve perfect crystallinity in all hierarchical crystals (ψ_6>0.99). By applying alternative field shapes and orientations, clusters are compressed in different shapes and directions, which not only changing the cluster morphology but also contributes to the diffusion of grain boundaries. Here an open loop control policy is

proposed. A fixed anisotropic field shape is used with two perpendicular orientations, which are generated by applying a voltage ratio of 10:5 to two pairs of active electrodes in octupole (Fig. 4-8A). Isotropic and anisotropic fields are alternatively applied with periods of 20s. During the first anisotropic period, a random field orientation is applied, while the following anisotropic periods always take perpendicular directions from the previous period. Isotropic field period is necessary because the dramatic energy difference between two perpendicular anisotropic fields can often destroy an existing ordered structure, while an isotropic intermediate step allows for moderate morphology changes while maintaining existing lattice structures. For example, in Fig. 4-4E, the first anisotropic period (t = [0,20s]) effectively removes grain boundaries in all but one clusters. During subsequent isotropic (t = [20,40s]) and anisotropic period (t = [40,60s]), the defected cluster continues to be improved, while the formed lattice structures are maintained with only local defects reintroduced. These defects can be easily removed by thermo motion of particles during subsequent control. Eventually, crystals are formed in all clusters. The negligible effect of morphing electric fields to existing crystal lattice is critical for the feasibility of assembly of hierarchical crystals. With other control approaches, for example, the assembly time could be orders of magnitudes longer or practically approaching infinity, even when such approaches are fairly efficient for a single cluster assembly control.

4.3.5 Obtain Circular Morphology and Perfect Crystals in All Clusters

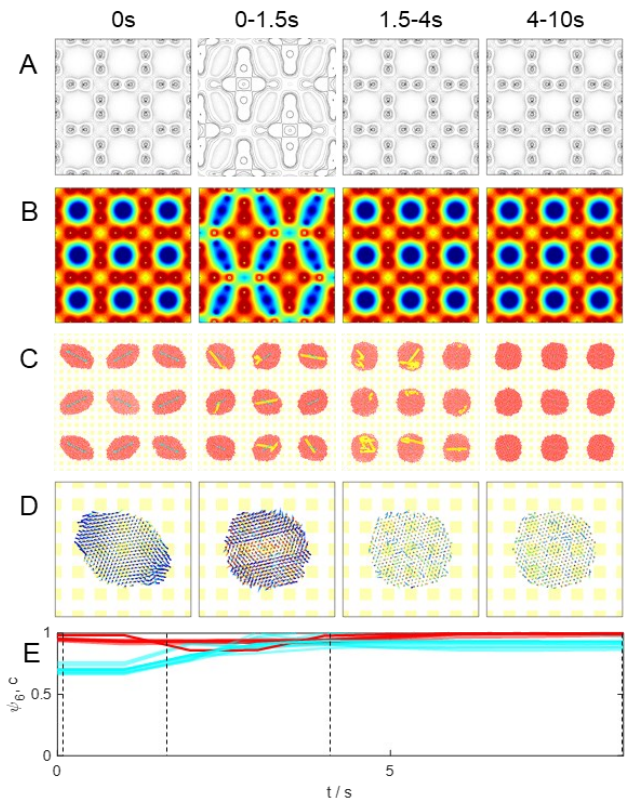

Figure 4-5 **Morphology relaxation using isotropic and anisotropic fields.** (**A**) MHz AC electric fields applied during each period of control. The plots scale between 0 and 0.05 V/μm. (**B**) Energy landscapes for single particle interaction with AC fields (Eq. (4.8)). The plots scale between 0 and 40kT. (**C**) Equilibrium particle configurations under each field shape. Grain boundary particles are colored in yellow and others are colored according to ψ_6 of each cluster in white (ψ_6 = 0) to red (ψ_6 = 1) scale. Cyan arrows point in the direction of morphology long-axis, and the length of arrows is $(1\text{-}c)\cdot R$, where c is the morphology circularity and $R = (N\cdot a^2/\eta_{cp})^{1/2}$ is the characteristic size of cluster. (**D**) Dynamic particles trajectories captured over 5s before rendered configurations. The color bar ranges from blue to red following rainbow spectrum. (**E**) Control parameters, including crystallinity ψ_6 (red) and morphology circularity c (cyan). Dash lines correspond to capture times of (C).

Fig. 4-5 shows a single step of control of cluster morphology to form perfect, circular crystals simultaneously in all clusters. Fig. 4-5A and B shows applied AC electric field and energy landscapes at different times of process. Fig. 4-5C shows renderings at these times. Grain particles are colored in yellow, and other particles are colored in white-to-red scale by $\psi_6$of each cluster. Cyan arrows represent morphology orientations of every

cluster, with length corresponding to deviation from circularity scaled by cluster radius. Fig. 4-5D shows particle trajectories over the course of one second starting from equilibrium positions in Fig. 4-5C. Fig. 5E shows trajectories of crystallinity, ψ_6, morphology circularity, c, and morphology orientation, θ, for each cluster.

After cluster redistribution (Fig. 4-3) and grain boundary removal (Fig. 4-4), all clusters are in perfect lattice structure, while morphology can be arbitrary depending on the ending state of previous control. Anisotropic field perpendicular to current morphology is applied to relax the circular morphologies, and isotropic field is applied to hold form circular crystals. Local defects and dislocations may be reintroduced during the process, as is seen in some clusters in Fig. 5C. However, these defects can be removed by particle thermo motions, and therefore melt automatically during the isotropic period. In a rare case, where reintroduced defect is nontrivial and cannot be removed with thermo motions, grain boundary removal control (Fig. 4-4) and morphology control (Fig. 4-5) can be re-applied in sequence. However, this has never happened over the course of 1000 simulations (Fig. 4-16). In all cases, a single iteration of grain boundary removal control and morphology restore control is required.

4.3.6 Potential Applications of Electrode Array

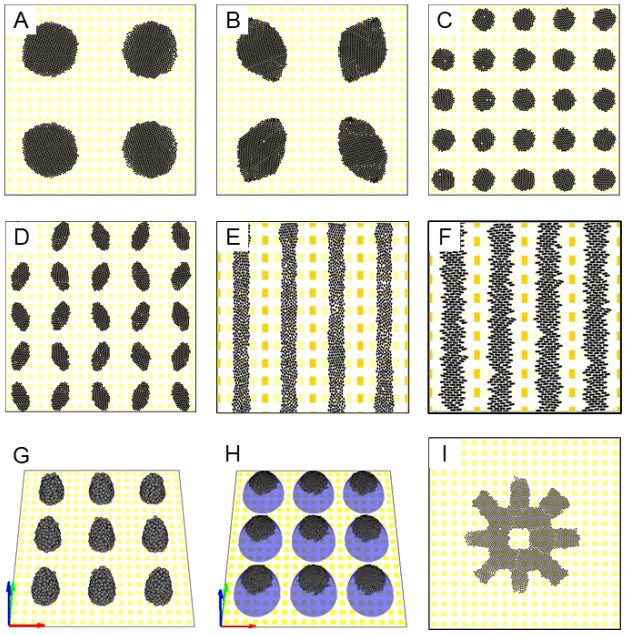

Figure 4-6 **Potential applications of electrode array.** (**A-D**) Assembly of hierarchical crystals with different sizes and morphology shapes. (**E**) Assembly of spherical particles into stripes by mimicking a parallel electrode. (**F**) Assembly of anisotropic particles into stripes. ((**G**) Assembly of hierarchical 3D colloidal structures. (**H**) Assembly of particles on periodic droplet interfaces. (**I**) assembly of complex microstructures, *e.g*. gears.

Fig. 4-6 presents a few potential applications based on electrode array. First, assembly and morphology control of various system and cluster sizes can be achieved by scaling the fields properly (Fig. 4-6A-D). Next, other microstructures (*e.g*. stripes) can be achieved using electrode array, which are used to assemble isotropic and anisotropic particles (Fig. 4-6E, F). Although the electrode array is a static pattern, the achievable energy landscapes are dynamic and reconfigurable. In this way, the limitation with pattern-based assembly can be overcome. Next, the assembly on periodic interfaces can also be facilitated by electrode array by simply depositing droplets only the substrates (Fig. 4-6G). Besides, the assembly can be extended from 2D structures to 3D, in which case periodic 3D pyramids can be assembly (Fig. 4-6H). Finally, electrode array can be used to achieved

more complex microstructures, such as a gear shape cluster (Fig. 4-6I). This can potentially be interesting in designing micromotors and achieve translation and rotation controls.

4.4 Conclusion

We reported a computational study of self-assembly of hierarchical colloid crystals from liquid phase using an electrode array. The process was divided into steps of coarse partitioning, cluster redistribution, and grain boundary and morphology control. Various types of DC and MHz AC electric fields were generated to facilitate different controls to colloid morphology and dynamics. We also investigated the scalability of problem for cluster redistribution and grain boundary and morphology control in terms of cluster dimension, L/S. Specifically, we presented an optimal redistribution strategy based on greedy planning algorithm and a Manhattan distance between clusters. We also presented an open loop strategy to direct the assembly of perfect, circular crystals.

The proposed strategy achieves accurate control to cluster size, crystallinity, and shape. The work is based on a simple design of electrode array, where each electrode can be individual activated with AC (alternating) and DC (offset) voltages. With the electrode array, we demonstrate control of colloidal phase behavior, nonequilibrium transport, and morphology and grain boundary defects. Based on this work, we further proposed a number of potential applications with electrode array. More cluster geometries can be formed using the electrode array, which can be used to study spherical as well as anisotropic particles. Moreover, electrode array can be used to control colloidal assembly on periodic droplet interfaces, or assembly of 3D microstructures. Finally, more complex structures, for example gears, can be obtained using an electrode array, which can be used to design micromotors.

4.5 Nomenclature

a	particle radius	R_g	individual cluster radius of gyration
a_c	morphology acylindricity	S	simulation window size
c	morphology circularity	S_x, S_y	gyration tensor diagonal terms
$\langle C_6 \rangle$	global bond connectivity	T	absolute temperature
$C_{6,i}$	local bond connectivity	u^{pf}	particle interaction with electric field
ε_m	medium dielectric constant	u_{ac}^{pf}	particle interaction with AC field
d	Manhattan norm	u_{dc}^{pf}	particle interaction with DC field
d_e	electrode size	u_i^{pp}	particle-particle interaction
D	medium viscosity	V_{dc}	DC field potential
e	elemental charge	α	relative GB orientation
E_{ac}	AC field magnitude	β	field orientation in lab coordinate
E_{dc}	DC field magnitude	γ	GB orientation in lab coordinate
f_{cm}	Clausius-Mossotti factor	ξ_p	particle zeta-potential
I	AC field second moment	ξ_s	substrate zeta-potential
k	Boltzmann constant	θ	relative morphology orientation
l	electrode distance	θ_{ij}	pair-wise particle orientation
L	cluster dimension	κ	inverse Debye screening length
N_0	total number of particles	$\langle N \rangle$	mean cluster size
ΔN	moved particle number	χ_6^{ij}	crystalline connectivity
N_i	size of cluster i	ψ_6	global bond orientational order
N_c^i	neighboring particle number	ψ_6^i	local bond orientational order
a	particle radius	Ψ	particle surface potential
r_{ij}	center-to-center particle distance		

4.6 Theory

4.6.1 Colloidal Interactions

The total energy, $u_{i,tot}$, acting on particle i under electric field is given by,

$$u_{i,tot} = \sum_{j \neq i} u_{ij}^{pp} + u_i^{ps} + u_i^{pf} \tag{4.1}$$

where the first term is the electrostatic repulsion between particle i and j and is given as,[59]

$$u_{ij}^{pp} = B \exp\left[-\kappa\left(r_{ij} - 2a\right)\right] \tag{4.2}$$

where,

$$B = 32\pi\varepsilon_m a\left(\frac{kT}{e}\right)^2 \tanh\left(\frac{e\Psi_p}{4kT}\right)\tanh\left(\frac{e\Psi_s}{4kT}\right) \tag{4.3}$$

where ε_m is the medium dielectric constant, a is the particle radius, k is the Boltzmann constant, T is the temperature, e is the elementary charge, r_{ij} is the center-to-center distance between the particles, Ψ_p is the colloid surface potential, and κ is the inverse Debye screening length. The second term in Eq. (4.1) represents interaction between particles and substrate, which is given by,

$$u_{ij}^{pp} = 2B\exp\left[-\kappa\left(z-a\right)\right] \tag{4.4}$$

where Ψ_s is surface potential of substrate. The last term in Eq. (4.1) represents interaction between a single particle and external fields, which are given as,

$$u^{pf}\left(x,y,z\right) = u^{grav}\left(z\right) + u_{ac}^{pf}\left(x,y\right) + u_{dc}^{pf}\left(x,y\right) \tag{4.5}$$

where (x, y, z) is the particle position in lab coordinate. u^{grav} is the energy caused by gravity, which is given by,

$$u^{grav}\left(z\right) = Gz \tag{4.6}$$

where,

$$G = \frac{3}{4}\pi a^3\left(\rho_p - \rho_m\right)g \tag{4.7}$$

where ρ_p and ρ_m are densities of particle and medium and g is the gravitational force. u_{ac}^{pf} is the energy due to interaction between particles and MHz AC electric field, which is given

by,[142]

$$u_{ac}^{pf}(x,y) = -2\pi\varepsilon_m a^3 f_{cm}\mathbf{E}_{ac}^2(x,y) \tag{4.8}$$

where, f_{cm} is the Clausius-Mossotti factor and $\mathbf{E}_{ac}$ is the AC electric field magnitude. u_{dc}^{pf} is the energy due to interaction with DC electric field, which is given by,[143]

$$u_{dc}^{pf}(x,y) = 4\pi a\varepsilon_m(\xi_p - \xi_s)V_{dc}(x,y) \tag{4.9}$$

where ξ_p and ξ_s are the zeta-potential of particle and substrate and V_{DC} is the local electric potential at the position of particles.

4.6.2 Equilibrium height of particles above substrate

For a single particle sediment under gravity, the total energy, $u_{i,tot}$, is given by,

$$u_{i,tot} = u_i^{ps} + u_i^{grav} \tag{4.10}$$

where the first term is the electrostatic repulsion between particle and substrate and the second term is gravity. The minimum in total energy occurs at equilibrium height given as,[144]

$$z_{eq} = \kappa^{-1}\ln\left(\frac{\kappa B}{G}\right) \tag{4.11}$$

where equilibrium height, z_{eq}, is found as ~100nm.

4.6.3 Electrophoretic potential under DC field

Eq. (4.9) is found by considering force balance of particle under DC electric field,

$$\mathbf{F}_{tot} = \mathbf{F}_{dc} + \mathbf{F}_{drag} \tag{4.12}$$

where $\mathbf{F}_{dc}$ is the electrophoretic force and $\mathbf{F}_{drag}$ is the stokes' friction given as,

$$\mathbf{F}_{drag} = -6\pi a\eta\mathbf{v} \tag{4.13}$$

where η is the medium viscosity, and $\mathbf{v}$ is the particle velocity, which can be related by electrophoretic mobility as,[143]

$$\mathbf{v} = \frac{\varepsilon_m\left(\xi_p - \xi_s\right)}{\eta}\mathbf{E}_{dc} \tag{4.14}$$

where $\mathbf{E}_{dc}$ is the local DC electric field magnitude. By substituting Eq. (4.14) and (4.13) into (4.12), one could get,

$$\mathbf{F}_{dc}\left(x,y\right) = 6\pi a\varepsilon_m\left(\xi_p - \xi_w\right)\mathbf{E}_{dc}\left(x,y\right) \tag{4.15}$$

which can be rewritten in scalar form in *x*- and *y*- coordinate as,

$$\begin{aligned} F_{dc,x} &= 6\pi a\varepsilon_m\left(\xi_p - \xi_w\right)E_{dc,x} \\ F_{dc,y} &= 6\pi a\varepsilon_m\left(\xi_p - \xi_w\right)E_{dc,y} \end{aligned} \tag{4.16}$$

The left-hand side can be integrated with respect to *x* and *y*, and sum to yield,

$$\int_{x_0}^{x} F_{dc,x}\partial x + \int_{y_0}^{y} F_{dc,y}\partial y = u_{dc}^{pf}\left(x_0, y_0\right) - u_{dc}^{pf}\left(x,y\right) \tag{4.17}$$

where x_0 and y_0 represent a reference state, and the right-hand side can yield,

$$6\pi a\varepsilon_m\left(\xi_p-\xi_w\right)\left[\int_{x_0}^{x}E_{dc,x}\partial x+\int_{y_0}^{y}E_{dc,y}\partial y\right]=6\pi a\varepsilon_m\left(\xi_p-\xi_w\right)\left[V_{dc}\left(x_0,y_0\right)-V_{dc}\left(x,y\right)\right] \tag{4.18}$$

Eq. (4.17) and (4.18) can be combined to yield,

$$u_{dc}^{pf}\left(x,y\right)=6\pi a\varepsilon_m\left(\xi_p-\xi_w\right)V_{dc}\left(x,y\right) \tag{4.19}$$

where the reference state is set to be zero for both electric potential and DC field energy landscape, and the expression is identical to Eq. (4.9).

4.6.4 Reaction Coordinates

4.6.4.1 Crystallinity Parameters

The global six-fold bond orientational order, ψ_6, is defined as,[97]

$$\psi_6=\left|\frac{1}{N}\sum_{i=1}^{N}\psi_6^i\right| \tag{4.20}$$

where N is the total number of particles, and ψ_6^{i} is the local six-fold bond orientational order for each particle i, given by,

$$\psi_6^i=\frac{1}{N_c^i}\sum_{j=1}^{N_C^i}e^{i6\theta_{ij}} \tag{4.21}$$

where $N_{\mathrm{c}}^{\mathrm{i}}$ is the number of coordinated neighbors within the first coordination radium of particle i, and θ_{ij} is the angled between particle i and j and the lab coordinate given as,

$$\theta_{ij} = \tan^{-1}\left(\frac{y_i - y_j}{x_i - x_j}\right) \tag{4.22}$$

The crystalline connectivity, χ_6^{ij}, between particle *i* and *j* is defined as,

$$\chi_6^{ij} = \frac{\left|\mathrm{Re}\left[\psi_6^i \psi_6^{j*}\right]\right|}{\left|\psi_6^i \psi_6^{j*}\right|} \tag{4.23}$$

where ψ_6^{j*} is the complex conjugate of ψ_6^j. The local six-fold connectivity $C_{6,i}$ can be calculated by,[98]

$$C_{6,i} = \frac{1}{6}\sum_{j=1}^{N_c^i}\left[\begin{vmatrix} 1 & \chi_6^{ij} \geq 0.32 \\ 0 & \chi_6^{ij} < 0.32 \end{vmatrix}\right] \tag{4.24}$$

and the global six-fold connectivity, $\langle C_6 \rangle$, is given by,

$$\langle C_6 \rangle = \frac{1}{N}\sum_{i=1}^{N} C_{6,i} \tag{4.25}$$

4.6.4.2 Electric Field Orientation

The orientation of MHz AC electric field is derived from the second moment of field energy landscape, defined in Eq. (2.2), as,

$$I = \frac{1}{\iint u^{pf}(x,y)\,dxdy}\begin{bmatrix} \iint x^2 u^{pf}(x,y)\,dxdy & \iint xy \cdot u^{pf}(x,y)\,dxdy \\ \iint xy \cdot u^{pf}(x,y)\,dxdy & \iint u^2 u^{pf}(x,y)\,dxdy \end{bmatrix} \tag{4.26}$$

where the coordinate (x, y) is defined in a lab coordinate. Field orientation is defined from a rotation matrix given as,

$$\begin{bmatrix} x' \\ y' \end{bmatrix} = \begin{bmatrix} \cos\beta & -\sin\beta \\ \sin\beta & \cos\beta \end{bmatrix} \begin{bmatrix} x \\ y \end{bmatrix} \tag{4.27}$$

where β is the field orientation when Eq. (3.30) is diagonalized with respect to rotated coordinate (x', y') as,

$$I' = \frac{1}{\iint u^{pf}(x', y') \cdot dxdy} \begin{bmatrix} \iint (x')^2 u^{pf}(x', y') \cdot dxdy & 0 \\ 0 & \iint (y')^2 u^{pf}(x', y') \cdot dxdy \end{bmatrix} \tag{4.28}$$

4.6.4.3 Morphology Parameters

Particle morphology shape and orientation are derived from particle gyration tensor, which is given as,[88]

$$S = \frac{1}{N} \begin{bmatrix} \sum_i x_i^2 & \sum_i x_i y_i \\ \sum_i x_i y_i & \sum_i y_i^2 \end{bmatrix} \tag{4.29}$$

Where, similar to Eq. (3.30), the coordinates are based on a lab coordinate. Morphology orientation is defined in,

$$\begin{bmatrix} x_i' \\ y_i' \end{bmatrix} = \begin{bmatrix} \cos\varphi & -\sin\varphi \\ \sin\varphi & \cos\varphi \end{bmatrix} \begin{bmatrix} x_i \\ y_i \end{bmatrix} \tag{4.30}$$

where φ is absolute morphology orientation if Eq. (3.42) can be diagonalized with respect to rotated coordinate as,

$$S' = \frac{1}{N}\begin{bmatrix} \sum_i (x_i')^2 & \sum_i x_i' y_i' \\ \sum_i x_i' y_i' & \sum_i (y_i')^2 \end{bmatrix} = \begin{bmatrix} S_x & 0 \\ 0 & S_y \end{bmatrix} \tag{4.31}$$

where S_x and S_y are primary diagonal terms. The final morphology orientation is defined with respect the applied field orientation as,

$$\theta = \frac{|\varphi - \beta|}{90°} \tag{4.32}$$

The morphology shape (circularity) is defined as,

$$c = 1 - \left(a_c / R_g\right) \tag{4.33}$$

where R_g is the particle radius of gyration,

$$R_g = \sqrt{S_x + S_y} \tag{4.34}$$

and a_c is the morphology acylindricity,

$$a_c = \sqrt{S_x - S_y} \tag{4.35}$$

4.6.4.4 Grain Boundary Coordinate

Grain particles are interior particles that are not hexagonally packed. Mathematically they are identified as $\psi_{6,i}<0.9$ and $C_{6,i}>0.6$. The orientation of grain boundary is defined as,

$$\gamma = \arctan\left[\frac{\sum_i \left(x_{i,g} - \langle x_g \rangle\right)\left(y_{i,g} - \langle y_g \rangle\right)}{\sum_i \left(x_{i,g} - \langle x_g \rangle\right)^2}\right] \tag{4.36}$$

where x_g and y_g are coordinates of grain particles, and angle brackets values represent center of mass coordinate. Conceptually γ is equivalent to the slope of a linear fit for all grain particles. The final grain boundary orientation is defined with respect to field orientation as,

$$\alpha = \frac{|\gamma - \beta|}{90°} \tag{4.37}$$

4.6.5 Colloidal Phase Behavior on Energy Landscapes

In our previous work we have shown the general relationship between particle density distribution and the applying external field.[84] The two-dimensional osmotic pressure, $\Pi(\rho)$, for hard disk colloids is given by the equation of state as,[44]

$$\Pi(\rho) = kT\rho Z(\rho) \tag{4.38}$$

where ρ is the particle number density and Z is the compressibility factor. For hard disk model, the compressibility factor is given as,

$$\begin{aligned} Z_{HD,\mathrm{F}}\left(\eta_{eff}\right) &= \left(1 + \frac{\eta_{eff}^2}{8}\right)\left(1 - \eta_{eff}\right)^{-2} && \eta_{eff} < \eta_f \\ Z_{HD,\mathrm{S}}\left(\eta_{eff}\right) &= 2\left(\frac{\eta_{CP}}{\eta_{eff}} - 1\right)^{-1} + 0.67\left(\frac{\eta_{CP}}{\eta_{eff}} - 1\right) + 1.9 && \eta_{CP} > \eta_{eff} > \eta_m \end{aligned} \tag{4.39}$$

where $Z_{\mathrm{HD,F}}$ is the fluid compressibility factor valid from infinite dilution up to the freezing

transition, η_f=0.69, and $Z_{HD,S}$ is the solid compressibility factor valid from melting transition, η_m=0.71, up to close packing at η_{CP}=0.906. η_{eff} is effective area fraction given as,

$$\eta_{eff} = \pi a_{eff}^2 \rho \tag{4.40}$$

where a_{eff} is the effective radius of particles which accommodates the pair-wise electrostatic repulsion interaction and is given as,[10]

$$2a_{eff} = 2a + \int_{2a}^{\infty} \left[1 - \exp\left(-u^e\left(r\right) / kT \right) \right] dr \tag{4.41}$$

Eq. (2.6) can be rewritten by combining Eq. (3.12)-(3.14) as,

$$\Pi\left(\eta_{eff}\right) = kT \frac{\eta_{eff}}{\pi a_{eff}^2} Z_{HD}\left(\eta_{eff}\right) \tag{4.42}$$

which relates the colloidal osmotic pressure to the effective area fraction. Under a 2D external energy landscape, differential changes in local osmotic pressure are given by partial differential force balances as,

$$\frac{\partial \Pi\left(x,y\right)}{\partial x} = -\frac{\partial u^{pf}\left(x,y\right)}{\partial x} \cdot \rho\left(x,y\right), \quad \frac{\partial \Pi\left(x,y\right)}{\partial y} = -\frac{\partial u^{pf}\left(x,y\right)}{\partial y} \cdot \rho\left(x,y\right) \tag{4.43}$$

which can be integrated with respect to x and y, and add together to give,

$$\int \frac{\partial \Pi\left(x,y\right)}{\partial x} \cdot dx + \int \frac{\partial \Pi\left(x,y\right)}{\partial y} \cdot dy = -\int \rho\left(x,y\right) \frac{\partial u^{pf}\left(x,y\right)}{\partial x} \cdot dx - \int \rho\left(x,y\right) \frac{\partial u^{pf}\left(x,y\right)}{\partial y} \cdot dy \tag{4.44}$$

which, by chain rule of total derivatives, can be simplified as,

$$\int d\Pi(x,y) = -\int \rho(x,y)\cdot du^{pf}(x,y) \tag{4.45}$$

which indicates that 2D differential changes in local osmotic pressure can be related to differential changes in the local energy landscape and the local density. Inserting the equation of state given by Eq. (2.10) into Eq. (2.16) and re-arranging gives,[84]

$$\int_{\eta_0}^{\eta_{eff}(x,y)} \frac{1}{\eta} d\left(\eta \cdot Z_{HD}\right) = -\frac{1}{kT}\left(u^{pf}(x,y) - u_0^{pf}\right) \tag{4.46}$$

where the left-hand side is integrated from a reference density, η_0, to the density at position (x, y), $\eta(x, y)$, and the right-hand side is integrated from the reference energy, $u^{pf}{}_0$, to the same energy landscape position, $u^{pf}(x, y)$. Eq. (4.46) indicates particle density depends only on energy landscape magnitude, and therefore the field can be related to the particle phase behavior. With Eq. (4.46), one can theoretically calculate minimum field strength to crystallize a given number of particles in a specific electric field. Briefly, The crystallization voltage of N particles under a specific field shape can be solved based on a 90-10 rule,[96] where the density decays from 90% of the maximum density to 10% in less than one particle diameter at the periphery. Using this criterion, Eq. (4.46) is re-written as,

$$\int_{0.1\eta_{cp}}^{0.9\eta_{cp}} \frac{1}{\eta} d\left(\eta \cdot Z_{HD}\right) = -\frac{1}{kT}\left[u^{pf}(R-a) - u^{pf}(R)\right] \tag{4.47}$$

where R is the distance between cluster edge and center. u^{pf} is replaced by Eq. (4.8) to yield,

$$\mathbf{E}^2\left(R-a\right)-\mathbf{E}^2\left(R\right)=\frac{kTZ_{HD}\ln 9}{2\pi a^3\varepsilon f_{cm}} \tag{4.48}$$

Which can be approximated as,

$$\nabla\mathbf{E}^2\left(R\right)=\frac{kTZ_{HD}\ln 9}{4\pi a^4\varepsilon f_{cm}} \tag{4.49}$$

Eq. (3.22) provide the minimum magnitude of the gradient of squared electric field on cluster edge in order to obtain a crystal phase.

4.6.6 Distribution of Cluster Size Based on Fluctuation Theory

Distribution of cluster sizes by coarse partitioning can be considered as a density fluctuation problem. The number of particles in each cluster can be considered as the particle density of each cluster area, and is given as,[140]

$$\frac{\sigma_N^2}{\langle N\rangle}\frac{1}{\rho k_B T}=\chi_T^L=(1-\frac{L^2}{S^2})\chi_T+\chi_T^{(b)}L^{-1}+O(L^{-2}) \tag{4.50}$$

whereρ is the fluid density, $\langle N\rangle$ and σ_N^2 are the mean and variance of particle number in the, L and S are dimensions of the area and the whole system, χ_T is the isothermal compressibility, χ_r^L is the expanded expression of isothermal compressibility in finite area, and $\chi_T^{(b)}$ is the first order correction due to boundaries of the block. Isothermal compressibility or pair distribution function can be calculated by,[145]

$$\rho kT\chi_T=\left\{\frac{\partial}{\partial\phi}\left[\phi Z(\phi)\right]\right\}^{-1} \tag{4.51}$$

The compressibility factor, $Z(\phi)$, can be approximated by Henderson's compressibility factor for a hard disk system as[146-147]:

$$Z(\phi) = \frac{1+0.125\phi^2}{(1-\phi)^2} \tag{4.52}$$

$\chi_T^{(b)}$ can be approximated as,

$$\chi_T^{(b)} = L\left[\frac{1-L^2/S^2}{\rho k_B T} - (1-\frac{L^2}{S^2})\chi_T\right] \tag{4.53}$$

which can be substituted in Eq. (4.50) to yield,

$$\frac{\sigma_N^2}{\langle N\rangle} = 1-\frac{L^2}{S^2} \tag{4.54}$$

which relates the variance of cluster size with cluster dimension. The mean cluster size, $\langle N\rangle$, is given by,

$$\langle N\rangle = \frac{L^2}{S^2} N_0 \tag{4.55}$$

where N_0 is the total number of particles in the system.

4.7 Computational Methods

4.7.1 Brownian Dynamics Simulation

Brownian Dynamics simulations used in this paper to study hierarchical assemble of particles were described in previous papers.[38, 148] Particles were confined in a 2D plane, whose trajectories were based on Langevin equation as,[149]

$$m\frac{d\mathbf{v}}{dt} = \mathbf{F}^H + \mathbf{F}^P + \mathbf{F}^B \tag{4.56}$$

where m is the particle relative mass in water, $\mathbf{v}$ is the particle velocity, and $\mathbf{F}^{\mathrm{H}}$ is the hydrodynamic forces, $\mathbf{F}^{\mathrm{P}}$ is the conservative forces due to particle interactions, and $\mathbf{F}^{\mathrm{B}}$ is the stochastic Brownian force. $\mathbf{F}^{\mathrm{P}}$ is given by the negative derivative of particle interactions defined in Eq. (2.1). $\mathbf{F}^{\mathrm{H}}$ is related to particle velocity and diffusivity as,

$$\mathbf{F}^H = -\frac{kT}{D}\mathbf{v} \tag{4.57}$$

where D is the particle diffusivity above a no-slip plane.[148, 150] $\mathbf{F}^{\mathrm{B}}$ is defined by,[151]

$$\begin{aligned} \left\langle \mathbf{F}^B \right\rangle &= 0 \\ \left\langle \mathbf{F}^B(0)\mathbf{F}^B(t) \right\rangle &= 2(kT)^2 D^{-1}\delta(t) \end{aligned} \tag{4.58}$$

Table 4-1 **Brownian Dynamic simulation parameters**. (a) Particle radii, (b) medium dielectric constant, (c) Debye length, (d) Clausius-Mossotti factor, (e) particle zeta potential, (f) substrate zeta potential, (g) temperate, (h) particle density, (i) medium density, (j) gravity constant.

Parameter	equation	value	parameter	equation	value
a (nm)[a]	(4.2), (4.3)	1000	ψ_s (mV)[f]	(4.2)	-50
ε_m[b]	(4.6), (4.7)	78	T (K)[g]	(4.2)	300
κ^{-1} (nm)[c]	(4.7)	10	ρ_p (g/cm^3)[h]	(4.8)	1.96
f_{cm}[d]	(4.6)	-0.47	ρ_m (g/cm^3)[i]	(4.8)	1
ψ_p (mV)[e]	(4.2)	-50	g (m/s^2)[j]	(4.8)	9.8

Particles diffuse in a quasi-2D plane above the substrate with fixed height of ~100nm (Eq. (4.11)). The equilibrium height is calculated by considering particle gravity and interaction between single particle and bottom substrate. Effects of electric fields to equilibrium height is neglected in the simulation. Other parameters used in the simulation are summarized in Table 1. Simulations were performed with an integration time of 0.01ms and store interval of 0.1s. Periodic boundary conditions were applied for the simulation

cell, which contained 3600 particles corresponding to a volume fraction of $\phi = 0.3$.

4.7.2 Electric Field Modeling

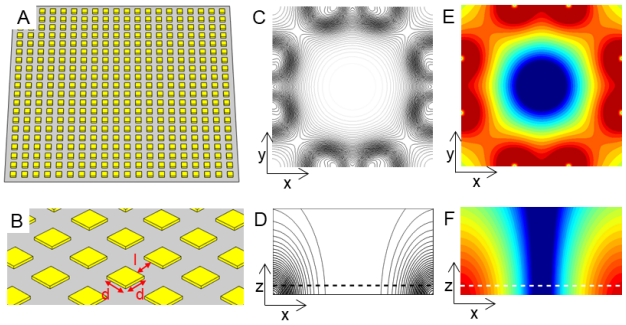

Figure 4-7 **COMSOL model of electrode and electric field.** (A) array of 20 by 20 electrodes (yellow) modeled on bottom substrate (gray). (B) Zoomed-in view. Electrode has dimension of 5μm (W) by 5μm (L) by 40nm (H), and are separated by *l* = 5μm in orthogonal array. (C) top view of a sample electric field generated by activating 8 electrodes with AC voltage and used to direct assembly. The colorbar ranges between 0 and 0.05V//μm. (D) xz-plane of the same electric field. Dash line shows the equilibrium height of particles, which is also the plane of lookup table. (E) Top view of energy landscape of single particle interacting with electric field shown in (C). Color bar ranges between 0 and 40kT. (F) xz-plane of the same energy landscape plotted up to 15 μm from bottom substrate.

DC electric fields and time-averaged MHz AC electric fields are modeled using electrostatic interface of COMSOL Multiphysics. Gold electrodes are placed on the bottom substrate, where each electrode has dimensions of 5μm (L) × 5μm (W) × 40nm (H). To form electrode array, electrodes are separated by 5μm into a regular matrix of 20 rows and 20 columns (Fig. 4-7). The whole model box has dimensions of 400μm (L) × 400μm (W) × 20 μm (H). To generate different electric fields, a subset of electrodes is activated with specified voltages, while others remain idle. COMSOL results suggest that inactivated electrodes do not distort the generated field shape. Electric fields are tabulated on the plane 1.5 μm above the bottom substrate, which is equivalent to the equilibrium height of particles electrostatically stabilized into quasi-2D structure. Electric fields have a spatial resolution of 0.25μm. Finer values are calculated using Barycentric interpolation

in simulation.

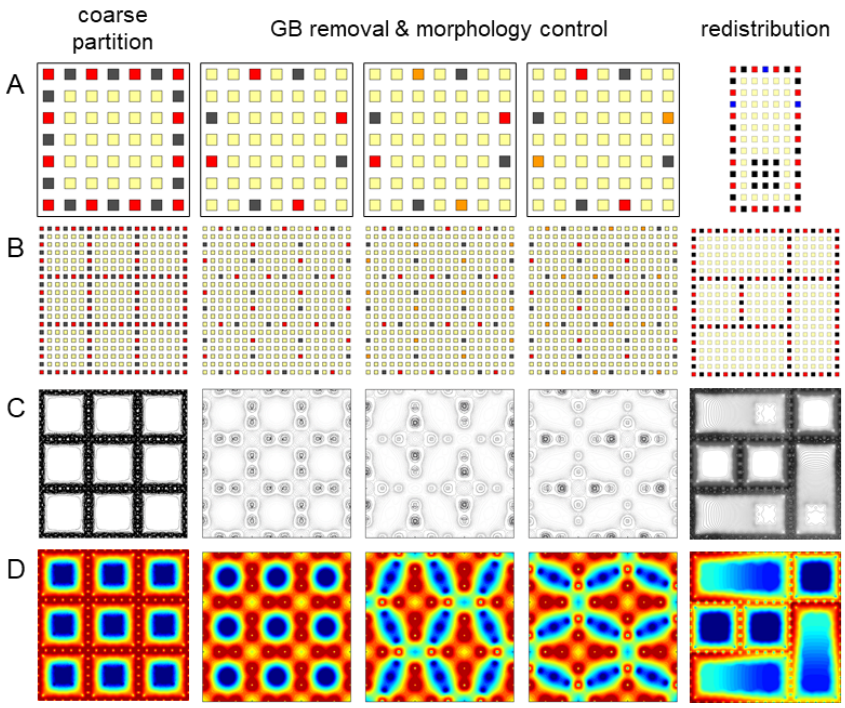

Figure 4-8 **Electrode conditions, electric fields, and energy landscapes.** (**A**) Electrode conditions of single control cell for coarse partition (1st column), GB and morphology control, including octupole with equal (2nd column) and unequal voltages (3rd and 4th column), and cluster redistribution (5th column). Electrodes are applied with AC voltage (red), DC voltage(blue), ground (black), or inactive (yellow). (**B**) Corresponding electrode conditions of the whole array. (**C**) Contour plots of electric field magnitudes generated by electrode conditions. The plots scale between 0 and 0.05V/μm for both AC and DC fields. (D) Energy landscapes of single particle interaction with applied AC and DC electric fields. The plots scale between 0 and 100kT for the 1st and 5th columns, and between 0 and 40kT for the other columns. Superposition and approximation of DC electric fields

DC electric fields are used during cluster redistribution. AC and DC electric fields are separately modeled using COMSOL, which assumes their energy landscapes, given by Eq. (2.2) and (4.9), are independent with each other. Moreover, the DC energy landscape is assumed to be effective only within the clusters that undergo redistribution and does not affect particles in surrounding clusters. This is expected to be reasonable because all clusters are always framed by AC electric fields, which provides a strong energy barrier (>100kT) between clusters and constrain particles towards cluster centers.

In addition, when multiple pairs of clusters undergo redistribution, the DC energy landscapes are independent with each other and are linearly superimposed with each other and with the AC energy landscape. This is valid by assuming DC energy landscape is confined within the redistributed clusters. Later we compare this approximation with a complete modeling of all existing DC electric fields.

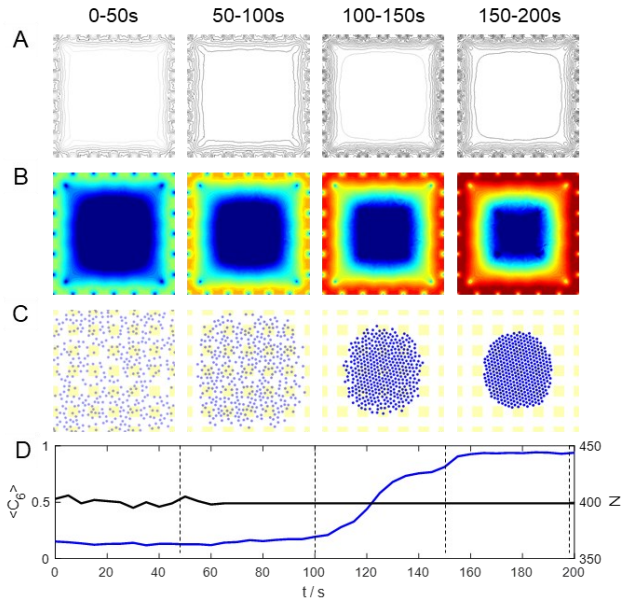

Figure 4-9 **Coarse partition in a single control cell.** (**A**) MHz AC electric fields generated using the electrodes shown in Fig. 4-7A, 1st column, with increasing voltages set as 0.06V (0-50s), 0.2V (50-100s), 1.6V (100-150s) and 2V (150-200s). The plots scale between 0 and 0.05 V/μm. (**B**) Energy landscapes for single-particle interaction with AC electric field (Eq. (4.8)), which scale between 0 and 100kT. (**C**) Particles in equilibrium under each field magnitude. Particles are colored in white (<C_6> = 0) to blue (<C_6> = 1) scale. (**D**) Trajectories of <C_6> (blue) and particle number within the cell area. Equilibrium particle configurations are captured at instances represented by dash lines.

4.8 Coarse Partitioning

4.8.1 Electric field

Electric fields (Fig. 4-9B 1st column) used for coarse partitioning are generated by alternatively applying a constant MHz AC voltage and ground state to adjacent electrodes on cluster edges (Fig. 4-9A 1st column). Such array of electrodes form boundaries that

divide electrode array into cluster regions. Each cluster region has a dimension of L = 60μm. The energy barrier on cluster edges is determined by applied voltage.

4.8.2 Energy landscape

Magnitude and distribution of particle-field energy landscape is defined by Eq. (2.2), with electric described in previous section (Fig. 4-9C 1st column).

4.8.3 Equilibrium microstructure

Particles are constrained and condensed by AC electric field and energy landscape into isolated clusters. Degree of condensation is determined by magnitude of applied field. At low magnitudes, energy barrier does not prevent particles from diffusing between adjacent cluster. At intermediate magnitudes, energy barrier is significantly high such that particles are constrained within specific cluster regions. At high field magnitudes, energy barrier not only constrains particles into isolated areas, but also condensed them into crystals because of long-range decay of energy landscape from cluster edges.

4.8.4 Control policy

A step ramp of field is used to divide particles into separate clusters and condense clusters to crystal phases. The magnitude of each step is designed to create energy barriers between cluster areas on orders of $0.1kT$, $1kT$, $10kT$ and $100kT$.

Table 4-2 Coarse partition control strategy

iterate with period Δt = 50s, increment applied voltage
V_{AC} = 0.06V if t < 50s
V_{AC} = 0.2V if 50s < t < 100s
V_{AC} = 1.6V if 100s < t < 150s
V_{AC} = 2V if 150s < t < 200s

4.9 Particle Redistribution

4.9.1 Electric field

A DC electric field is applied to direct the transfer of particles, and an AC electric field is applied to constrain the particles (Fig. 4-8B 5th column). DC and AC electric fields are modeled separately using COMSOL and then linearly sum together. This is reasonable because AC and DC electric fields come from a time-alternating voltage and a constant offset. Moreover, the interaction between particles and each type of field, as given in Eq. (2.2) and (4.9), are independent with each other. DC electric field is oriented such that active electrodes are around the cluster with larger size, and 9 ground electrodes are placed at the center of the cluster with smaller size (Fig. 4-8A 5th column). Particles migrate along generated field gradient as defined by Eq. (4.9). AC electric field is used to hold particles in two clusters and prevent the DC field from affecting surrounding clusters. As a result, when multiple DC fields are applied to simultaneously direct transfers between different pairs of clusters, the overall DC field is a linear summation of each individual part. When transfer operation is completed, AC electric fields same as used in coarse partitioning are applied to split the redistributed clusters and hold particles back cluster centers (Fig. 4-8B 1st column).

4.9.2 Energy landscape

Energy landscapes caused by AC and DC electric fields are computed separately by Eq. (4.8) and (4.9). The final energy landscape is assumed to be a linear summation of the two components (Fig. 4-8C 5th column). Moreover, when multiple DC electric fields are applied simultaneously, they are considered to be independent with each other. Fig. 4-10 compares COMSOL simulations between a complete calculation of all DC fields and a

linear summation of individually calculated fields. To approximate the periodic boundary condition, the electrode array is repeated by 9 times into a matrix of 3×3 (Fig. 4-10A). The AC electric field applied on a single electrode array is shown in Fig. 4-10B, which is similar to the coarse partitioning field except that the barrier between transferred clusters are removed. The resulting energy landscape has local energy minima in each separated cluster (Fig. 4-10C). The DC electric field is modeled by replicating the array for 9 times (Fig. 4-10D), where all three sets of DC fields are modeled in each array (Fig. 4-10E). The calculated energy landscape is therefore an exact solution (Fig. 4-10F). By superimposing both components, the final energy landscape is shown in Fig. 4-10I. For every pairs of redistributed clusters, an energy gradient exists due to DC fields. For other unaffected clusters, energy landscape drops from cluster edge to center, which constrain particles in each cluster. On the other side, the overall energy landscape can be obtained approximated by superimposing AC field (Fig. 4-10C) with multiple sets of single DC field (Fig. 4-10H). The resulting field is given in Fig. 4-10J, which is very close to the complete model given in Fig. 4-10I. The major difference is the energy profile of the cluster on the leftmost of second row, which are slightly affected the surrounding DC fields. However, this is negligible considering the overall energy barrier that holds this cluster is ~100kT.

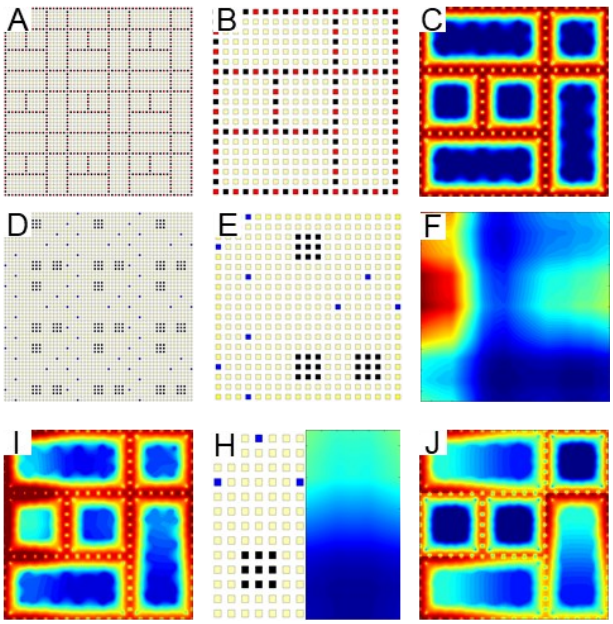

Figure 4-10 **Comparison between approximated and exact solutions of superimposed energy landscapes.** (**A**) Full COMSOL simulation model for the AC electric field, where the periodic boundary condition is approximated by replicating the original electrode array by 8 times. (**B**) Electrode design in COMSOL of the original simulated electrode array. Red and black electrodes represent active AC and ground electrodes. (**C**) COMSOL modeling of the energy landscape due to particle interaction with AC electric field. The plot scales between 0 and 100 kT. (**D**) Full COMSOL simulation model for the DC electric field, where the periodic boundary condition is approximated by replicating the original electrode array by 8 times. (**E**) Electrode design in COMSOL of the original simulated electrode array. Blue and black electrodes represent active DC and ground electrodes. (**F**) COMSOL modeling of the energy landscape due to particle interaction with DC electric field. The plot scales between 0 and 20 kT. (**I**) Linear summation of energy landscapes in (C) and (F), which is assumed to be the exact solution for particle interactions under AC and DC fields. The plot scales between 0 and 100 kT. (**H**) COMSOL model of a single set of DC electric field (left) and its corresponding energy landscape (right) scaled between 0 and 100kT. (**J**) Approximated energy landscape, in which the single DC energy landscape shown in (H) is superimposed to corresponding cluster regions in (C).

4.9.3 Equilibrium microstructure

At equilibrium states, all clusters are held by AC field and energy landscape. During cluster redistribution, DC fields are applied to certain pairs of adjacent clusters, between which a specific number of particles are moved. Once target number of particles are moved to the other cluster, DC field is turned off and AC fields are reapplied to equilibrate particles into respective clusters. The process repeats until all clusters have same sizes.

4.9.4 Control policy

4.9.4.1 Control Policy for Pair-wise Cluster Redistribution

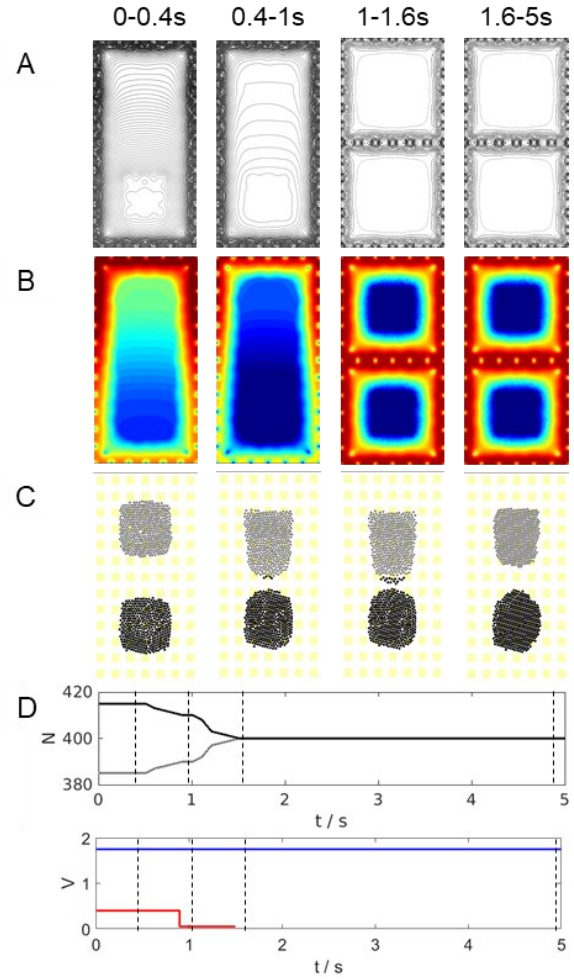

Figure 4-11 **Transfer operation between two adjacent clusters.** (**A**) Applied electric fields, where the first two columns are linear superpositions of DC and MHz Ac electric fields, and the last two columns are MHz AC electric fields. The plots scale between 0 and 0.05 V/μm. (**B**) Energy landscapes, where the first two columns are linear summation of interactions between particles and DC (Eq. (4.9)) and MHz AC (Eq. (4.8)) electric fields, and the last two columns are based on interaction with MHz AC electric fields only. The plots scale between 0 and 100kT (**C**) Particle renderings captured throughout the redistribution process, where black and grey particles represent the two clusters. (**D**) Cluster sizes (black and gray) and applied DC (red) and AC (blue) voltages. Dash lines correspond to capture times of (C).

Control policy is designed at two levels. At the low level, particle redistributed from the controlled cluster to an adjacent cluster is achieved using direction DC electric field and AC electric field (Fig. 4-11). Applied voltages are given by,

$$V_{DC} = \begin{cases} 0.4V & N = N_0 \\ 0.1V & N_0 > N > N - \Delta N \\ 0V & N = N - \Delta N \end{cases} \tag{4.59}$$

where N is the number of particles in the controlled cluster, N_0 is the initial number of particles in the controlled cluster. ΔN is the number of particles to be moved. All clusters are initially held with AC fields. when ΔN particles need to be transferred between two clusters, the DC field is applied at maximum magnitude to propel particles in the controlled cluster towards the other cluster (Fig. 4-11 1st column). As soon as the first particle exceeds cluster boundary, a reduced DC field is applied to fine control transport process (Fig. 4-11 2nd column). When the target cluster size is reached, the DC field is turned off and AC field is re-applied (Fig. 4-11 3rd column). Particles in both clusters eventually reach equilibrium positions again (Fig. 4-11 4th column).

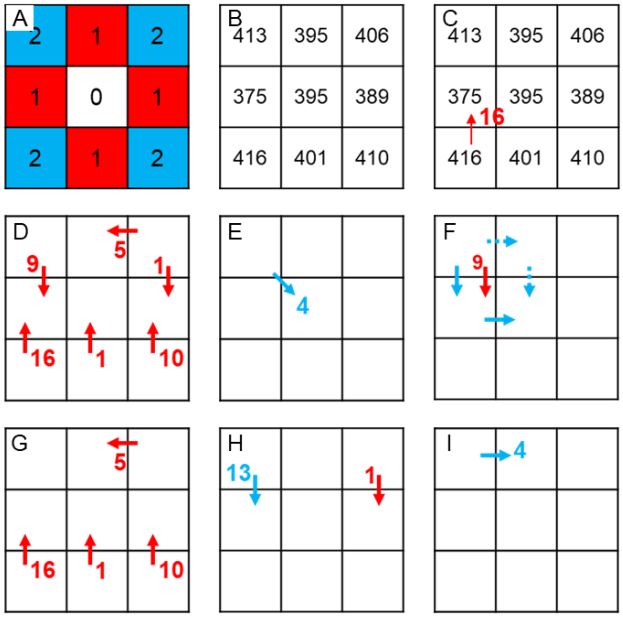

Figure 4-12 **Optimal cluster redistribution strategy.** (**A**) Manhattan norm (distance) between clusters with respect to the center in a *L*/*S* = 1/3 array. (**B**) A sample distribution of N_0 = 3600 particles formed by coarse partitioning. (**C**) A transfer operation between the most inequal clusters adjacent to each other (*d* = 1), which is the most preferred operation according to the greedy planning algorithm. (**D**) A summary of all transfers between adjacent clusters (*d* = 1). (**E**) An

operation between diagonal clusters (d = 2), which is needed in order to equalize clusters as shown in (B). (**F**) two potential transfer paths (solid and dash arrows) that are equivalent to the diagonal transfer. Red arrow shows an existing operation in (D). (**G-I**) Transfer operations are parallelized into three steps. Red arrows represent moves initially between adjacent clusters and blue arrows represent moves initially between diagonal clusters.

4.9.4.2 Optimized Redistribution Strategy based on Pair-wise Transfer Operations

The high level of redistribution policy is to optimize the number of moved particles to equalize cluster size (Fig. 4-12). The optimization is conducted using greedy algorithm (Policy 1). Particle transfers are planned between closest clusters first. Cluster distance is defined by the Manhattan norm as,

$$d\left(N_i, N_j\right) = \left|x_i - x_j\right| + \left|y_i - y_j\right| \tag{4.60}$$

where N_i and N_j are two clusters and (x_i, y_i) and (x_j, y_j) are their cluster positions (Fig. 4-12A). For example, adjacent clusters have distance of one, and diagonal clusters have distance of two. For an array of 3x3 clusters with periodic boundary condition, the maximum distance is two, which correspond to diagonal clusters. The Manhattan norm is equivalent to the number of pair-wise transfer operations needed to move particles between two clusters. By greedy algorithm, transfers are prioritized between closer clusters. Local cluster redistribution is more desired than global redistribution because the former requires less transfer operations than the latter. Between equal distance clusters, transfers are prioritized by number of particles to be transferred, which is given as,

$$\Delta N = \min\left(\left|N_i - \langle N\rangle\right|, \left|N_j - \langle N\rangle\right|\right) \tag{4.61}$$

where $\langle N\rangle$ is the mean cluster size. Particles are redistributed until the first of the two clusters reaches mean cluster size. This prevent unnecessary transfers. Fig. 4-12B presents a distribution based on 3×3 clusters, where mean cluster size is 400. Fig. 4-12C shows the

transfer operation between two adjacent clusters (d = 1) that has the largest number of transferred particles. Fig. 4-12D shows a summary of all transfer operations between adjacent clusters (d = 1), and Fig. 4-12E shows a summary of transfers between diagonal clusters (d = 2), which has only one move for this specific case, and is determined after all adjacent cluster redistributions are conducted. Through transfers shown in Fig. 4-12D-E, all clusters end with equal sizes.

While redistribution between adjacent clusters can be directly carried out using a single transfer operation, redistribution between further distanced clusters has to be done into multiple steps through consecutively adjacent clusters. In this situation, multiple paths can be available, and the one that requires minimum additional transfer operations is preferred. For example, Fig. 4-12F shows the situation where a transfer between diagonal clusters can be carried out in two paths. The solid arrow requires one additional transfer operation, because the operation in vertical direction coincides with a previous transfer and therefore can be merged. The two operations following the dash arrow path, on the other side, are both new compared with previous operations. When multiple equivalent paths exist, a random path is selected. Finally, all transfers can be parallelized if they involve different clusters (Fig. 4-12G-I).

The total number of misplaced particles is defined as,

$$N_{mp} = \frac{1}{2}\sum_i \left| N_i - \langle N \rangle \right| \tag{4.62}$$

which is half the differences between every cluster size and mean cluster size. This value represents the minimum number of particles need to be redistributed in order to equalize all clusters. The actual number of particles being moved is given as,

$$N_m = \sum d(i,j)\Delta N(i,j) \tag{4.63}$$

where $d(i,j)$ and $N(i,j)$ are the distance and number of particles transferred between cluster N_i and N_j. Because transfer is possible between adjacent clusters only, a total of d transfer operations is required to redistribute particles between clusters of distance d. N_m represent the actual number of particles transferred and is always larger than or equal to N_{mp}.

Table 4-3 Minimize number of transferred particles

start from closest clusters	$d\ (N_i, N_j) = 1, 2, 3, \ldots$
start from most inequal clusters	$\lvert N_x - N_y\rvert = \max(\lvert N_i - N_j\rvert)$
move minimum number of particles	$\Delta N = \min(\lvert N_x - N_{ave}\rvert, \lvert N_y - N_{ave}\rvert)$

Table 4-4 Cluster Redistribution control policy

iterate transfer steps planned by Table 4-3	
if no particle pass cluster boundary,	if $\Delta N = 0$
apply high DC voltage	$V_{DC} = 0.4$V
then if target transfer number is not achieved,	if $\Delta N < \min(\lvert N_i - \langle N\rangle\rvert, \lvert N_j - \langle N\rangle\rvert)$
apply low DC voltage	$V_{DC} = 0.1$V
then if target transfer number is achieved,	if $\Delta N = \min(\lvert N_i - \langle N\rangle\rvert, \lvert N_j - \langle N\rangle\rvert)$
turn off DC voltage	$V_{DC} = 0$V

4.10 Remove Grain Boundaries

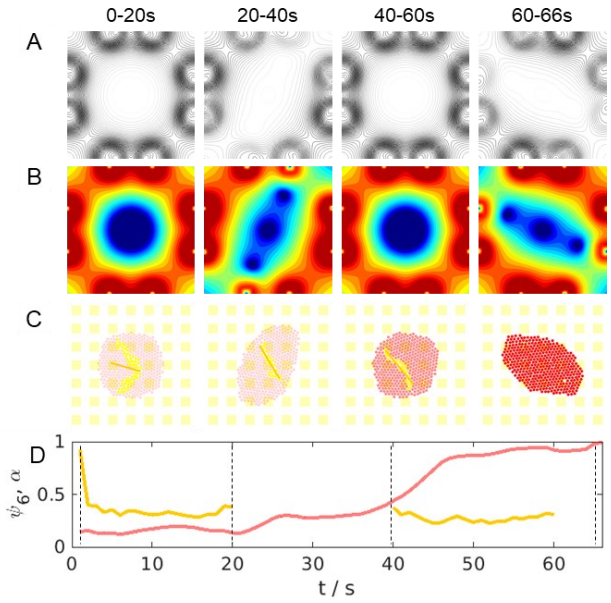

Figure 4-13 **Grain boundary remove in a unit cluster.** (**A**) MHz AC electric fields applied during each period of control. The plots scale between 0 and 0.05 V/μm. (**B**) Energy landscapes for single particle interaction with AC fields. The plots scale between 0 and 40kT. (**C**) Equilibrium particle configurations under each field shape. Grain boundary particles are colored in yellow and others are colored according to ψ_6 of each cluster in white (ψ_6 = 0) to red (ψ_6 = 1) scale. (**D**) Control parameters, including crystallinity ψ_6 (red) and grain orientation α (yellow) related to anisotropic field orientation for each cluster. Dash lines correspond to capture times of (C).

4.10.1 Electric field

MHz AC electric field is used to control removal of grain boundaries simultaneously in all clusters. Eight electrodes are activated, where four of them are ground and other four are active and grouped into diagonal pairs (Fig. 4-13A). Every adjacent cluster region shares two electrodes, and therefore resulting electric fields are in mirror position. Field shape in each cluster region is controlled by the relative voltage applied to the two pair of active electrodes. When two voltages are equal, the resulting field is isotropic. When two voltages are inequal, the field elongates towards the electrodes with

lower voltage. To minimize complexity of field, only two anisotropic field directions are designed, which are used in the control. Minimum voltage required to full crystallize a given number of particles can be determined theoretically based on thermodynamic phase behavior of colloid system.

4.10.2 Energy landscape

Magnitude and distribution of particle-field energy landscape is defined by Eq. (4.8) and shown in Fig. 4-13B. Energy landscape is proportional to square of MHz AC electric fields.

4.10.3 Equilibrium microstructure

Equilibrium configurations of particles under isotropic and anisotropic fields can be derived in theory by balancing the gradient of energy landscape with osmotic pressure due to particle condensation. Particle configurations follow closely to field and energy landscape shapes. During the control process, meanwhile, a true equilibrium microstructure is never formed, because fields are constantly changed during each control period, so that particles only asymptotically approach equilibrium positions.

4.10.4 Control policy

An open loop policy is used in this paper to direct the removal of grain boundaries in hierarchical colloidal clusters (Policy 2). The policy iterates with constant period time. In each period, an isotropic and one of the two anisotropic fields are alternatively applied. The first period is always anisotropic, where the field orientation is randomly chosen. In the subsequent anisotropic periods, the perpendicular field direction from the previous

anisotropic period is used. The endpoint is defined as when ψ_6>0.99 for all clusters. The control immediately terminates when the endpoint condition is met.

Table 4-5. Remove grain boundaries in all clusters

iterate with period time Δt = 40s	
endpoint detection every second	end if ψ_6>0.99 for all clusters
for first half of period, apply anisotropic field	$V_1 \neq V_2$ when $t < 0.5\Delta t$
random orientation	$V_1 > V_2$ if $U(0,1) > 0.5$, else $V_1 < V_2$
for second half of period, apply isotropic field	$V_1 = V_2$ when $t > 0.5\Delta t$

4.11 Morphology Control

4.11.1 Electric field

MHz AC electric fields same as in grain boundary remove control are used here.

4.11.2 Energy landscape

Energy landscape is defined by single particle interaction with MHz AC electric field given in Eq. (4.8).

4.11.3 Equilibrium microstructure

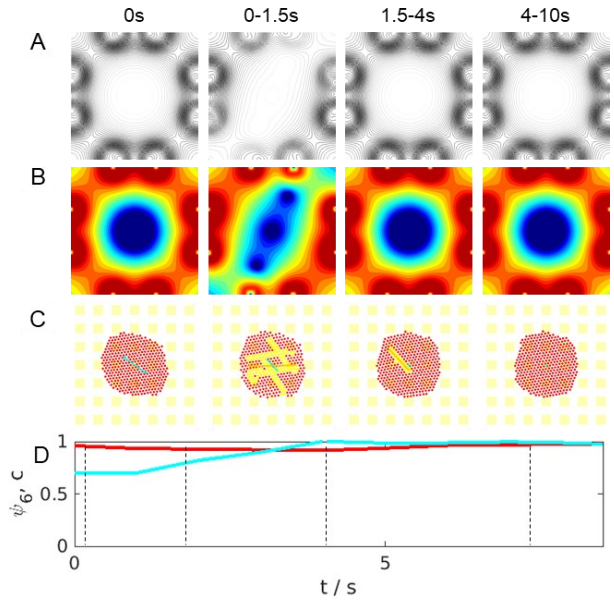

Figure 4-14 **Morphology control in a unit cluster.** (**A**) MHz AC electric fields applied during each period of control. The plots scale between 0 and 0.05 V/μm. (**B**) Energy landscapes for single particle interaction with AC fields. The plots scale between 0 and 40kT. (**C**) Equilibrium particle configurations under each field shape. Grain boundary particles are colored in yellow and others are colored according to ψ_6 of each cluster in white ($\psi_6 = 0$) to red ($\psi_6 = 1$) scale. Cyan arrows point in the direction of morphology long-axis, and the length of arrows is $(1\text{-}c)\cdot R$, where c is the morphology circularity and $R = (N\cdot a^2/\eta_{cp})^{1/2}$ is the characteristic size of cluster. (**D**) Control parameters, including crystallinity ψ_6 (red) and morphology circularity c (cyan). Dash lines correspond to capture times of (C).

Equilibrium behaviors of particles and clusters are identical to cases in grain boundary removal control. In addition, because clusters are in perfectly ordered structure at the beginning of morphology control, lattice rigidity further hinders formation of truly equilibrium structures as predicted by thermodynamics.

4.11.4 Control policy

Morphology control restores the shape of all clusters to circular with a single period of control. First, the anisotropic field perpendicular to the morphology orientation is applied until circularity is unity (c >0.99). Circular morphology can be simultaneously achieved for all clusters because both anisotropic fields and cluster morphology are in

mirror symmetry for adjacent clusters. Morphology change in the same direction for all clusters. Next, an isotropic field is applied to hold clusters until perfect crystallinity is achieved (ψ_6>0.99). With grain boundary remove control, interior grain boundary defects are all removed. Remaining defects at the beginning of isotropic period is due to local misorientation from morphology restoration. Such type of defects can be removed by thermo motion of particles and local re-organization, and therefore a simple hold using isotropic field is sufficient to achieve perfect crystals. In the rare case, where interior grain defects are re-introduced during morphology control, grain boundary remove control can be reapplied, after which morphology control can be tried again. In practice, however, such case has never been seen.

Table 4-6. Restore circular morphology for all clusters

if anisotropic morphology exists	if c<0.99 for any cluster
apply anisotropic field perpendicular to morphology circularity	$V_1 > V_2$ if $\varphi - \beta_1 < 45^o$, else $V_1 < V_2$
then if perfect crystals are not formed	if ψ_6<0.99 for any cluster
apply isotropic field	$V_1 = V_2$

4.12 Cluster Redistribution for Different Systems Sizes

Fig. 4-15A, C, E show distributions of cluster size for L/S = 1/2, 1/3, and 1/5, which correspond to arrays of 2×2, 3×3, and 5×5 clusters. colored bars represent histograms obtained from 1000 configurations in each condition, and curves represent Gaussian distributions whose mean and variance are predicted using Eq. (4.54) and (4.55). Fig. 4-15G plots the relationship between mean and standard deviation of cluster distribution and the dimension of cluster. Dash line is given by $\langle N\rangle$=3600(L/S)^2, which is the mean cluster size for all cluster dimensions. Fig. 4-15B, D, F show relationship between misplaced particle number, N_{mp}, given in Eq. (4.62), and total number of moved particles, N_m, given

in Eq. (4.63). Fig. 4-15H shows the mean and standard deviation of moved particles for different cluster dimensions.

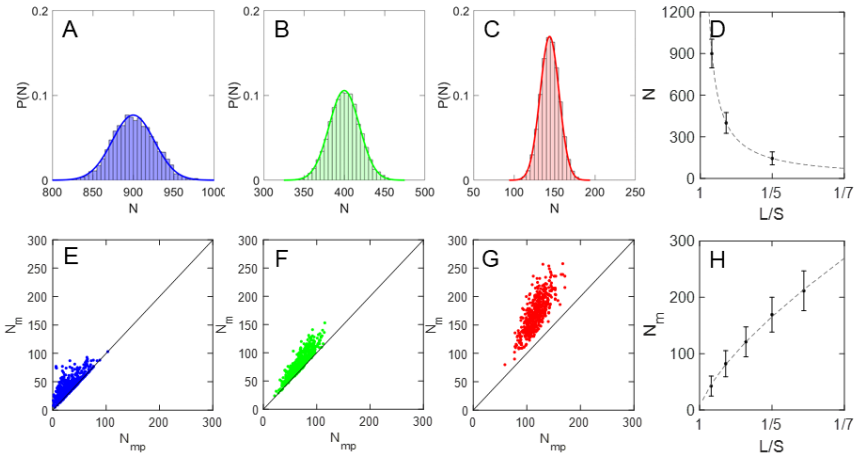

Figure 4-15 **Statistics of cluster size and redistribution operation.** (**A, C, E**) Distribution of cluster sizes by coarse partitioning for cluster dimensions of *L*/*S* = 1/2 (blue), 1/3 (green), and 1/5 (red). Bars are histograms measured over 1000 configurations. Curves are gaussian distributions predicted by density fluctuation theory in Eq. (4.54) and (4.55). The mean cluster sizes are 900, 400, and 144, and standard deviations are 26, 19, 12 for *L*/*S* = 1/2, 1/3, and 1/5. (**B, D, F**) Correlation between total number of misplaced particles (N_{mp}, Eq. (4.62)) and total number of particles moved (N_m, Eq. (4.63)) for each cluster dimension. Each scatter plot shows 200 data points. (**G**) dependency of mean and standard deviation of cluster size on cluster dimension. Error bars show standard deviations, dash line shows the analytical equation for mean cluster size as predicted by Eq. (4.55). (H). Relationship between total number of moved particles and the cluster dimensions. 1000 configurations are considered for each cluster dimension. Dash line is an empirical fitting given as $N_m=17(L/S)^{0.35}$.

Distribution of cluster sizes can be predicted by density fluctuation theory, because the sizes are determined by the configuration of particles when coarse partitioning field is applied. Mean cluster sizes can be calculated by Eq. (4.55), which gives $\langle N \rangle$ = 900, 400, and 144 for cluster dimensions of *L*/*S* = 1/2, 1/3, and 1/5. The standard deviation can be calculated by Eq. (4.54), which gives σ_N^2 = 26, 19, and 12 for each case. As cluster dimension increases, the standard deviation of cluster size decreases. Meanwhile, when considering total number of particles misplaced or being moved to equalize cluster sizes (Fig. 4-15B, D, F), both numbers increases with cluster dimension. Although for each cluster, the deviation of cluster size is smaller for smaller cluster dimension, more clusters

exist in the whole system. Overall, more particles need to be redistributed for smaller cluster dimensions. In addition, with smaller cluster dimensions, transfer of particles between clusters can take more operations, and therefore the total number of moved particles, which weights number of transferred particles with distance of transfer, also increases. If all particles moves are conducted directly between adjacent clusters, in which case a single operation is needed, the total number of misplaced particles is equal to the number of moved particles. Deviation between these two parameters correspond to the extra operations required for long-distance transfers. For smaller cluster dimensions, the scattered data are more deviated from the diagonal line.

4.13 Assembly of Perfect Crystals of Different Sizes

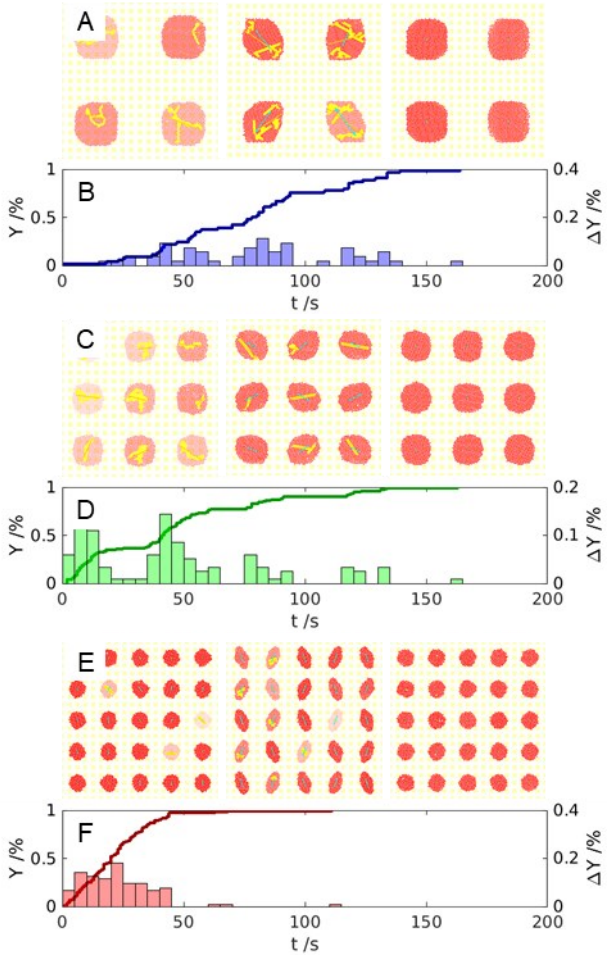

Figure 4-16 **Yield of perfect crystals for different cluster sizes.** (**A**) System with cluster dimension of L/S = 1/2, which correspond to $\langle N \rangle$ = 900 particles. Renderings show circular morphology with defects (left), anisotropic morphology with defects (middle), and circular perfect crystals (right). Grain particles are colored in yellow and other particles are colored by local ψ_6 in white (ψ_6 = 0) to red (ψ_6 = 1) scale. Cyan arrows point in the direction of morphology long-axis, and the length of arrows is $(1\text{-}c)\cdot R$, where c is the morphology circularity and $R = (N\cdot a^2/\eta_{cp})^{1/2}$ is the characteristic size of cluster. (**B**) Yield of hierarchical crystals with cluster dimension of L/S = 1/2. Histogram represent instantaneous yields (Δt = 5s) and the curve represents cumulative yield. Times for different percentages of yields are: 49s (25%), 79s (50%), 100s (75%), and 134s (100%). (**C**) System with cluster dimension of L/S = 1/3, which correspond to $\langle N \rangle$ = 400 particles. Renderings show circular morphology with defects (left), anisotropic morphology with defects (middle), and circular perfect crystals (right). (**D**) Yield of hierarchical crystals with cluster dimension of L/S = 1/3 with same legend definition as in (B). Times for different percentages of yields are: 20s (25%), 45s (50%), 72s (75%), and 129s (100%). (**E**) System with cluster dimension of L/S = 1/5, which correspond to $\langle N \rangle$ = 144 particles. Renderings show circular morphology with defects (left), anisotropic morphology with defects (middle), and circular perfect crystals (right). (**F**) Yield of hierarchical crystals with cluster dimension of L/S = 1/5 with same legend definition as in (B). Times for different percentages of yields are: 12s (25%), 22s (50%), 30s (75%), and 48s (100%).

Fig. 4-16 shows yields of perfect crystals with circular morphology as a function of time for systems dimensions of $L/S = 1/2$, 1/3, and 1/5, where each cluster has $\langle N \rangle = 900$, 400, and 144 particles. Result of each system size is averaged over 1000 cycles of simulation. For each simulation, all clusters have equal sizes and are controlled simultaneously following open loop policies for grain boundary remove and morphology control as described in previous sections. The initial states are generated by randomly quenched particles into isotropic morphologies. The time is defined as when all clusters form perfect crystals ($\psi_6 > 0.99$) with circular morphology ($c > 0.99$).

Overall a shorter assembly time is observed for finer clusters. A significant portion of clusters in $L/S = 1/5$ are already in perfect crystal state through random quenching, and therefore the early successes are more frequent than other cluster dimensions. In addition, defects are closer to periphery for small clusters, and so a rapid diffusion is observed, which causes the quick termination of all simulations. Larger clusters, on the other hand, may contain multiple defects deep inside of cluster. As a result, longer times are needed to achieve perfect structure.

5 CONLCUSIONS AND FUTURE WORK

5.1 Summary and Conclusion

This dissertation contained three focuses. First, the fundamental thermodynamics of colloids under different phases are generated and studied. Second, assembly of colloids into perfect circular crystals are controlled using morphing external fields. Last, a hierarchical assembly strategy is proposed to form ordered crystals on top of electrode array. The following conclusions are based on each of these focuses as presented in this dissertation.

5.1.1 Equilibrium Distribution of Colloids under 2D Energy Landscapes

A method was developed to determine concentration profiles and local phase behavior on energy landscapes that vary in more than one spatial coordinate. A general expression was derived based on local osmotic pressure differences balancing forces on colloids due to energy landscape gradients (when concentration and energy gradients are large compared to the particle size). This analysis is used to study colloidal particles in high frequency AC electric fields, where an octupolar electrode is used to tune the amplitude and shape of electric fields and resulting energy landscapes. By modeling the colloidal particles with an effective hard disk equation of state based on perturbation theory, it is shown that concentration profiles of locally non-uniform solid and fluid phases can be predicted for a variety of different 2D energy landscape shapes including multiple energy minima. Results are compared to Brownian Dynamic simulations to confirm the predictions of the theoretical model against time averaged equilibrium particle

configurations. Findings include practical details of determining concentration profiles and cross sections based on different known and unknown variables. Findings from this work demonstrate a general approach for obtaining concentration profiles and local phase behavior on multi-dimensional energy landscapes for colloids interacting with a variety of external fields. The reported approach is amenable to controlling colloidal microstructure on morphing energy landscapes and to the inverse design of external fields and energy landscapes based on desired colloidal concentration profiles (*e.g.*, hierarchically patterned crystals).

5.1.2 Assembly of Colloidal Crystals under Morphing External Fields

We developed a new feedback controlled approach using morphing energy landscapes to remove GBs and produce circular shapes in colloidal crystals. We demonstrated this approach in microscopy and simulation experiments for colloidal particles in AC electric fields, although the reported approach is generalizable to any morphing energy landscape. We discovered how easily accessible energy landscape shapes and orientations together could enhance coupled GB and crystal morphology relaxation processes. Based on this finding, RL was used to develop an optimized control policy to close the loop between sensing states and actuating morphing energy landscapes to rapidly and reliably produce defect-free circular crystals.

The resulting optimized control enabled by morphing energy landscapes is superior to benchmarks and is scalable to different system sizes. Statistical comparisons of controlled stochastic trajectories quantify the speed and accuracy of producing defect-free circular crystals, where: (1) feedback controlled morphing energy landscapes produces perfect crystals an order of magnitude faster than feedback controlled isotropic landscapes,

and (2) both feedback controlled methods are dramatically faster than the nearly unbounded times required for uncontrolled relaxation of defective crystals into perfect structures. The key element provided by morphing energy landscapes that enables rapid creation of perfect crystals is the ability to exert anisotropic stresses to control crystal defects/shapes without melting, which is inherently faster than repeated melting/freezing (disassembly/assembly) processes. Finally, this new control approach is scalable to different system sizes, with average times for creating defect-free circular crystals increasing as $N^{0.5}$. In short, morphing energy landscapes in conjunction with optimized feedback control can assemble defect-free colloidal crystals with non-trivial improvements to speed and scaling compared to state-of-the-art methods.

Future work could extend the scalability of our approach, most likely without the need for higher fidelity control. Addressing multiple crystals on electrode arrays, or any periodic landscape, via parallel and serial combinations of our control approach, could be used to merge adjacent crystals into larger crystals or to create hierarchical patterned crystal structures. Given the success of elliptically shaped landscapes in this work, it is not obvious that more complex shaped landscapes would improve speed or reliability. For example, even in the limit of individually controlling every particle on highly complex landscapes, limitations due to cooperative re-arrangement processes would not obviously allow for faster net processes than coarse control of directional stresses within crystals via local field anisotropy. One further extension of this work is to control assembly of anisotropic colloidal particles, which have additional complexities due to additional orientational degrees of freedom important to equilibrium and non-equilibrium structures as well as defects. Ultimately, controlling locally repeating shapes on periodic landscapes could

produce many defect-free local structures that collectively lead to a global defect-free hierarchical structure.

5.1.3 Assembly of Hierarchical Crystals on Electrode Array

We reported a computational study of self-assembly of hierarchical colloid crystals from liquid phase using an electrode array. The process was divided into steps of coarse partitioning, cluster redistribution, and grain boundary and morphology control. Various types of DC and MHz AC electric fields were generated to facilitate different controls to colloid morphology and dynamics. We also investigated the scalability of problem for cluster redistribution and grain boundary and morphology control in terms of cluster dimension, L/S. Specifically, we presented an optimal redistribution strategy based on greedy planning algorithm and a Manhattan distance between clusters. We also presented an open loop strategy to direct the assembly of perfect, circular crystals.

The proposed strategy achieves accurate control to cluster size, crystallinity, and shape. The work is based on a simple design of electrode array, where each electrode can be individual activated with AC (alternating) and DC (offset) voltages. With the electrode array, we demonstrate control of colloidal phase behavior, nonequilibrium transport, and morphology and grain boundary defects. Based on this work, we further proposed a number of potential applications with electrode array. More cluster geometries can be formed using the electrode array, which can be used to study spherical as well as anisotropic particles. Moreover, electrode array can be used to control colloidal assembly on periodic droplet interfaces, or assembly of 3D microstructures. Finally, more complex structures, for example gears, can be obtained using an electrode array, which can be used to design micromotors.

5.2 Future Work

This dissertation demonstrates broad applications of controlling colloidal morphology and phase behavior with electric fields. This could enable future works in two ways. First, the general strategy to control colloids under external fields can be extended to more sophisticated systems, in which both fundamental behaviors and practical applications of colloids can be studied. Second, the diversity of electrode design and types of interactions between particles and electric field can be further developed in searching for more complex colloidal controls.

5.2.1 Colloidal Interactions in Nonaqueous Medium

The interactions between particles and with external electric fields are less well understood compared with aqueous systems. The low dielectric constant of nonaqueous medium can often reduce or fundamentally change the particle behaviors. The applications of colloids in nonaqueous systems, on the other hand, are ubiquitous and often possess practical and commercial interests. Controlling individual particles as well as cluster of particles are therefore both challenging and intriguing. The electrode design and electric fields discussed in this dissertation are naturally applicable to nonaqueous system without further modification.

5.2.2 Assembly on Periodic Interfaces

Strong interaction between colloids and oil-water interfaces has been known for many years.[152] Many interactions exist between particles on the interface, which affects their equilibrium configurations, dynamic properties, and various applications.[153] Some

interactions that are well understood in bulk phase is less clear between particles at interfaces.[154] Unpredicted structures are often observed that are against commonly accepted theories of colloidal interactions.[154] Moreover, assembly on curved interface adds another layer of complexity than regular 2D assembly, because periodic structures often contains geometry-based defects as well as other types of defects. The characterization of crystal lattice on a curve interface, therefore, is substantially different from a flat surface and requires both physical and mathematical models to understand. Electrode array can be used to direct assembly at interfaces, which is identical to other types of electric field mediate assembly problem but with better reconfigurability with geometry of interfaces. Moreover, electrode array can be used to achieve hierarchical assembly on periodic curved interfaces, which might be more interesting in designing novel nanostructures.

5.2.3 Assembly of Anisotropic Particles

Anisotropic particles are known as building blocks of many biomimicry functional materials and possess unique mechanical, optical, and electrical properties.[155] Anisotropic nanomaterials give rise to similarly anisotropic properties.[156] The assembly of anisotropic species into ordered, isotropic or anisotropic structures are inherently more complex than isotropic particles. Orientational order of particles with nearby particles are critical in achieving desired microstructures.[157] In addition, understanding geometry-dependent colloidal interactions is still an ongoing research. External field mediate assembly of anisotropic particles can often achieve high level of alignment and order.[155] In particularly, electric field has been used to direct assembly of many anisotropic particles. Many particles can be polarized under electric field and form chains and other ordered structures.[158] Moreover, the equilibrium orientation and position of anisotropic particles can also be

controlled with tunable electric fields. Electrode array has been shown to be versatile and capable of forming a wide variety of field shapes and conditions. It is most suitable to study equilibrium behaviors of anisotropic particles under different conditions. In addition, the control approaches developed in this dissertation can provide clues to anisotropic particle controls. The anisotropic electric fields, for example, can be a natural fit to the control of similarly anisotropic particles.

5.2.4 Control of complex Colloidal Structures and Micromotors

Active particles or micromotors are studied with potential applications in biomedicine, mechanical engineering, and environmental engineering.[154, 159] One perspective is to design self-propelled particles, also known as microswimmers, which could navigate in confined environment and actively searching for specific targets and sites.[160] Another possible strategy is to direct the particle translocation via extern field.[161] This can be potentially interesting in achieving functionalities of micromotors without chemical or structural modifications to particles. By harvesting external energy and converting to its own kinetic energy, particles can act as micro-cargo carriers to capture, transport, and release other objects. They can also be studied as the model for collaborative functions of natural material and living species. Electrode array is capable of generated complex and dynamic external fields to assemble and drive colloidal micromotors as single particle or ensemble cluster. In addition, some of the control planning algorithms, such are reinforcement learning, are inherently suitable for such robotic planning and control tasks.

REFERENCES

1. Moffitt, J. R.; Chemla, Y. R.; Smith, S. B.; Bustamante, C., Recent Advances in Optical Tweezers. *Annual Review of Biochemistry* **2008,** *77* (1), 205-228.

2. Dinsmore, A. D.; Crocker, J. C.; Yodh, A. G., Self-assembly of colloidal crystals. *Current Opinion in Colloid & Interface Science* **1998,** *3* (1), 5-11.

3. Ye, X.; Qi, L., Two-dimensionally patterned nanostructures based on monolayer colloidal crystals: Controllable fabrication, assembly, and applications. *Nano Today* **2011,** *6* (6), 608-631.

4. Grzelczak, M.; Vermant, J.; Furst, E. M.; Liz-Marzán, L. M., Directed Self-Assembly of Nanoparticles. *ACS Nano* **2010,** *4* (7), 3591-3605.

5. Hermanson, K. D.; Lumsdon, S. O.; Williams, J. P.; Kaler, E. W.; Velev, O. D., Dielectrophoretic Assembly of Electrically Functional Microwires from Nanoparticle Suspensions. *Science* **2001,** *294* (5544), 1082.

6. Tracy, J. B.; Crawford, T. M., Magnetic field-directed self-assembly of magnetic nanoparticles. *MRS Bulletin* **2013,** *38* (11), 915-920.

7. Greving, I.; Cai, M.; Vollrath, F.; Schniepp, H. C., Shear-Induced Self-Assembly of Native Silk Proteins into Fibrils Studied by Atomic Force Microscopy. *Biomacromolecules* **2012,** *13* (3), 676-682.

8. Kalsin, A. M.; Fialkowski, M.; Paszewski, M.; Smoukov, S. K.; Bishop, K. J. M.; Grzybowski, B. A., Electrostatic Self-Assembly of Binary Nanoparticle Crystals with a Diamond-Like Lattice. *Science* **2006,** *312* (5772), 420.

9. Swan, J. W.; Vasquez, P. A.; Whitson, P. A.; Fincke, E. M.; Wakata, K.; Magnus, S. H.; Winne, F. D.; Barratt, M. R.; Agui, J. H.; Green, R. D.; Hall, N. R.; Bohman, D. Y.; Bunnell, C. T.; Gast, A. P.; Furst, E. M., Multi-scale kinetics of a field-directed colloidal phase transition. *Proceedings of the National Academy of Sciences* **2012,** *109* (40), 16023.

10. Beckham, R. E.; Bevan, M. A., Interfacial colloidal sedimentation equilibrium. I. Intensity based confocal microscopy. *The Journal of Chemical Physics* **2007,** *127* (16), 164708.

11. Russel, W. B.; Saville, D. A.; Schowalter, W. R., *Colloidal Dispersions*. Cambridge University Press: New York, 1989.

12. Anderson, J. L., Colloid transport by interfacial forces. *Ann. Rev. Fluid Mech.* **1989,** *21*, 61-99.

13. Morgan, H.; Green, N. G., *AC electrokinetics: colloids and nanoparticles*. Research Studies Press: Philadelphia, PA, 2003.

14. Lim, J.; Lanni, C.; Evarts, E. R.; Lanni, F.; Tilton, R. D.; Majetich, S. A., Magnetophoresis of Nanoparticles. *ACS Nano* **2011,** *5* (1), 217-226.

15. Biben, T.; Hansen, J.-P.; Barrat, J.-L., Density profiles of concentrated colloidal suspensions in sedimentation equilibrium. *J. Chem. Phys.* **1993,** *98* (9), 7330-7344.

16. Lu, M.; Bevan, M. A.; Ford, D. M., Interfacial Colloidal Sedimentation Equilibrium II. Closure based Density Functional Theory. *J. Chem. Phys.* **2007,** *127*, 164709.

17. Perrin, J. B., Realite moleculaire (Molecular Reality). *J. Ann. Chim. Phys.* **1909,** *18*, 1.

18. Perrin, J., *Atoms*. D. van Nostrand Company: New York, 1916.

19. Carnahan, N. F.; Starling, K. E., Equation of state for nonattracting rigid spheres. *J. Chem. Phys.* **1969,** *51*, 635.

20. Hall, K. R., Another Hard-Sphere Equation of State. *J. Chem. Phys.* **1972,** *57* (6), 2252-2254.

21. Hachisu, S.; Takano, K., Pressure of Disorder to Order Transition in Monodisperse Latex. *Advances in Colloid and Interface Science* **1982,** *16*, 233-252.

22. Davis, K. E.; Russel, W. B.; Glantschnig, W. J., Disorder-to-Order Transition in Settling Suspensions of Colloidal Silica: X-ray Measurements. *Science* **1989,** *245*, 507-510.

23. Rutgers, M. A.; Dunsmuir, J. H.; Xue, J.-Z.; Russel, W. B.; Chaikin, P. M., Measurement of the hard-sphere equation of state using screened charged polystyrene colloids. *Phys. Rev. B* **1996,** *53* (9), 5043-5046.

24. Barker, J. A.; Henderson, D., Perturbation Theory and Equation of State for Fluids. II. A Successful Theory of Liquids. *J. Chem. Phys.* **1967,** *47* (11), 4714-4721.

25. Beckham, R. E.; Bevan, M. A., Interfacial Colloidal Sedimentation Equilibrium I. Intensity Based Confocal Microscopy. *J. Chem. Phys.* **2007,** *127*, 164708.

26. Luigjes, B.; Thies-Weesie, D. M. E.; Erné, B. H.; Philipse, A. P., Sedimentation equilibria of ferrofluids: II. Experimental osmotic equations of state of magnetite colloids. *Journal of Physics: Condensed Matter* **2012,** *24* (24), 245104.

27. Beltran-Villegas, D. J.; Schultz, B. A.; Nguyen, N. H. P.; Glotzer, S. C.; Larson, R. G., Phase behavior of Janus colloids determined by sedimentation equilibrium. *Soft Matter* **2014,** *10* (26), 4593-4602.

28. Ginot, F.; Theurkauff, I.; Levis, D.; Ybert, C.; Bocquet, L.; Berthier, L.; Cottin-Bizonne, C., Nonequilibrium Equation of State in Suspensions of Active Colloids. *Physical Review X* **2015,** *5* (1), 011004.

29. Sherman, Z. M.; Swan, J. W., Dynamic, Directed Self-Assembly of Nanoparticles via Toggled Interactions. *ACS Nano* **2016,** *10* (5), 5260-5271.

30. Savenko, S. V.; Dijkstra, M., Sedimentation and multiphase equilibria in suspensions of colloidal hard rods. *Physical Review E* **2004,** *70* (5), 051401.

31. Jones, T. B., *Electromechanics of Particles*. Cambridge University Press: Cambridge, 1995; p 265.

32. Sullivan, M. T.; Zhao, K.; Hollingsworth, A. D.; Austin, R. H.; Russel, W. B.; Chaikin, P. M., An electric bottle for colloids. *Phys. Rev. Lett.* **2006,** *96*, 015703.

33. Leunissen, M. E.; van Blaaderen, A., Concentrating colloids with electric field gradients. II. Phase transitions and crystal buckling of long-ranged repulsive charged spheres in an electric bottle. *J. Chem. Phys.* **2008,** *128* (16), 164509-12.

34. Lumsdon, S. O.; Kaler, E. W.; Velev, O. D., Two-Dimensional Crystallization of Microspheres by a Coplanar AC Electric Field. *Langmuir* **2004,** *20* (6), 2108-2116.

35. Smith, B. D.; Mayer, T. S.; Keating, C. D., Deterministic Assembly of Functional Nanostructures Using Nonuniform Electric Fields. *Annual Review of Physical Chemistry* **2012,** *63* (1), 241-263.

36. Singh, J. P.; Lele, P. P.; Nettesheim, F.; Wagner, N. J.; Furst, E. M., One- and two-dimensional assembly of colloidal ellipsoids in ac electric fields. *Physical Review E* **2009,** *79* (5), 050401.

37. Juarez, J. J.; Bevan, M. A., Feedback Controlled Colloidal Self-Assembly. *Adv. Funct. Mater.* **2012,** *22* (18), 3833-3839.

38. Tang, X.; Rupp, B.; Yang, Y.; Edwards, T. D.; Grover, M. A.; Bevan, M. A., Optimal Feedback Controlled Assembly of Perfect Crystals. *ACS Nano* **2016,** *10* (7), 6791-6798.

39. Wang, X. B.; Huang, Y.; Burt, J. P. H.; Markx, G. H.; Pethig, R., Selective Dielectrophoretic Confinement of Bioparticles in Potential-Energy Wells. *J. Phys. D: Appl. Phys.* **1993,** *26* (8), 1278-1285.

40. Jones, T. B.; Washizu, M., Equilibria and dynamics of DEP-levitated particles: multipolar theory. *J. Electrostatics* **1994,** *33* (2), 199-212.

41. Juarez, J. J.; Bevan, M. A., Interactions and Microstructures in Electric Field Mediated Colloidal Assembly. *J. Chem. Phys.* **2009,** *131*, 134704.

42. Juárez, J. J.; Cui, J.-Q.; Liu, B. G.; Bevan, M. A., kT-Scale Colloidal Interactions in High Frequency Inhomogeneous AC Electric Fields. I. Single Particles. *Langmuir* **2011,** *27* (15), 9211-9218.

43. Juarez, J. J.; Liu, B. G.; Cui, J.-Q.; Bevan, M. A., kT-Scale Colloidal Interactions in High-Frequency Inhomogeneous AC Electric Fields. II. Concentrated Ensembles. *Langmuir* **2011,** *27* (15), 9219-9226.

44. Juarez, J. J.; Feicht, S. E.; Bevan, M. A., Electric Field Mediated Assembly of Three Dimensional Equilibrium Colloidal Crystals. *Soft Matter* **2012,** *8* (1), 94-103.

45. Edwards, T. D.; Beltran-Villegas, D. J.; Bevan, M. A., Size Dependent Thermodynamics and Kinetics in Electric Field Mediated Colloidal Crystal Assembly. *Soft Matter* **2013,** *9* (38), 9208-9218.

46. Henderson, D., Monte carlo and perturbation theory studies of the equation of state of the two-dimensional Lennard-Jones fluid. *Molecular Physics* **1977,** *34* (2), 301-315.

47. Alder, B. J.; Hoover, W. G.; Young, D. A., Studies in Molecular Dynamics. V. High-Density Equation of State and Entropy for Hard Disks and Spheres. *The Journal of Chemical Physics* **1968,** *49* (8), 3688-3696.

48. Bahukudumbi, P.; Bevan, M. A., Imaging Energy Landscapes using Concentrated Diffusing Colloidal Probes. *J. Chem. Phys.* **2007,** *126*, 244702.

49. Fernandes, G. E.; Beltran-Villegas, D. J.; Bevan, M. A., Spatially Controlled Reversible Colloidal Self-Assembly. *J. Chem. Phys.* **2009,** *131*, 134705.

50. Juarez, J. J.; Mathai, P. P.; Liddle, J. A.; Bevan, M. A., Multiple Electrokinetic Actuators for Feedback Control of Colloidal Crystal Size. *Lab Chip* **2012,** *12* (20), 4063-4070.

51. Tang, X.; Zhang, J.; Bevan, M. A.; Grover, M. A., A comparison of open-loop and closed-loop strategies in colloidal self-assembly. *Journal of Process Control* **2017,** *60*, 141-151.

52. Wu, H.-J.; Pangburn, T. O.; Beckham, R. E.; Bevan, M. A., Measurement and Interpretation of Particle−Particle and Particle−Wall Interactions in Levitated Colloidal Ensembles. *Langmuir* **2005,** *21* (22), 9879-9888.

53. Truskett, T. M.; Torquato, S.; Sastry, S.; Debenedetti, P. G.; Stillinger, F. H., Structural precursor to freezing in the hard-disk and hard-sphere systems *Phys. Rev. E* **1998,** *58* (3), 3083 - 3088.

54. Engel, M.; Anderson, J. A.; Glotzer, S. C.; Isobe, M.; Bernard, E. P.; Krauth, W., Hard-disk equation of state: First-order liquid-hexatic transition in two dimensions with three simulation methods. *Physical Review E* **2013,** *87* (4), 042134.

55. Regnaut, C.; Ravey, J. C., Application of the Adhesive Sphere Model to the Structure of Colloidal Suspensions. *J. Chem. Phys.* **1989,** *91* (2), 1211-1221.

56. Nelson, D. R.; Halperin, B. I., Dislocation-Mediated Melting in Two Dimensions. *Phys. Rev. B* **1979**, 2457-2484.

57. van Teeffelen, S.; Likos, C. N.; Löwen, H., Colloidal Crystal Growth at Externally Imposed Nucleation Clusters. *Physical Review Letters* **2008,** *100* (10), 108302.

58. Berrut, J.-P.; Trefethen, L. N., Barycentric Lagrange Interpolation. *SIAM Review* **2004,** *46* (3), 501-517.

59. Edwards, T. D.; Yang, Y.; Beltran-Villegas, D. J.; Bevan, M. A., Colloidal Crystal Grain Boundary Formation and Motion. *Sci. Rep.* **2014,** *4*, 06132.

60. Yang, Y.; Thyagarajan, R.; Ford, D. M.; Bevan, M. A., Dynamic colloidal assembly pathways via low dimensional models. *The Journal of Chemical Physics* **2016,** *144* (20), 204904.

61. Khusid, B.; Acrivos, A., Effects of interparticle electric interactions on dielectrophoresis in colloidal suspensions. *Phys. Rev. E* **1996,** *54* (5), 5428.

62. Velev, O. D.; Gupta, S., Materials Fabricated by Micro- and Nanoparticle Assembly – The Challenging Path from Science to Engineering. *Adv. Mat.* **2009,** *21* (19), 1897-1905.

63. Zhao, Y.; Xie, Z.; Gu, H.; Zhu, C.; Gu, Z., Bio-inspired variable structural color materials. *Chemical Society Reviews* **2012,** *41* (8), 3297-3317.

64. McDougal, A.; Miller, B.; Singh, M.; Kolle, M., Biological growth and synthetic fabrication of structurally colored materials. *Journal of Optics* **2019,** *21* (7), 073001.

65. Pusey, P. N.; van Megen, W., Phase Behaviour of Concentrated Suspensions of Nearly Hard Colloidal Spheres. *Nature* **1986,** *320* (6060), 340-342.

66. Hachisu, S.; Kobayashi, Y. J., Kirkwood-Alder Transition in Monodisperse Latexes II. Aqueous Latexes Of High Electrolyte Concentration. *J. Colloid. Interface Sci.* **1974,** *46*, 470-476.

67. Swan, J. W.; Bauer, J. L.; Liu, Y.; Furst, E. M., Directed colloidal self-assembly in toggled magnetic fields. *Soft Matter* **2014,** *10* (8), 1102-1109.

68. Helseth, L. E.; Wen, H. Z.; Hansen, R. W.; Johansen, T. H.; Heinig, P.; Fischer, T. M., Assembling and Manipulating Two-Dimensional Colloidal Crystals with Movable Nanomagnets. *Langmuir* **2004,** *20* (17), 7323-7332.

69. Bharti, B.; Velev, O. D., Assembly of Reconfigurable Colloidal Structures by Multidirectional Field-Induced Interactions. *Langmuir* **2015,** *31* (29), 7897-7908.

70. Hilou, E.; Du, D.; Kuei, S.; Biswal, S. L., Interfacial energetics of two-dimensional colloidal clusters generated with a tunable anharmonic interaction potential. *Physical Review Materials* **2018,** *2* (2), 025602.

71. Ackerson, B. J., *Shear induced order and shear processing of model hard sphere suspensions*. SOR: 1990; Vol. 34, p 553-590.

72. Solomon, T.; Solomon, M. J., Stacking fault structure in shear-induced colloidal crystallization. *Journal of Chemical Physics* **2006,** *124* (13), 10.

73. Loudiyi, K.; Ackerson, B. J., Direct observation of laser induced freezing. *Physica A* **1992,** *184*, 1-25.

74. Ashkin, A.; Dziedzic, J. M.; Bjorkholm, J. E.; Chu, S., Observation of a single-beam gradient force optical trap for dielectric particles. *Opt. Lett.* **1986,** *11* (5), 288-290.

75. Korda, P. T.; Grier, D. G., Annealing thin colloidal crystals with optical gradient forces. *J. Chem. Phys.* **2001,** *114* (17), 7570-7573.

76. Vossen, D. L. J.; Plaisier, M. A.; Blaaderen, A. v., *Colloidal crystallization induced by optical gradient forces exerted by optical tweezers*. SPIE: 2004; Vol. 5514, p 755-762.

77. Huang, Y.; Pethig, R., Electrode Design for Negative Dielectrophoresis. *Meas. Sci. Technol.* **1991,** *2*, 1142-1146.

78. Chaudhary, S.; Shapiro, B., Arbitrary steering of multiple particles at once in an electroosmotically driven microfluidic system. *IEEE Transactions on Control Systems Technology* **2006,** *14* (4), 669-680.

79. Lu, J. P.; Thompson, J. D.; Whiting, G. L.; Biegelsen, D. K.; Raychaudhuri, S.; Lujan, R.; Veres, J.; Lavery, L. L.; Völkel, A. R.; Chow, E. M., Open and Closed Loop Manipulation of Charged Microchiplets in an Electric Field. *Appl. Phys. Lett.* **2014,** *105* (5), 054104.

80. Hayward, R. C.; Saville, D. A.; Aksay, I. A., Electrophoretic assembly of colloidal crystals with optically tunable micropatterns. *Nature* **2000,** *404* (6773), 56-59.

81. Kim, Y.; Shah, A. A.; Solomon, M. J., Spatially and Temporally Reconfigurable Assembly of Colloidal Crystals. *Nat. Commun.* **2014,** *5*, 4676.

82. Hunter, R. J., *Zeta Potential in Colloid Science: Principles and Applications*. Academic Press: New York, 1981.

83. Morrison, I. D., Electrical charges in non-aqueous media. *Coll. Surf. A* **1993,** *71*, 1-37.

84. Zhang, J.; Zhang, Y.; Bevan, M. A., Spatially Varying Colloidal Phase Behavior on Multi-Dimensional Energy Landscapes. *J. Chem. Phys.* **2020,** *152*, 054905.

85. Pethig, R., Review Article---Dielectrophoresis: Status of the theory, technology, and applications. *Biomicrofluidics* **2010,** *4* (2), 022811.

86. Dobnikar, J.; Snezhko, A.; Yethiraj, A., Emergent colloidal dynamics in electromagnetic fields. *Soft Matter* **2013,** *9* (14), 3693-3704.

87. Beltran-Villegas, D. J.; Sehgal, R. M.; Maroudas, D.; Ford, D. M.; Bevan, M. A., Colloidal Cluster Crystallization Dynamics. *J. Chem. Phys.* **2012,** *137* (13), 134901.

88. Coughlan, A. C. H.; Torres-Díaz, I.; Zhang, J.; Bevan, M. A., Non-equilibrium steady-state colloidal assembly dynamics. *The Journal of Chemical Physics* **2019,** *150* (20), 204902.

89. Klotsa, D.; Jack, R. L., Controlling Crystal Self-Assembly Using a Real-Time Feedback Scheme. *J. Chem. Phys.* **2013,** *138* (9), 094502.

90. Vezirov, T. A.; Gerloff, S.; Klapp, S. H. L., Manipulating Shear-Induced Non-Equilibrium Transitions in Colloidal Films by Feedback Control. *Soft Matter* **2015,** *11* (2), 406-413.

91. Yang, Y.; Thyagarajan, R.; Ford, D. M.; Bevan, M. A., Dynamic colloidal assembly pathways via low dimensional models. *J. Chem. Phys.* **2016,** *144* (20), 204904.

92. Littman, M. L., Reinforcement learning improves behaviour from evaluative feedback. *Nature* **2015,** *521*, 445.

93. Lee, J. M.; Lee, J. H., Approximate dynamic programming-based approaches for input–output data-driven control of nonlinear processes. *Automatica* **2005,** *41* (7), 1281-1288.

94. Leunissen, M. E.; Sullivan, M. T.; Chaikin, P. M.; van Blaaderen, A., Concentrating colloids with electric field gradients. I. Particle transport and

growth mechanism of hard-sphere-like crystals in an electric bottle. *J. Chem. Phys.* **2008,** *128* (16), 164508-11.

95. Wei, Q.; Lewis, F. L.; Sun, Q.; Yan, P.; Song, R., Discrete-Time Deterministic Q-Learning: A Novel Convergence Analysis. *IEEE Transactions on Cybernetics* **2017,** *47* (5), 1224-1237.

96. Davidchack, R. L.; Laird, B. B., Simulation of the hard-sphere crystal–melt interface. *The Journal of Chemical Physics* **1998,** *108* (22), 9452-9462.

97. Nelson, D. R.; Halperin, B. I., Dislocation-mediated melting in two dimensions. *Physical Review B* **1979,** *19* (5), 2457-2484.

98. Rein ten Wolde, P.; Ruiz ‐ Montero, M. J.; Frenkel, D., Numerical calculation of the rate of crystal nucleation in a Lennard ‐ Jones system at moderate undercooling. *The Journal of Chemical Physics* **1996,** *104* (24), 9932-9947.

99. Kinoshita, S.; Yoshioka, S.; Miyazaki, J., Physics of structural colors. *Reports on Progress in Physics* **2008,** *71* (7), 076401.

100. Zhang, H.; Yu, X.; Braun, P. V., Three-dimensional bicontinuous ultrafast-charge and -discharge bulk battery electrodes. *Nature Nanotechnology* **2011,** *6* (5), 277-281.

101. Ozin, G. A.; Hou, K.; Lotsch, B. V.; Cademartiri, L.; Puzzo, D. P.; Scotognella, F.; Ghadimi, A.; Thomson, J., Nanofabrication by self-assembly. *Materials Today* **2009,** *12* (5), 12-23.

102. Kim, Y.; Shah, A. A.; Solomon, M. J., Spatially and temporally reconfigurable assembly of colloidal crystals. *Nature Communications* **2014,** *5* (1), 3676.

103. Vogel, N.; Retsch, M.; Fustin, C.-A.; del Campo, A.; Jonas, U., Advances in Colloidal Assembly: The Design of Structure and Hierarchy in Two and Three Dimensions. *Chemical Reviews* **2015,** *115* (13), 6265-6311.

104. Chang, C. H.; Tian, L.; Hesse, W. R.; Gao, H.; Choi, H. J.; Kim, J. G.; Siddiqui, M.; Barbastathis, G., From Two-Dimensional Colloidal Self-Assembly to Three-Dimensional Nanolithography. *Nano Letters* **2011,** *11* (6), 2533-2537.

105. Yang, S.-M.; Jang, S. G.; Choi, D.-G.; Kim, S.; Yu, H. K., Nanomachining by Colloidal Lithography. *Small* **2006,** *2* (4), 458-475.

106. Zhang, J.; Li, Y.; Zhang, X.; Yang, B., Colloidal Self-Assembly Meets Nanofabrication: From Two-Dimensional Colloidal Crystals to Nanostructure Arrays. *Advanced Materials* **2010,** *22* (38), 4249-4269.

107. Quan, Z.; Fang, J., Superlattices with non-spherical building blocks. *Nano Today* **2010,** *5* (5), 390-411.

108. Miszta, K.; de Graaf, J.; Bertoni, G.; Dorfs, D.; Brescia, R.; Marras, S.; Ceseracciu, L.; Cingolani, R.; van Roij, R.; Dijkstra, M.; Manna, L., Hierarchical self-assembly of suspended branched colloidal nanocrystals into superlattice structures. *Nature Materials* **2011,** *10* (11), 872-876.

109. Feng, W.; Ueda, E.; Levkin, P. A., Droplet Microarrays: From Surface Patterning to High-Throughput Applications. *Advanced Materials* **2018,** *30* (20), 1706111.

110. Saranathan, V.; Osuji, C. O.; Mochrie, S. G. J.; Noh, H.; Narayanan, S.; Sandy, A.; Dufresne, E. R.; Prum, R. O., Structure, function, and self-assembly of single network gyroid (I4₁32) photonic crystals in butterfly wing scales. *Proceedings of the National Academy of Sciences* **2010,** *107* (26), 11676.

111. Xiu, Y.; Zhu, L.; Hess, D. W.; Wong, C. P., Biomimetic Creation of Hierarchical Surface Structures by Combining Colloidal Self-Assembly and Au Sputter Deposition. *Langmuir* **2006,** *22* (23), 9676-9681.

112. Lin, T.-H.; Huang, W.-H.; Jun, I.-K.; Jiang, P., Bioinspired Assembly of Colloidal Nanoplatelets by Electric Field. *Chemistry of Materials* **2009,** *21* (10), 2039-2044.

113. Liu, K.; Jiang, L., Bio-inspired design of multiscale structures for function integration. *Nano Today* **2011,** *6* (2), 155-175.

114. Goerlitzer, E. S. A.; Klupp Taylor, R. N.; Vogel, N., Bioinspired Photonic Pigments from Colloidal Self-Assembly. *Advanced Materials* **2018,** *30* (28), 1706654.

115. Li, F.; Josephson, D. P.; Stein, A., Colloidal Assembly: The Road from Particles to Colloidal Molecules and Crystals. *Angewandte Chemie International Edition* **2011,** *50* (2), 360-388.

116. Wang, J.; Zhang, Y.; Wang, S.; Song, Y.; Jiang, L., Bioinspired Colloidal Photonic Crystals with Controllable Wettability. *Accounts of Chemical Research* **2011,** *44* (6), 405-415.

117. Bai, L.; Xie, Z.; Wang, W.; Yuan, C.; Zhao, Y.; Mu, Z.; Zhong, Q.; Gu, Z., Bio-Inspired Vapor-Responsive Colloidal Photonic Crystal Patterns by Inkjet Printing. *ACS Nano* **2014,** *8* (11), 11094-11100.

118. Dumanli, A. G.; Savin, T., Recent advances in the biomimicry of structural colours. *Chemical Society Reviews* **2016,** *45* (24), 6698-6724.

119. Velev, O. D.; Kaler, E. W., Structured Porous Materials via Colloidal Crystal Templating: From Inorganic Oxides to Metals. *Advanced Materials* **2000,** *12* (7), 531-534.

120. Chiou, P. Y.; Ohta, A. T.; Wu, M. C., Massively parallel manipulation of single cells and microparticles using optical images. *Nature* **2005,** *436* (7049), 370-372.

121. Nie, Z.; Petukhova, A.; Kumacheva, E., Properties and emerging applications of self-assembled structures made from inorganic nanoparticles. *Nature Nanotechnology* **2010,** *5* (1), 15-25.

122. Munch, E.; Launey, M. E.; Alsem, D. H.; Saiz, E.; Tomsia, A. P.; Ritchie, R. O., Tough, Bio-Inspired Hybrid Materials. *Science* **2008,** *322* (5907), 1516.

123. Weekes, S. M.; Ogrin, F. Y.; Murray, W. A.; Keatley, P. S., Macroscopic Arrays of Magnetic Nanostructures from Self-Assembled Nanosphere Templates. *Langmuir* **2007,** *23* (3), 1057-1060.

124. Watanabe, S.; Mino, Y.; Ichikawa, Y.; Miyahara, M. T., Spontaneous Formation of Cluster Array of Gold Particles by Convective Self-Assembly. *Langmuir* **2012,** *28* (36), 12982-12988.

125. Yap, F. L.; Thoniyot, P.; Krishnan, S.; Krishnamoorthy, S., Nanoparticle Cluster Arrays for High-Performance SERS through Directed Self-Assembly on Flat Substrates and on Optical Fibers. *ACS Nano* **2012,** *6* (3), 2056-2070.

126. Xia, D.; Ku, Z.; Li, D.; Brueck, S. R. J., Formation of Hierarchical Nanoparticle Pattern Arrays Using Colloidal Lithography and Two-Step Self-Assembly: Microspheres atop Nanospheres. *Chemistry of Materials* **2008,** *20* (5), 1847-1854.

127. Yin, Y.; Lu, Y.; Gates, B.; Xia, Y., Template-Assisted Self-Assembly: A Practical Route to Complex Aggregates of Monodispersed Colloids with Well-Defined Sizes, Shapes, and Structures. *Journal of the American Chemical Society* **2001,** *123* (36), 8718-8729.

128. Lee, I.; Zheng, H.; Rubner, M. F.; Hammond, P. T., Controlled Cluster Size in Patterned Particle Arrays via Directed Adsorption on Confined Surfaces. *Advanced Materials* **2002,** *14* (8), 572-577.

129. Lei, Y.; Yang, S.; Wu, M.; Wilde, G., Surface patterning using templates: Concept, properties and device applications. *Chemical Society Reviews* **2011,** *40* (3), 1247-1258.

130. Xia, Y.; Yin, Y.; Lu, Y.; McLellan, J., Template-Assisted Self-Assembly of Spherical Colloids into Complex and Controllable Structures. *Advanced Functional Materials* **2003,** *13* (12), 907-918.

131. Dziomkina, N. V.; Vancso, G. J., Colloidal crystal assembly on topologically patterned templates. *Soft Matter* **2005,** *1* (4), 265-279.

132. Chen, K. M.; Jiang, X.; Kimerling, L. C.; Hammond, P. T., Selective Self-Organization of Colloids on Patterned Polyelectrolyte Templates. *Langmuir* **2000,** *16* (20), 7825-7834.

133. Manoharan, V. N.; Elsesser, M. T.; Pine, D. J., Dense Packing and Symmetry in Small Clusters of Microspheres. *Science* **2003,** *301* (5632), 483.

134. Velev, O. D.; Furusawa, K.; Nagayama, K., Assembly of Latex Particles by Using Emulsion Droplets as Templates. 1. Microstructured Hollow Spheres. *Langmuir* **1996,** *12* (10), 2374-2384.

135. Aizenberg, J.; Braun, P. V.; Wiltzius, P., Patterned Colloidal Deposition Controlled by Electrostatic and Capillary Forces. *Physical Review Letters* **2000,** *84* (13), 2997-3000.

136. Tien, J.; Terfort, A.; Whitesides, G. M., Microfabrication through Electrostatic Self-Assembly. *Langmuir* **1997,** *13* (20), 5349-5355.

137. Shillingford, C.; Grebe, V.; McMullen, A.; Brujic, J.; Weck, M., Assembly and Dynamic Analysis of Square Colloidal Crystals via Templated Capillary Assembly. *Langmuir* **2019,** *35* (37), 12205-12214.

138. Solomon, M. J., Tools and Functions of Reconfigurable Colloidal Assembly. *Langmuir* **2018,** *34* (38), 11205-11219.

139. Bevan, M. A.; Ford, D. M.; Grover, M. A.; Shapiro, B.; Maroudas, D.; Yang, Y.; Thyagarajan, R.; Tang, X.; Sehgal, R. M., Controlling assembly of colloidal particles into structured objects: Basic strategy and a case study. *Journal of Process Control* **2015,** *27*, 64-75.

140. Román, F. L.; White, J. A.; Velasco, S., Block analysis method in off-lattice fluids. *Europhysics Letters (EPL)* **1998,** *42* (4), 371-376.

141. Juárez, J. J.; Mathai, P. P.; Liddle, J. A.; Bevan, M. A., Multiple electrokinetic actuators for feedback control of colloidal crystal size. *Lab on a Chip* **2012,** *12* (20), 4063-4070.

142. Robins, M.; Fillery-Travis, A., Colloidal dispersions. Edited by W. B. Russel, D. A. Saville & W. R. Schowalter, Cambridge University Press, Cambridge, UK, 1989, xvii + 506 pp., price: £60.00. ISBN 0 521 34188 4. *Journal of Chemical Technology & Biotechnology* **1992,** *54* (2), 201-202.

143. Keh, H. J.; Anderson, J. L., Boundary effects on electrophoretic motion of colloidal spheres. *Journal of Fluid Mechanics* **1985,** *153*, 417-439.

144. Bike, S. G.; Prieve, D. C., Measurements of double-layer repulsion for slightly overlapping counterion clouds. *International Journal of Multiphase Flow* **1990,** *16* (4), 727-740.

145. Hansen, J. P.; McDonald, I. R., *Theory of Simple Liquids*. Academic Press: London, 1986.

146. Henderson, D., Simple Equation of State for Hard Disks. *Molecular Physics* **1975,** *30* (3), 971-972.

147. Baus, M.; Colot, J. L., Thermodynamics and Structure of a Fluid of Hard-Rods, Disks, Spheres, or Hyperspheres from Rescaled Virial Expansions. *Physical Review A* **1987,** *36* (8), 3912-3925.

148. Beltran-Villegas, D. J.; Sehgal, R. M.; Maroudas, D.; Ford, D. M.; Bevan, M. A., A Smoluchowski model of crystallization dynamics of small colloidal clusters. *The Journal of Chemical Physics* **2011,** *135* (15), 154506.

149. Bedeaux, D.; Mazur, P., Brownian motion and fluctuating hydrodynamics. *Physica* **1974,** *76* (2), 247-258.

150. Swan, J. W.; Brady, J. F., Simulation of hydrodynamically interacting particles near a no-slip boundary. *Physics of Fluids* **2007,** *19* (11), 113306.

151. Grassia, P. S.; Hinch, E. J.; Nitsche, L. C., Computer simulations of Brownian motion of complex systems. *Journal of Fluid Mechanics* **2006,** *282*, 373-403.

152. Liu, I. B.; Sharifi-Mood, N.; Stebe, K. J., Capillary Assembly of Colloids: Interactions on Planar and Curved Interfaces. *Annual Review of Condensed Matter Physics* **2018,** *9* (1), 283-305.

153. McGorty, R.; Fung, J.; Kaz, D.; Manoharan, V. N., Colloidal self-assembly at an interface. *Materials Today* **2010,** *13* (6), 34-42.

154. Morrison, I. D.; Ross, S., *Colloidal dispersions: suspensions, emulsions, and foams*. Wiley-Interscience New York: 2002.

155. Thorkelsson, K.; Bai, P.; Xu, T., Self-assembly and applications of anisotropic nanomaterials: A review. *Nano Today* **2015,** *10* (1), 48-66.

156. Glotzer, S. C.; Solomon, M. J., Anisotropy of building blocks and their assembly into complex structures. *Nature Materials* **2007,** *6* (8), 557-562.

157. Liu, Q.; Cui, Y.; Gardner, D.; Li, X.; He, S.; Smalyukh, I. I., Self-Alignment of Plasmonic Gold Nanorods in Reconfigurable Anisotropic Fluids for Tunable Bulk Metamaterial Applications. *Nano Letters* **2010,** *10* (4), 1347-1353.

158. Rupp, B.; Torres-Díaz, I.; Hua, X.; Bevan, M. A., Measurement of Anisotropic Particle Interactions with Nonuniform ac Electric Fields. *Langmuir* **2018,** *34* (7), 2497-2504.

159. Xiao, Z.; Wei, M.; Wang, W., A Review of Micromotors in Confinements: Pores, Channels, Grooves, Steps, Interfaces, Chains, and Swimming in the Bulk. *ACS Applied Materials & Interfaces* **2019,** *11* (7), 6667-6684.

160. Khezri, B.; Novotný, F.; Moo, J. G. S.; Nasir, M. Z. M.; Pumera, M., Confined Bubble-Propelled Microswimmers in Capillaries: Wall Effect, Fuel Deprivation, and Exhaust Product Excess. *Small* **2020,** *16* (27), 2000413.

161. Yang, G.-Z.; Bellingham, J.; Dupont, P. E.; Fischer, P.; Floridi, L.; Full, R.; Jacobstein, N.; Kumar, V.; McNutt, M.; Merrifield, R., The grand challenges of Science Robotics. *Science robotics* **2018,** *3* (14), eaar7650.

CURRICULUM VITAE

EDUCATION

Ph.D.

Aug. 2015 − Oct. 2020	Johns Hopkins University, Baltimore, MD
	Department of Chemical and Biomolecular Engineering
	Advisors: Prof. Michael A. Bevan

M.S.E.

Aug. 2014 − May. 2015	University of California, Berkeley, CA
	Department of Chemical and Biomolecular Engineering

B.S.

Aug. 2010 − Aug. 2014	Georgia Institute of Technology, Atlanta, GA
	Department of Chemical and Biomolecular Engineering

AWARDS AND HONORS

ACS Colloids, Soft Matter poster prize	2017
UC, Berkeley Product Development scholarship ($20,000/yr.)	2015
NSF fellowship for Undergraduate Summer Research Program	2013

PUBLICATIONS

Zhang, J.; Bevan, M.A., (2020). Hierarchical Assembly of Colloids on Electrode Array. manuscript in preparation.
Zhang, J.; Yang, J; Zhang, Y; Bevan, M.A., (2020). Perfect Colloidal Crystals via Morphing Energy Landscapes & Reinforcement Learning. *Sci. Adv.* submitted.
Zhang, J.; Zhang, Y; Bevan, M.A., (2020). Spatially Varying Colloidal Phase Behavior on Multi-Dimensional Energy Landscapes, *J. Chem. Phys*.
Coughlan A.C.H.; Torres, I**.**; **Zhang, J**.; Bevan, M.A., (2019). Non-Equilibrium Steady-State Colloidal Assembly Dynamics, *J. Chem. Phys.*
Lin, L.; **Zhang, J.**; Peng, X.; Wu, Z.; Coughlan A.C.H.; Mao, Z.; Bevan, M.A.; Zheng, Y., (2017). Opto-thermophoretic Assembly of Colloidal Matter. *Sci. Adv*.
Tang, X.; **Zhang, J.**; Bevan, M.A.; Grover, M.A. (2017). A Comparison of Open-Loop and Closed-Loop Strategies in Colloidal Self-Assembly. *J. Process Control*.